UNIVERSITY OF SOUTHAMPTON

FACULTY OF PHYSICAL SCIENCES AND ENGINEERING

Optoelectronics Research Centre

Optical integrated circuits for large-scale quantum networks

By

Matthew T. Posner

Thesis for the

degree of Doctor of Philosophy

December 2017

UNIVERSITY OF SOUTHAMPTON

ABSTRACT

FACULTY OF PHYSICAL SCIENCES AND ENGINEERING

Optoelectronics Research Centre

DOCTOR OF PHILOSOPHY

OPTICAL INTEGRATED CIRCUITS FOR LARGE-SCALE QUANTUM NETWORKS

by Matthew Thomas Posner

This thesis presents the development of a platform to fabricate photonics integrated circuits that can be used to scale networks intended for quantum information processing (QIP) experiments. The stringent technical requirements for the transport and manipulation of quantum states of light are discussed with respect to channel waveguides and integrated gratings fabricated in silica-on-silicon through direct UV writing laser processing.

Tilted gratings are identified as a method to enable polarisation-based applications for this integrated platform. A novel implementation of in-line planar waveguide polarisers based on 45° tilted gratings is presented, demonstrating gratings with polarisation extinction ratio (PER) of 0.25 dB / mm and bandwidth impairments better than 0.3 dB in the C-band. 45° tilted gratings in UV written waveguides are used to create novel polarising coupler architectures with PER of 28.5 dB.

The alteration of the material composition of germanosilicate planar core layers is investigated, producing waveguides with birefringence of $4.5 \pm 0.2 \times 10^{-4}$, higher than previously reported for this platform. A process for producing end facet endcaps to extend the platform's capability for high power applications is also described. These developments offer potential for the scaling of QIP experiments with heralded spontaneous four-wave mixing single-photon sources.

Finally, the thesis describes research-based education experiments conducted to inform a wide range of audiences on the importance of photonics technologies. The concept of Photonics, and the underlying science and associated research, has been introduced to 2,952 students from 81 schools in the South of England and over 6,000 people in public events.

Contents

List of figures

List of tables

Nomenclature

ASE	Amplified spontaneous emission
BT	Beam tracing
CMP	Chemical-mechanical polishing
DUW	Direct ultra-violet writing
EOM	Electro-optic modulator
FEM	Finite-element modelling
FHD	Flame hydrolysis deposition
IYL 2015	2015 International Year of Light
MFD	Mode-field diameter
MIR	Mid infrared
MM	Multimode
MZI	Mach-Zehnder interferometer
NA	Numerical aperture
NIR	Near infrared
OSA	Optical spectrum analyser
PDL	Polarisation dependent loss
PER	Polarisation extinction ratio
PER	Public engagement with research
PIC	Photonics integrated circuits
PM	Polarising maintaining
PMC	Planar mode coupling
PSO	Position synchronised output
QIP	Quantum information processing
SFWM	Spontaneous four-wave mixing
SM	Single mode
SoS	Silica-on-silicon
TE/TM	Transverse electric/magnetic
TIR	Total internal reflection
UV	Ultra-violet

Declaration of authorship

I, Matthew Thomas Posner, declare that this thesis entitled “Optical integrated circuits for large-scale quantum networks” and the work presented in it are my own and has been generated by me as the result of my own original research.

I confirm that:

1. This work was done wholly or mainly while in candidature for a research degree at this University;
2. Where any part of this thesis has previously been submitted for a degree or any other qualification at this University or any other institution, this has been clearly stated;
3. Where I have consulted the published work of others, this is always clearly attributed;
4. Where I have quoted from the work of others, the source is always given. With the exception of such quotations, this thesis is entirely my own work;
5. I have acknowledged all main sources of help;
6. Where the thesis is based on work done by myself jointly with others, I have made clear exactly what was done by others and what I have contributed myself;
7. Parts of this work have been published in the following publications, as indicated in the relevant chapters:

M. T. Posner, P. L. Mennea, N. Podoliak, P. Horal, J. C. Gates, and P. G. R. Smith, "45° tilted gratings for silica-based integrated polarizers," in *2015 European Conference on Lasers and Electro-Optics - European Quantum Electronics Conference*, (Optical Society of America, 2015), paper CE_10_5, 2015.

M. T. Posner, P. L. Mennea, N. Podoliak, P. Horak, J. C. Gates, and P. G. Smith, "Integrated polarizing coupler based on tilted gratings," in *Advanced Photonics 2016 (IPR, NOMA, Sensors, Networks, SPPCom, SOF)*, OSA technical Digest (online) (Optical Society of America, 2016), paper IW3B.3, 2016.

M. T. Posner, P. V John, D. Standen, N. V. Wheeler, L. D. van Putten, N. Soper, T. Parsonage, N. H. L. Wong, and G. Brambilla, "Reflecting photonics: Reaching new audiences through new partnerships: IYL 2015 and the Royal Horticultural Society flower show," in *Proc. SPIE 9946*, pp. 9946–2, 2016.

M. T. Posner, P. V John, N. H. L. Wong, V. Mittal, and M. M. Nunez-Velazquez, "From school classes to UNESCO: IYL-enabled environments for tackling the STEM skills shortage through student-led outreach, (*Invited Paper*)" in *Proc. SPIE 9946*, pp.9946-6, 2016.

M. T. Posner, A. Jantzen, L. D. Van Putten, A. Ravagli, A. L. Donko, N. Soper, N. H. L. Wong, and P. V. John, "Cathedral outreach: student-led workshops for school curriculum enhancement in non-traditional environments," in *Proc. SPIE 10452*, pp. 10452-07, 2017.

M. T. Posner, R. H. S Bannerman, D. H. Smith, P. L. Mennea, J. C. Gates, P. G. R. Smith, "High-birefringence direct-UV-written silica waveguides for heralded single-photon sources at telecom wavelengths," in *Conference on Lasers and Electro-Optics Europe (CLEO Europe)*, 2017.

Signed: .....

Date: .....

Acknowledgements

There are a great number of people to whom thanks are due for the help and inspiration over the course of my PhD.

I am deeply grateful to my supervisors, James Gates and Peter Smith. Their expertise has been a source of ideas. Their experience has been unmatched guidance.

I wish to thank the Engineering and Physical Sciences Research Council (EPSRC), UK, for supporting me over the four years of my PhD.

I have had the privilege of working within an amazing research group. Thank you to the members of past, present and future for the stimulating discussions over the years. Thank you: Christopher Holmes, Paula Smith, Corin Gawith, Sam Berry, Lewis Carpenter, Devin Smith, Teresa Fereiro, Peter Cooper, Paolo Mennea, Stephen Lynch, Paul Gow, Rex Bannerman, Miranda Turvey, Alexander Jantzen, James Field, Alan Gray, Bolan Liu, Senta Scholl, Helen Rogers, Chaotan Sima, Sumiaty Ambran and Dominic Wales.

I also wish to thank past and present colleagues at the University of Southampton, my Optics and Photonics Society committees for making me feel a part of a vibrant professional community, and my *Lightwavers* for fuelling me with enthusiasm. A special thanks goes to Pearl John, for giving me a voice to engage with unexpected audiences in ways I could never have dreamt of.

Thank you to my cycling buddies, Trevor Allen, Charlie Leech, James Robards, Rob Collier, Chris Brooks, Alex Clayton, George Crammond, Henry Nixon, and many *SURCers*, for the cycling, coffee and chat; and to my dearest friends, Dominic Harrison and Grégoire Hutin, for being there to chat from near or afar.

Thank you to my family, Rebecca, Mum and Dad, for everything.

And finally, thank you to Becky, for being loving, caring, putting up with me throughout this adventure and for always being there.

Education breeds confidence.

Confidence breeds hope.

Hope breeds peace.

Confucius

Chapter 1 Introduction

Photonics, the science of light, is recognised as a "key enabling technology" with far-reaching economic potential in and beyond the 21st century [1]. The benefits brought to society by the theoretical and technological advancements in the light sciences were observed globally in 2015 through the United Nations Educational, Scientific and Cultural Organisation's (UNESCO) International Year of Light and Light-based Technologies (IYL 2015). Theodore Maiman's first demonstration of the ruby laser [2] undoubtedly initiated one of the great technological achievements of the last century; indeed 20% of seminal accounts on the development of optics in the past century highlight this discovery [3]. Its significance is also being celebrated by the implementation of the UNESCO International Day of Light, to be held annually on 16th May, the day where the discovery was first reported – see Figure 1.1 (b).

Figure 1.1 – (a) The United Nations General Assembly proclaimed 2015 as the International Year of Light and light-based technologies. (b) The International Day of Light will be celebrated annually from 16th May 2018.

Integrated photonics can be described as the miniaturisation of photonics functions. Stewart Miller's seminal paper on integrated optics heralded half a century of research and development in this field [4]. Today, a plethora of different technologies have led to the integration of photonics into applications applied to high-speed telecommunications, sensing, and computing. The research in this thesis stems from the observation of the potential for functionalisation of silica-based planar technologies to complement the rich field of integrated photonics components, whilst offering compatibility and potential for integration with low-loss silica fibre components and systems.

Silica-based integrated photonics has been a key component in optical telecommunication systems for over 20 years. Research at the University of Southampton's Optoelectronics Research Centre (ORC) was initiated in this area over 15 years ago. Part of this research was the development of novel silica planar geometries through flame hydrolysis deposition, a technique adapted from mature fibre preform fabrication processes. Functionalisation of planar devices was achieved by generating glass layers photosensitive to ultraviolet (UV) radiation to create channel waveguides [5]. By using two UV beams, gratings could be inscribed, providing an essential functionalisation step for passive structures for filtering and routing of signals [6]. The fundamental techniques have been advanced to allow more complex grating engineering [7], and novel non-destructive grating-based interrogation of the waveguides properties [8]. Techniques and devices have been developed, patented [9], [10] and successfully spun-out from research to industry (www.stratophase.com). Applications have been researched in various fields including chemical sensing, telecommunications and quantum information processing. The latter field has driven significant further development of the fabrication platform to investigate novel areas of science and technology.

1.1 Engineering the building blocks for quantum photonics

Over the past 20 years, quantum engineering has evolved considerably. The "second quantum revolution" strives to develop devices harnessing quantum principles [11]. This section will outline the key areas of technological applications utilising quantum phenomena and discuss the role of photonics in advancing this field.

1.1.1 Quantum-enabled technologies

The basis of quantum technology relies on being able to manipulate fundamental units of quantum information, quantum bits or qubits. Qubits can be thought of as particles capable of exhibiting quantum behaviour. Several technologies are being employed by researchers including photons, ions and trapped atoms, as well quantum dot, superconductor and nuclear magnetic resonance systems, which have all historically been used to study quantum science. The extension of these systems to quantum technologies have found applications in communications [12], sensing [13], and computing [14]. A full review of these fields is outside the scope of this study and the reader is referred to the aforementioned reviews for further details. The system of implementation for future technologies is unknown and is likely to be a hybrid of qubit platforms. Photonics has been instrumental in the development of technologies and the following section focuses on this implementation.

1.1.2 Photonics for quantum technologies

A photonic quantum system relies on transporting and precisely manipulating two or more photons. The key requirement is to preserve the quantum properties throughout the process. This section highlights the stringent requirements to achieve this.

Photons can be used as qubits. Their transmission speed, low-noise properties and limited interaction with the environment makes them an ideal candidate to transfer quantum states [15]. Silica fibre technology has been used as a platform to transport quantum states due to its very low transmission loss in the visible and near-infrared where laser systems and advanced detectors can be employed in proof of concept quantum experiments. Although the quantum state lifetime of a photon is very long, the *decoherence* of a quantum state is limited by loss [14]. This comes in many forms including coupling loss and propagation losses (scattering, absorption).

The processing of photonics qubits was an important limitation to exploiting photonics. A breakthrough was reported in 2001 that allowed quantum information processing (QIP) based solely on single-photon sources, detectors and linear optical networks [16]. Passive network components harnessing quantum behaviour have been used to solve problems with high complexity exceeding that which a classical

computer could solve, such as Boson sampling [17]. The scaling to more complex systems will require systems combining memories, detectors, circuits and reliable sources [18]. Although loss tolerant protocols are being developed, the scaling of the system will be limited by loss. A more extensive treatise of the restrictions imposed by loss can be found elsewhere [19]. Low loss operation is the key motivation for the development of the platform used in thesis.

1.2 Photonics quantum networks

To enable technologies through quantum information science, and to open the investigation of complex quantum systems, many photons must be connected and precisely manipulated. This section discusses how integrated optics can provide the platform for the scaling of the technology.

1.2.1 Integrated quantum photonics

The previous section acknowledged that guided-wave optics, in the form of optical fibres, played a crucial role in the early stages of development of quantum photonics technologies. Integrated waveguide optics can be used to encode photonics qubits based on their path, polarisation or frequency and allow transport and manipulation of photonics qubits [20]. Tanzilli et al. remark that integrated photonics, as a guided wave technology, could advance the field towards standardised, low cost and interconnectable elements. The same authors comment that the efficient coupling from free-space or fibres to integrated photonics circuits, and vice-versa, is essential for the scaling of the platform.

There are many platforms for integrated photonics. Indium phosphide [21] and silicon based platforms [22], [23] are by far the most advanced integrated technologies, building on decades of industrial research and development. Silica-on-silicon is an ideal candidate for waveguide quantum circuits since it couples efficiently to single mode optical fibres, and is subject to only low waveguide losses [24]. In addition, silica is transparent for wavelengths in the telecommunications C-band around 1550nm, where silica-fibre has its lowest loss, and in the visible spectrum where commercial single-photon detectors are available. The fabrication of waveguides can be tailored to match the guided wave optics of silica fibres. Such a platform has been used to demonstrate QIP components using both

photolithography [25] and laser processing [26] techniques for the fabrication of buried waveguides.

1.2.2 Towards networks of large optical quantum states

The aim of this PhD research project is to further develop a platform suitable for scaling the complexity of QIP experiments. This will build on work previously conducted by the ORC's Optical Engineering and Quantum Photonics research group, led by Professor Peter G. R. Smith, to develop a silica-on-silicon platform which could be used to manufacture the sub-components required for photonic quantum networks. The research activities are undertaken in collaboration with research partners from the University of Oxford's Ultrafast Quantum Optics and Optical Metrology research group, led by Professor Ian A. Walmsley, whom possess expertise in experimental quantum optics.

The platform has previously been used to demonstrate high impact advancement in QIP experiments through the implementation of sources, circuits and detectors. Key integrated quantum experiments have been demonstrated on chip, including phase controlled quantum circuits [27], Boson sampling circuits [28] and quantum teleportation [29]. These have benefitted from low loss coupling to fibre networks, compatibility with microfabrication processes and the ability to integrate optical functions on chips (beam splitters, filters). The uniformity of the waveguides fabricated has enabled the study of interaction between heralded single-photons based on arrays of identical on-chip sources [30]. The functionalisation through gratings for in-situ waveguide characterisation and Bragg filters has permitted the optimisation of on-chip single-photon detectors [31]. The "classical" characterisation of the optical properties of devices is essential to predict their behaviour when operating in a quantum regime. The silica-on-silicon technology permits low loss integration with fibre optics platforms, which is critical for future scalability. A summary of the current applications, devices fabricated and platform characteristics is presented in Figure 1.2.

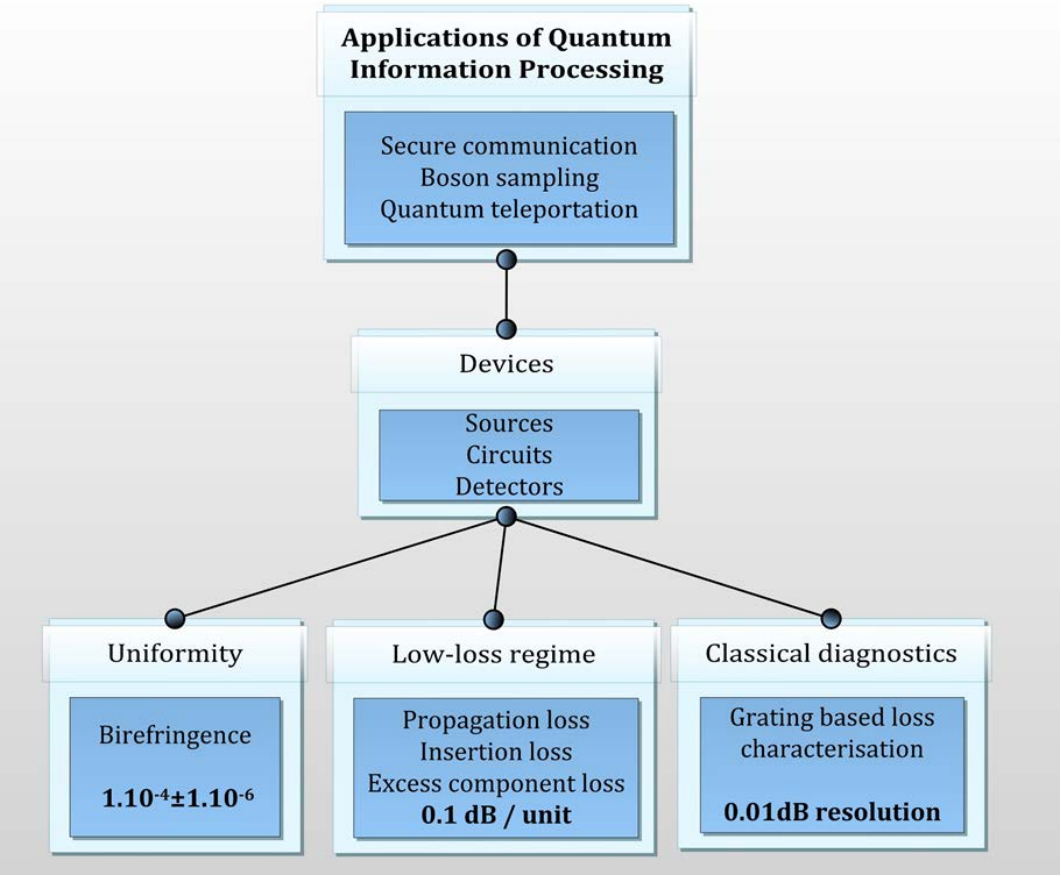

Figure 1.2 – Application, devices and technological requirements for silica-on-silicon quantum information processing platform.

1.3 Thesis synopsis

This thesis focuses on the engineering of the devices and their "classical" characterisation. Although primarily aimed at applications in QIP, the techniques and devices developed have applications in other areas of photonics, which will be highlighted in the relevant chapters.

Coupling loss is a critical element in the scaling of a network. Chapter 2 will introduce the physical concepts relating to this for integrated photonics systems. The discussion will be accompanied by a review of the technology platform and classical characterisation tools used throughout this thesis for the development and testing of these building blocks. This is presented with the intention of demonstrating the platform's suitability and potential for enhancing the component library available for QIP experiments.

Polarisation-dependant devices are important in the component library required for QIP experiments. Chapter 3 will describe a theoretical and experimental study for a novel implementation of integrated polarisers in planar waveguides based on tilted gratings. Chapter 4 will describe an extension of this work making use of the platform's added functionality for the fabrication of novel polarisation-dependent waveguide-based architectures.

Chapter 5 reports the development of the fabrication platform to implement waveguide-based heralded single-photon sources operating in the near-infrared and visible. The discussion also presents the project's technical achievements that can be used for the scaling of the platform and to extend its compatibility with high-power applications. The interfacing between arrays of fibres and waveguides is crucial for the scaling of the technology. Chapter 6 covers the development of a characterisation system to inspect commercial fibre v-groove arrays to determine their suitability for interfacing between silica-on-silicon technologies and fibre components.

The work in this thesis has been coupled with participation in and organisation of many education and engagement endeavours. Chapter 7 will outline how "traditional" research activities cannot be disentangled from researchers' social responsibility. It describes *experiments* designed to engage the public and school children in research and the fundamental optical science underlying this thesis.

Chapter 8 provides a summary of the findings of this thesis and proposes suggestions for future lines of investigation.

Chapter 2 Direct UV writing for an integrated waveguide platform

2.1 Introduction

The optical properties of devices are defined by the fabrication processes and the material properties used to make them. This chapter introduces tools for the design, production and testing of silica-on-silicon photonics integrated circuits that can be employed as building blocks in large-scale networks for experiments in quantum information processing (QIP).

The reader will first be presented with relevant background theory on planar waveguides to form an understanding of the platform's design parameters, highlighting its suitability for integration with low loss silica fibre platforms. The fabrication techniques for silica-on-silicon (SoS) wafers and chips through flame hydrolysis deposition (FHD) will then be discussed. The chapter will review the development of techniques for the fabrication of waveguides and gratings through direct UV writing (DUW), and outline detailed fabrication and control parameters of the system employed in this study. The discussion is supported with details on spectral characterisation methods compatible with this platform. Physical micromachining techniques for the packaging of devices will also be presented. The chapter will be concluded with an outlook of the technical work carried out in the context of this thesis.

2.2 Planar waveguides

Optical waveguides are used to guide light waves between different locations. “Fibre optics” are the most ubiquitous waveguide implementation, and optical integrated planar waveguides can be thought as their monolithic, “postage stamp size”, equivalent. An understanding of the transmission of light through planar waveguides is required for the integration of separate components, i.e. individual building blocks, into optical networks. This section presents fundamental waveguide structural properties and modelling tools that are used in the design of planar waveguide structures used throughout this study.

2.2.1 Ray propagation in waveguides

To appreciate how light travels into and through a waveguide, light can be described using a ray that zigzags through a material. *Ray theory* provides a reasonable, although incomplete, understanding of these coupling and propagation mechanisms. The following discussion is used to highlight how losses can occur from coupling between fibres and waveguides that form part of a larger photonics network. This section makes analogies to fibre optic ray theory, following the account in [32], which studies silica-based materials systems with characteristics similar to those of the platform considered in this study.

The transmission of light at a planar dielectric interface is governed by Snell’s law, given in equation (2.1).

$$n_1 \, sin\, \theta_1 = n_2 \, sin\, \theta_2 \qquad \textbf{(2.1)}$$

A beam incident from a material with refractive index n_1 will change its direction of propagation at the interface with a second material of refractive index n_2. The following study sets $n_1 > n_2$. With reference to Figure 2.1, the angle of the incident beam, θ_1, and transmitted beam, θ_2, are defined with respect to the normal to the interface. As θ_1 increases, the refracted wave is eventually transmitted orthogonal to the normal plane of incidence. This is the critical angle, θ_c, which is given by equation (2.2). Beyond θ_c, total internal reflection (TIR) occurs. The radiation is

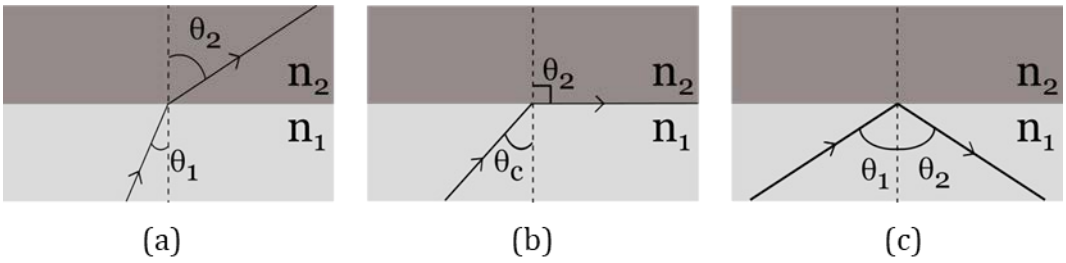

Figure 2.1 – Behaviour of a light ray incident on the boundary between two dielectric media with different refractive indices, for $n_1 > n_2$ (a) $\theta_1 < \theta_c$, transmission of refracted ray (b) $\theta_1 = \theta_c$, onset of total internal reflection (c) $\theta_1 > \theta_c$, ray confinement by total internal reflection.

entirely reflected and there is no transmitted wave in the second medium[1]. The critical angles for slab waveguides fabricated in this thesis are typically around 84^0 because of the index contrast of the silica platform considered. In the scenario where $n_1 < n_2$, TIR is not permitted as the critical angle does not have a real solution.

$$\theta_c = sin^{-1}\left(\frac{n_2}{n_1}\right) \qquad \textbf{(2.2)}$$

Figure 2.2 shows the structure of an optical waveguide that can be used to guide light by TIR. The waveguide consists of a core and cladding region, with indices of refraction n_1 and n_2 respectively. The constraints for TIR at the core-cladding interface region impose that $\sin\phi > n_2/n_1$. Light is launched into the waveguide at an angle θ_i from another medium with a refractive index n_0. For the geometry presented in Figure 2.2, $\sin\phi = \cos\theta$. Using the trigonometric identity $\cos^2 x + sin^2 x = 1$, and applying Snell's law at the interface between the core and the surrounding medium, it follows that light propagation by TIR in the waveguide can occur if equation (2.3) is satisfied.

[1] No energy is conveyed away from the surface provided the second medium extends an infinite distance from the boundary. A small disturbance does occur through an electric field that decays exponentially with distance away from the boundary, known as the evanescent field.

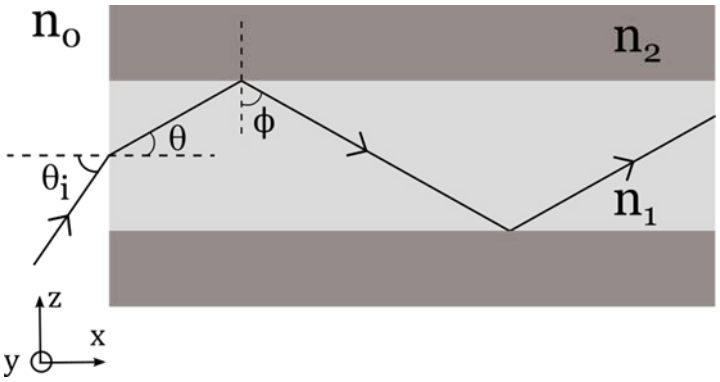

Figure 2.2 – Light ray propagation by total internal reflection. The launched light is within the cone of acceptance angles of the guiding structure, i.e. the numerical aperture of the wave guiding structure.

$$sin\ \theta_i < \left[\frac{n_1^2 - n_2^2}{n_0^2}\right]^{1/2} \tag{2.3}$$

The range of angles θ_i describes a cone from which light can be launched into the waveguide and guided by TIR. The light gathering efficiency of the waveguide is a function of the term on the right-hand side of equation (2.3). It is defined as the numerical aperture (NA), and is traditionally calculated when the surrounding medium is air, with $n_0 = 1$. The value of NA is then entirely dependent on the refractive indices of the core (n_{Co}) and cladding (n_{Cl}), as given by equation (2.4).

$$NA = \sqrt{n_{Co}^2 - n_{Cl}^2} \tag{2.4}$$

The NA is a useful parameter to assess the coupling efficiency of a system. From fibre theory, the loss due to mismatch in numerical aperture is given by equation (2.5) [33]. It has been assumed that the waveguides have an equivalent refractive index profile and core dimensions, and that the ray propagation characteristics in each medium are uniform.

$$\begin{aligned} Loss\ (dB) &= -20\ log_{10}\left(\frac{NA_2}{NA_1}\right) && NA_2 < NA_1 \\ Loss\ (dB) &= 0 && NA_2 \geq NA_1 \end{aligned} \tag{2.5}$$

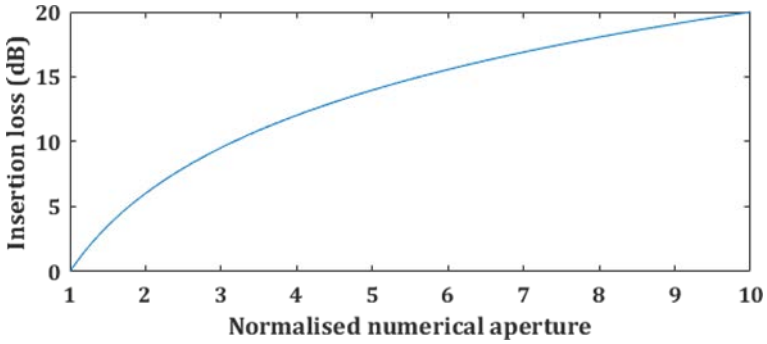

Figure 2.3 – Insertion loss as a function of mismatch of numerical aperture.

From equation (2.5), the transmission from a low NA system to a high NA system does not suffer from loss. The rays in the smaller cone are all contained within the larger cone of acceptance of the receiving medium. Loss occurs in the reverse direction of transmission. Mismatches in NA result in a very rapid increase of coupling loss. The normalised NA mismatch induced losses is shown in Figure 2.3. For connecting building blocks of photonics networks, it is therefore desirable for the NA of each component to be matched to each other to reduce coupling losses.

2.2.2 Optical modes in waveguides

The guidance mechanism presented so far permits light to travel in a waveguide through TIR. The spectra of rays that can be guided by TIR constitute the modes of the waveguides. There is a discrete and finite set of waveguide modes (or ray angles) that are permitted. These are determined by the waveguide thickness, *d*, and the NA for a given wavelength of operation, λ. The quantities are related through equation (2.6)

$$V = \frac{2\pi d}{\lambda} NA < m\pi, m = 0, 1, 2, 3... \quad \textbf{(2.6)}$$

For a waveguide of dimension $d = 6\,\mu m$ operating at $\lambda = 1.55\,\mu m$, a single waveguide mode ($m = 1$) is supported if $NA \leq 0.13$. For larger NA, higher order modes ($m > 1$) are permitted; the waveguides in this study have been designed to support single-mode operation and the following discussion assumes the waveguides are indeed single mode.

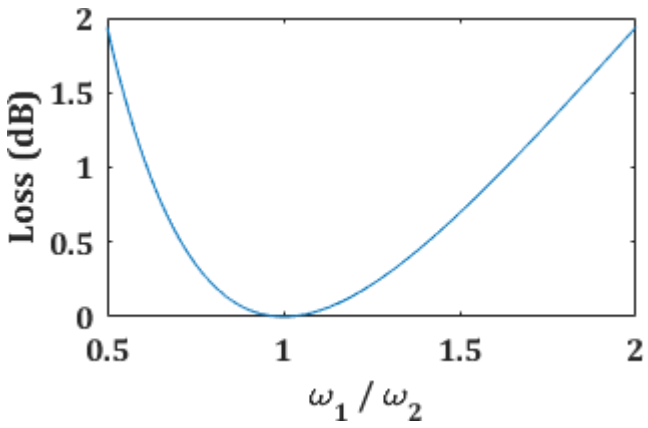

Figure 2.4 – Losses between two perfectly aligned Gaussian modes with different mode field diameters.

Each mode is uniquely represented by its modal characteristics. An important metric used to assess the efficiency of coupling between modes of independent waveguides is the intensity distribution of the optical power in each mode. For single mode waveguides, with NA similar to fibres, the distribution of the intensity of the waveguide mode, *I(z)*, can be approximated using a Gaussian function – see equation (2.7) [34]. With reference to Figure 2.2, the z-axis is taken as the normal of the core-cladding interface so that it describes the variation in the refractive index across the waveguide.

$$I(z) = I_0 \, exp\left(\frac{-z^2}{\omega_0^2}\right) \tag{2.7}$$

In equation (2.7) the quantity $d = 2\omega_0$ is the mode field diameter (MFD) of the waveguide; this is where the intensity of the field decreases to $1/e^2$ of its maximal value. The parameter permits the estimation of the coupling loss between two single mode devices (waveguides and/or fibres) with different MFD ω_1 and ω_2, and which are perfectly aligned. The loss due to modal mismatch is given in equation (2.8) [34], and plotted in Figure 2.4.

$$Loss\ (dB) = -20\ log\left(\frac{2\,\omega_1\,\omega_2}{\omega_1^2 + \omega_2^2}\right) \tag{2.8}$$

The propagation through the waveguide is uniquely characterised for each waveguide mode by the modal propagation constant, $\beta = k_0 n_{eff}$. An effective

refractive index, n_{eff}, is defined to describe the interaction of the mode with the waveguide geometry. The variable k_0 is the free space wavenumber and is given by $k_0 = 2\pi/\lambda = \omega/c$; ω is the angular frequency of the electromagnetic radiation. These values are directly related to the complex representation of a plane wave travelling in the x-direction, described by its electric field, $\bar{E}$, shown in equation (2.9).

$$\overline{E} = \overline{E}(y, z)\, e^{j(\omega t - \beta x)} \tag{2.9}$$

Single mode waveguides conventionally contain a pair of fundamental modes with different excitation orientations of the electric field, which represent the polarisation of the electric field. Both transverse electric (TE) and transverse magnetic (TM) modes can be supported in single mode waveguides. If the electric field is aligned along the y-axis, the TE mode is supported. If the electric field is aligned along the z-axis, the TM mode is supported. At other angles, both modes are excited. The difference in the propagation mode constant is indicative of the birefringence of the waveguide, $\Delta n = (\beta_{TE} - \beta_{TM})/k_0 = n_{TE} - n_{TM}$. The characterisation of these modes will be discussed further in section 2.6 and later chapters. The reader is referred to [35], [36] for further theoretical treatments of planar waveguides using Maxwell's electromagnetic equations.

2.2.3 Waveguide modelling

The following section provides an overview of waveguide modelling techniques. It introduces an analytical technique for the determination of the effective refractive indices of two-dimensional geometries, and describes numerical software packages and methods used to model waveguides fabricated in this study.

2.2.3.1 Effective index approach

The effective index method [37] is an analytical method to analyse two-dimensional waveguides with rectangular boundaries, such as the structure presented in Figure 2.5. A waveguide region has been formed by increasing the refractive index of the planar core layer by a constant value, Δn_w. The method assumes that the electromagnetic field in the waveguide can be separated along the z and y coordinates as defined in Figure 2.5; the waveguide mode propagates along the x-

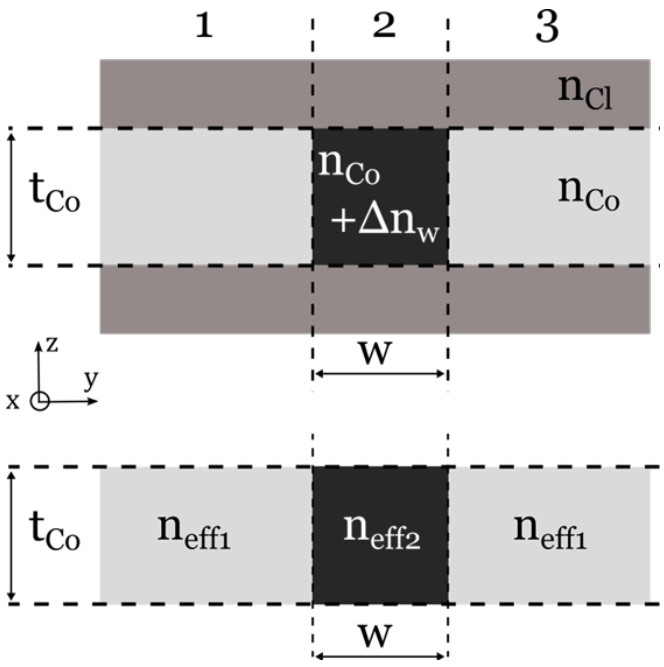

Figure 2.5 – Cross-section of the 2D waveguide for modal analysis through the effective index method. The waveguide is analysed as a set of 1D slab waveguides.

axis in this study. The methodology computes an effective index distribution for waveguide in regions 1, 2 and 3. The analysis yields a 1D refractive index profile. The 1D step index profile is identical to the waveguide geometry described previously, and NA and MFD waveguide parameters can be extracted from this. Measurements of the field provide MFD values in both z and y axes, which can be used to model the waveguide using numerical software packages that are described in the following section.

2.2.3.2 Numerical description of waveguide behaviour

The waveguide analysis described previously is restricted to rectangular geometry planar optical waveguides. Numerical methods are required to describe inhomogeneous cores, with graded-index profiles, such as the devices fabricated in this thesis. A 2D mode solver package (Photon Design ® FIMMWAVE) has been used in this study to determine the modal characteristics of the waveguide (Chapter 5). A numerical simulation software (COMSOL Multiphysics ®) has also been employed for the 2D propagation in waveguide structures with tilted gratings (Chapters 3-4).

The numerical methods rely on the discretisation of the geometry into lattice regions, in which the field is approximated in each element. The finite difference method (FDM) [38] uses rectangular grids to discretise the domain, and the effective refractive index of each section are resolved. The technique is suited for finding solutions of rectangular waveguides, with and without graded index profiles. Another technique used is the finite element method (FEM) [38], which defines grids with a triangular mesh to enable the analysis of waveguide structures with complex geometries. The technique enhances the resolution at regions of interest. The element contributions are assembled to form the effective index and numerical solutions to Maxwell's electromagnetic equations. FEM has been used extensively for the study of the interaction of light with gratings.

2.2.4 Factors of merit

The section above has introduced fundamental design parameters for the design of waveguide circuits for low loss integration into photonics networks. Single mode waveguide operation has been described in the context of the layer refractive indices, and the implications for the waveguide field intensity profiles have been presented. Single mode waveguides are characterised by pairs of polarisations modes, which will be used to establish birefringence in waveguides.

Waveguide NA and MFD properties permit the estimation of the connection loss between different platforms. The assumptions made on the multimode nature of the waveguide will cause the loss to be overestimated using NA as a metric. The MFD will provide a more accurate representation of losses between single mode components. Experimental measurements of this parameter can readily be inserted into modelling tools to compute waveguide mode profiles based on numerical solutions of the fundamental laws of electromagnetism. These will be used in Chapter 5.

2.3 Flame hydrolysis deposition for slab waveguide engineering

The following section provides details of flame hydrolysis deposition (FHD) used for the development of silica-based slab waveguide structures to provide an understanding of the nature of the devices used in this study.

2.3.1 Base wafer

Silicon wafers of diameter of approximately 15 cm (6 inches) are used as the base substrates for the fabrication of silica-based devices in this study. It is important to note that there is a large thermal expansion coefficient mismatch between silica and silicon: the linear thermal expansion coefficient of fused silica is $0.40\text{-}0.55\times10^{-6}$ K^{-1} [39], compared to $2.55\text{-}4.56\times10^{-6}$ K^{-1} for silicon from room temperature to 1500 K [40]. The thermal coefficient mismatch between the materials leads to an anisotropic distribution of stress between the layers [41], which can be manipulated during the consolidation process (section 2.3.3).

A buffer layer is used to alleviate the stresses between the silicon and silica. This consists of a silicon-oxide layer that is thermally grown on the base silicon. The thermal oxide growth happens through the oxidisation of the silicon in an oxygen rich environment [42]. It is likely that these thermal oxide layers have a linear expansion coefficient between that of fused silica and silicon due to the formation process, thus permitting more uniform anisotropic stresses across the wafer.

The formation of the oxide layer takes a period of approximately 20 days. The layers are grown in a high-temperature and wet environment. Wafers used in this process have been purchased commercially. The wafers used in this thesis have a thick thermal oxide, typically 15-17 μm. The thick-thermal oxide devices have been found suitable for the deposition of photosensitive core and overcladding layers on the surface through FHD. The thick thermal oxide also acts as the optical underclad in the final devices.

2.3.2 Layer deposition

Core and overclad layers with specific optical and material properties have been deposited by the FHD technique using the fabrication facilities at the University of Southampton's Optoelectronics Research Centre (ORC). This section describes the FHD process and wafer layer characterisation techniques that have been used to fabricate the wafers in this study.

2.3.2.1 Layer composition and refractive index control

Flame hydrolysis deposition is a planar fabrication process for silica glass layers. It is a comparable process to vapour-phase axial deposition (VAD) [43] and outside vapour deposition (OVD) [44] techniques that have been developed for the fabrication of silica fibre preforms. The reader is referred to [5] for a comprehensive review of the adaptations of these methods for planar fabrication in the ORC.

The FHD technique consists of the synthesis of fine glass particles that are deposited as a porous low-density soot on a planar wafer. The deposited soot is "sintered", or "consolidated", in a high temperature controlled atmosphere for the formation of a dense glass layer (section 2.3.3). The technique permits the production of low loss planar layers. The glass properties can also be tuned to modify the layer stresses. FHD allows high deposition rates and is an appropriate tool for developing and prototyping silica-based integrated optical circuits.

The formation of a silica soot takes place through a combination of two chemical reactions of silica tetrachloride ($SiCl_4$) in an oxyhydrogen burner. The dominant chemical reaction is temperature dependent. These are direct oxidation (>1200°C) and hydrolysis (<1200°C) of the $SiCl_4$, given by equations (2.10) and (2.11), respectively [45].

$$SiCl_4 + O_2 \rightarrow SiO_2 + 2Cl_2 \quad \textbf{(2.10)}$$

$$SiCl_4 + 2H_2O \rightarrow SiO_2 + 4HCl \quad \textbf{(2.11)}$$

A high pressure $SiCl_4$ vapour phase is created in a bubbler system (*SG Controls TD0197*) through the injection of nitrogen carrier gas into a high purity liquid $SiCl_4$. The vapour is cycled to the deposition system through a mass flow controller, which

is temperature compensated with respect to the air pressure and humidity of the lab environment. This permits comparative measures of the amount of precursor reaching the deposition system and reproducibility between fabrication runs.

The same chemical vapour processes are used to add dopants in the production process. The dopants permit the tuning of the glass layer properties in terms of the refractive index, thermal expansion coefficient, photosensitivity, and melting point [5], [46]–[48]. The dopants used in this study are germanium tetrachloride ($GeCl_4$), phosphorus trichloride (PCl_3) and boron trichloride (BCl_3). A summary of the effect of the addition of each dopant on layer properties has been summarised in Table 2.1, where arrows denote the increase (↑) or decrease (↓) of the layer property. $GeCl_4$ and PCl_3 gases are produced through the bubbling of the liquid precursors, in the same way as $SiCl_4$. BCl_3 is already a gas at room temperature and is used in its gaseous state; it is directly controlled via a mass flow controller.

Table 2.1 – Effect of dopants on properties of glass layers.

Dopant	Refractive index	Photo-sensitivity	Melting point	Thermal expansion coefficient
Germanium	↑	↑	↓	↑
Phosphorus	↑	↓	↓	↑
Boron	↓	↑	↓	↑

Soot layers are deposited with a 4-ring torch that is fed with gases from four lines. The halide precursors are combined with oxygen and hydrogen. An additional line is fed with argon to control the directionality of the flame. The torch is mounted pointing 46^0 downwards. A Teflon tube is placed approximately 15 cm in front of the torch pointing 8^0 downwards acting as an extract for the chlorides formed in the reactions. Figure 2.6 (a) shows a picture of the system depositing soot on 6-inch wafers.

Germanium and boron dopants are used for the fabrication of the core layer. The addition of germanium to the silicate matrix increases the refractive index; conversely, the addition of boron decreases the refractive index. Controlling the amount of dopants allows the control of the refractive index of the core layer. The core layer has a higher refractive index than the underlying thermal oxide. This produces a planar guiding layer. The germanium in the core layers enhances the material's photosensitivity in the UV when co-doped with boron [48], which is used for subsequent definition of buried channel waveguides (section 2.4). Boron and phosphorus dopants are added to the flame for the formation of the overclad layer. The dopant levels are controlled to permit the matching of the refractive index to the underclad and offer good mode matching to silica fibre. The addition of phosphorus and boron also reduces the consolidation temperature to permit sintering at lower temperatures and maintain the integrity of the layers during the consolidation process.

2.3.2.2 Control of layer thickness

The devices are fabricated on silicon wafers with a thick (16 μm) thermal oxide, which serves as an underclad and isolates the evanescent field of planar modes from the silicon wafer. Up to six 6-inch (150 mm) wafers can be mounted on a rotating platform, which is heated at 180^0C to ensure the evaporation of chlorides and excess water to the extract system. The torch is translated across the turntable – see Figure

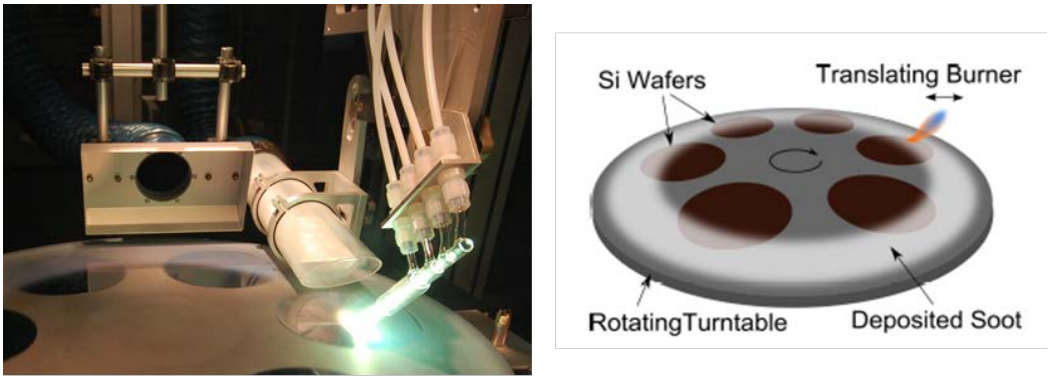

Figure 2.6 – (a) Photo of the FHD system in operation. Soot is deposited on 6-inch silicon wafers by a doped hydroxide flame. (b) Diagram of the FHD turntable system, provided by P. L. Mennea.

2.6 (b) – where the speed is controlled as a function of the torch position to provide a uniform thickness deposition of the layer per pass. The uniformity of the final glass can typically be measured as a few hundred nanometres over the wafer (Section 2.3.4). The thickness of the final glass layer with each deposition pass has been determined empirically as ~0.5 μm. The desired thickness is obtained by passing the torch over by an appropriate number of passes. Fine tuning is achieved via the torch translation speed.

2.3.3 Layer sintering

The sintering, or thermal consolidation, of the deposited soot is the final process step in the fabrication of the planar layer. The thermal processing of the soot defines the structural and optical properties of the glass. The processes used in this thesis are based on the consolidation parameters established during the development of the FHD process in the ORC [5]. This section provides a brief overview on the process.

Following the soot deposition, the wafers undergo thermal processing to produce a dense glass layer; a typical temperature profile is shown in Figure 2.7. After deposition, the wafers are transferred immediately to an adjoining furnace (*Severn Thermal Solutions SP2030*). The temperature of the furnace is taken to 600°C, where the wafers are held in an oxygen-helium environment. The temperature of the furnace is increased at a constant rate (ramp 1) to the layer's consolidation temperature, T_C. The wafer is held at the consolidation temperature for a period of 2-3 hours. The temperature is then reduced to 600°C (ramp 2), followed by a rapid temperature reduction to room temperature.

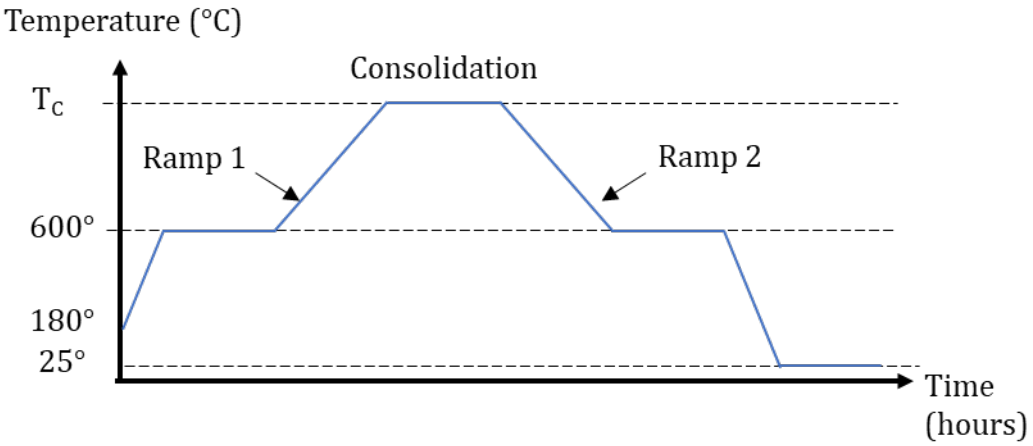

Figure 2.7 – Furnace temperature control profile for the sintering of FHD soot. Ramps 1 and 2 are controlled at 5^0C/min. The consolidation temperature, T_C, varies and has been empirically determined for core and cladding layers.

The temperature levels and ramp rates affect the optical quality and structural integrity of the layers. The soot dopant composition determines the consolidation temperature. The overclad doping has been controlled to permit the sintering at a lower temperature, which maintains the integrity of the layers. The consolidation temperature of core and cladding layers have been empirically established: typically for a core layer, T_C = 1360^0C and for cladding layers, T_C = 1100^0C.

Glasses with lower consolidation temperature generally require a longer time of consolidation, and vice versa. The longer consolidation time can cause added dopant volatility, compromising the structural integrity of the layers. The ramp rate also affects the optical quality of the layers, as a slow ramp rate will cause the soot sitting too long near its consolidation temperature and cause an increase in dopant volatility.

The cool down rates will affect the quality of the optical layer formed. This is a compromise between avoiding phase separation and crystallisation induced cracking from slow cooling and wafer warping from rapid cooling. The cooling rate for temperatures above 600^0C have the greatest impact on the layer uniformity and composition. The cooling rates for temperatures between 600^0C and room temperature is less critical as cracking is less likely to occur in these temperature regimes.

2.3.4 Layer material properties

The fabricated FHD layers are characterised for information on their optical and structural properties to assess the suitability of the planar platform for subsequent processing.

Layers are characterised using a prism coupling measurement apparatus (Metricon 2010 Prism Coupler). The technique can characterise thin films in terms of their refractive index, *n*, and thickness, *T*. It uses a laser beam directed at a prism, which is reflected onto a photodetector. The prism is brought in contact with the planar dielectric medium, and the angle of incidence of the laser beam, θ, is varied by rotating the sample. At certain angles, coupling to the m^{th} mode (m = 0, 1, 2…) of the planar layer from the prism is permitted, causing a drop in the light intensity on the photodetector. The quantities are related by the "mode equation" [49], given in equation (2.12).

$$\frac{2\pi}{\lambda} * n\, cos(\theta) * T + \Psi_{10} + \Psi_{12} = m\pi \quad (m = 0, 1, 2...) \qquad (2.12)$$

In equation (2.12), λ is the wavelength of the laser, and Ψ_{10} and Ψ_{12} are the Fresnel phase shifts induced from the film-air and film-substrate interfaces, respectively.

The technique provides thickness and refractive index measurements with a quoted accuracy of ±0.5% and ±0.0005, respectively. Test wafers with thin a thermal oxide (~1 μm) are usually fabricated during the same FHD and consolidation process and these are used for the characterisation. Wafers are characterised at multiple points to assess uniformity. The measured thickness and refractive index are used to design gratings, and give an indication of whether the wafers are single mode or multimode. The calculated parameters permit the modelling of the structures of waveguide structures.

2.3.5 Process flow overview

An overview of the final devices is shown in Figure 2.8. The key characteristics of a wafer are the core thickness and its refractive index contrast with respect to the undercladding. The overcladding and undercladding are usually index matched to allow for better mode matching to an optical fibre. These permit the determination

of the NA and theoretical V-number of the fabricated slab waveguide. The effect of the dopant concentration on the stresses in the layers to control the birefringence of the layers will be investigated in Chapter 5. The wafers have been diced into chips using a precision dicing machine (section 2.7) prior to further processing.

***FHD clad layer**, doped with B and P.*
Thickness 15-17 µm.
Refractive index matched to underclad.

***FHD core layer**, doped with Ge and B.*
Photosensitive. Thickness: 4-6 µm. Refractive index contrast 0.2-0.5% greater than cladding.

***Thick thermal oxide underclad layer**.*
Thickness: 15-17 µm. n = 1.44

***Silicon wafer**. Thickness: 1 mm.*

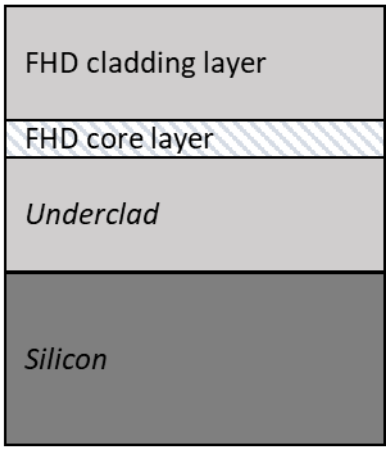

Figure 2.8 – Schematic of the wafers fabricated by FHD.

2.4 Direct UV writing

The direct UV writing employed in this thesis refers to a laser inscription technique that has been applied for the fabrication of channel waveguides in a SoS planar platform. The fabrication of buried waveguides in germanosilica planar layers was first studied by Svaalgard et al. [50]. The research demonstrated the use of a laser beam, with a wavelength in the photosensitive region of a material, focussed into a photosensitive core area that causes a change of refractive index leading to a channel waveguide region [51]. This section reviews the mechanisms for photosensitivity and fabrication process for buried waveguides in germanosilicate glasses.

2.4.1 Photosensitivity

The fabrication process relies on the presence of a photosensitive core layer that will later be used to define buried channel waveguide circuits. The mechanisms for sensitivity are considered as a combinatory set of effects caused during the exposure to ultraviolet (UV) radiation [52]. The following section describes the mechanisms for photosensitivity and its enhancement.

2.4.1.1 Mechanisms of photosensitivity

Hill et al. first observed a photo-induced increase of the refractive index of germanium-doped silica fibres using an argon-ion laser at wavelength of 488 nm [53]. It was later discovered by Lam and Garside that the magnitude of the induced refractive index in the core was found to be proportional to the square of the usable writing power, which was interpreted as a two-photon absorption process causing the photosensitive phenomena [54]. Further experimental investigation by Hand and Russell proposed a model where the radiation energy caused charge transfers in irradiated germanosilicate materials with lattice defects, leading to a modulation of the refractive index [55]. The effect is qualitatively described in the following paragraphs.

Germanosilica lattices may exhibit defects if, for instance, there is a lack of oxygen during the fabrication. These types of defects are referred to as oxygen deficient centres (ODC). An example of an ODC is a neutral oxygen vacancy centre, causing a Si-Ge bonding, as illustrated in Figure 2.9 (a); an analogous defect is caused for a Ge-Ge bond. Another type of defect is the Ge^{2+} defect, illustrated in Figure 2.9 (b). These "colour centres" are understood to cause absorption in the 240-250 nm region [55] and contribute to germanosilica's photosensitivity.

The aforementioned study of photosensitivity in germanosilica suggest that UV irradiation causes an increase in the concentration of ODCs. This is achieved through the excitation of an electron, which is then released in the glass matrix – see Figure

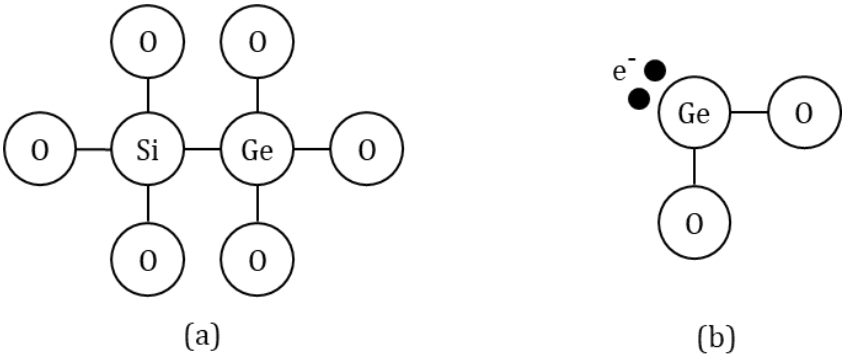

Figure 2.9 – Defects in germanosilica (a) Neutral oxygen vacancy defect. (b) GE^{2+} defect.

2.10 (a). In the scenario of Figure 2.10 (a), the electron breaks the Si-Ge bond, resulting in a GeE' centre that may recombine to cause a luminescence. The free electron may also diffuse through the matrix, eventually being trapped at Ge(1) or Ge(2) centres to form Ge(1) – see Figure 2.10 (b) – and Ge(2) defects, respectively. A Ge(1) centre corresponds to a Ge atom being the centre of four Si-O bonds and a Ge(2) centre corresponds to a Ge atom being the centre of three Si-O and one Ge-O bond.

The image however is incomplete, and many other mechanisms have been reported to account for this increase in photosensitivity [52], [56]. These include the densification of glass prompted by the laser irradiation in the 240-250 nm region. The UV radiation region causes bonds to break and gives rise to modification of the refractive index [52]. Addition of other dopants, such as boron, to a glass matrix has been noted to increase the stress effects, resulting in increased photosensitivity [48].

Extensive studies have not yet been conducted on the mechanisms leading to a photo-induced refractive index change on planar SoS platforms. It is likely that a combination of both theories account for this effect in the direct UV writing process.

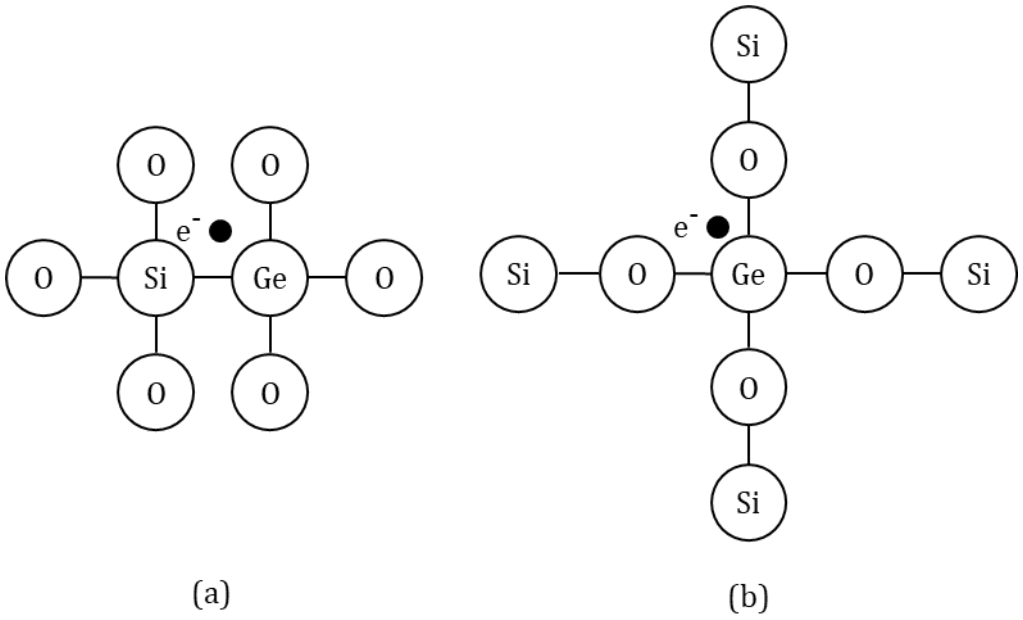

Figure 2.10 – (a) Direct UV exposure effect. (b) Ge(1) defect.

2.4.1.2 Hydrogenation for photosensitivity enhancement

Samples used in this work are hydrogenated to improve the achievable refractive index increase possible. The photosensitivity of germanosilica glasses is known to be enhanced through the high pressure "loading" of hydrogen into samples, permitting refractive index increases of up to 10^{-2} [57]. The hydrogenation promotes the photosensitivity through its reaction with the glass matrix's colour centres. Samples are hydrogenated at 120 bar in a high-pressure hydrogen cell. One disadvantage of using hydroxyl is the formation of an absorption band near 1400 nm, resulting in optical losses near telecoms wavelengths. The use of deuterium, which introduces OD^- groups with absorption bands nearer 1900 nm, may potentially reduce losses [58].

Hydrogen diffuses out of the glass matrix when removed from the hydrogen-rich environment, resulting in reduced photosensitivity with time. This "outgassing" is inhibited by storing samples in liquid nitrogen prior to UV writing. The time to write a waveguide is ~2 mins and little change is observed over this writing period. For the scaling towards larger and more complex devices, where multiple waveguides must be defined, the outgassing may influence the uniformity between successively fabricated waveguides.

This section has outlined the mechanisms permitting the fabrication of buried waveguides and gratings through photo-induced refractive changes from UV irradiation of germanosilica. The formation of waveguides is caused through the combinatory effects of the formation of ODC defects in the crystal lattice and glass densification. The grating formation also relies on these processes for the simultaneous definition of waveguides and gratings, which will be discussed in section 2.5. The implementation of direct UV writing is presented in the next section.

2.4.2 Waveguide formation

The DUW system used in this study uses a frequency-doubled argon ion laser (LEXEL™ 95-SHG) operating at a wavelength of 244 nm. A sample is placed on an ultra-high precision air bearing stage system (Aerotech™ ABL 9000) that is computer controlled. The stage control system (Aerotech™ A3200) provides positioning precision of the order of a few nanometres.

The refractive index change is a function of the energy illuminating the sample, i.e. the "fluence". The fluence (kJ/cm^2) is given by equation (2.13) and defined in terms of the power density of the focussed laser spots, I_{UV} (kW/cm^2), the spot diameter, d (cm), and the translation speed of the stages, v_{trans} (cm/s).

$$F = \frac{I_{UV} * d}{v_{trans}} \quad \textbf{(2.13)}$$

The spot diameter is a critical parameter in the fabrication process. For the waveguide generation, the size defines the horizontal width of the channel. The vertical width is largely set by the thickness of the core layer. The waveguide channel dimensions should ideally be well matched to fibre profiles for minimal insertion loss. The spot size has been empirically determined of having a mode field diameter of ~6 μm.

2.4.3 DUW waveguide description

The mechanisms for the formation of a photo-induced buried channel waveguide have been presented in this section. The combination of defects and densification effects in the glass lattice permit the increase of the refractive index of the fabricated planar chips through ultraviolet irradiation at 244 nm. Hydrogenation of the fabricated chip in a high-pressure hydrogen chamber has been used to enhance the photosensitivity mechanisms. The DUW system permits the "drawing" of waveguides across a chip, and the waveguide guiding properties are determined by fluence. The system has been employed to add functionality on chip, such as beam-splitters with waveguide profiles matched to other components of the DUW catalogue [59]. This is particularly attractive for the scaling of complex photonics networks.

The waveguide's refractive index profile, n_w, is described by equation (2.14) in terms of the axes indicated in Figure 2.11. In equation (2.14), n_{Co} is the refractive index of the core of the slab waveguide and Δn_w the photo-induced refractive index modulation. The horizontal Δn_w, *along* the y-axis, is associated to the spot size of the laser writing system, which is assumed to have a Gaussian spot size of radius σ. The refractive index of the waveguide along the writing (x) axis is constant for straight channel waveguides. The equation assumes that the DUW does not induce a

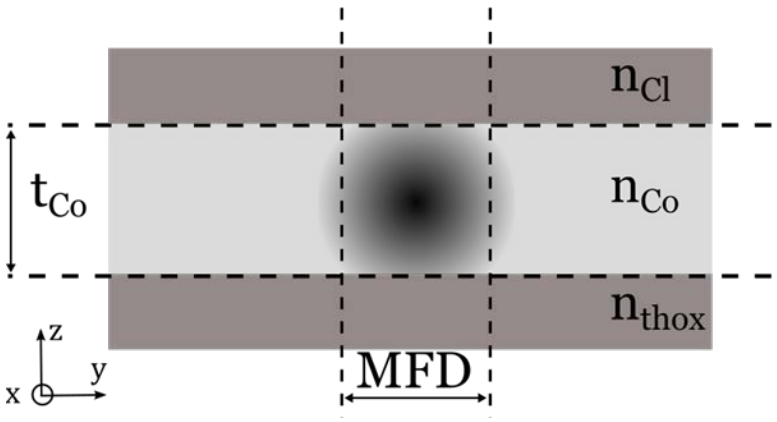

Figure 2.11 – Cross-section of buried waveguides fabricated by DUW.

significant modulation of the refractive index in the non-photosensitive cladding, and that Δn_w is constant in the z-axis. The model will be used as the basis for the modelling waveguides in Chapters 3 and 4.

$$n_w(x,y) = n_{Co} + \Delta n_\omega \, exp\left(-\frac{y^2}{\sigma^2}\right) \qquad \textbf{(2.14)}$$

The spatial modal characteristics of the fabricated waveguide are schematically represented in Figure 2.11. The vertical MFD of the waveguide is largely defined by the thickness of the core layer, t_{Co}. The horizontal MFD is defined by the profile of the refractive index modulation through the DUW, and is largely controlled by the fluence. Optimal coupling to single-mode fibre requires tailoring the waveguide MFD, and will be discussed further in Chapter 5.

2.5 Integrated grating fabrication through direct UV writing

A grating can be described as a periodic perturbation of any waveguide characteristic along the direction of propagation. Gratings are used in many integrated photonics devices to add functionality to waveguide-based circuits. The gratings developed in this study have been fabricated through DUW to produce integrated devices with periodic changes in the refractive index – see Figure 2.12. This section presents details of the design and fabrication of gratings for the DUW platform. As a preamble, background on the fabrication and behaviour of photo-induced gratings is presented.

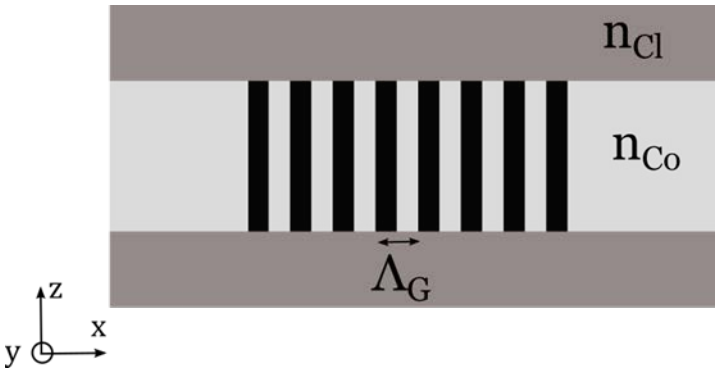

Figure 2.12 –Waveguide with a periodic refractive index change in the direction of propagation of the electromagnetic radiation. Λ_G is the grating period.

2.5.1 Photo-induced grating

Investigatory work and technological advancements on UV photo-induced gratings stem from the field of fibre gratings. The physical mechanisms are relevant to the material platform used in this study. The following section describes relevant concepts that have been applied to the fabrication of planar waveguide gratings by DUW.

2.5.1.1 Fabrication

Morey, Meltz, and Glenn first demonstrated the use of UV irradiation at wavelengths of 244 nm for the interferometric formation of holographic gratings by side illumination in silica fibres [60]. The interference pattern used to generate the gratings was formed by splitting a radiation into two beams of equal intensity and recombining them after having travelled equal optical path length. Interferometry and phase-mask methods have been employed for the generation of gratings through the generation of an interference pattern.

The techniques fundamentally rely on the modulation of the interference pattern during the exposure process. The control of sample positioning [61] and beam intensity [62] enabled demonstrations of advanced fibre Bragg grating structures, such as chirp and apodisation, through multiple exposure of the gratings. The technique was advanced through the modulation of the phase in the beam path, resulting in faster and more efficient fabrication procedures [63]. The interferometric control principles were combined with a dual-beam DUW

fabrication process in the ORC (section 2.5.3), resulting in the first demonstration of simultaneously UV-written waveguides and gratings in planar devices [64]. The following section describes the types of gratings that are formed through this integrated planar grating fabrication process.

2.5.1.2 Grating types

The formation of gratings within photosensitive core layers has been described as a function of the photo-induced process. Two principle dynamic regimes can be identified, namely Type I and Type II gratings [65].

Type I gratings are characterised by a refractive index change that takes place below the damage threshold of the glass. The process occurs through the excitation of the colour centres that are responsible for the photosensitivity in germanosilicate glass that are exploited in the waveguide formation by DUW (section 2.4.1). These gratings are usually associated with a positive refractive index change. [65].

Type II gratings, also called “damage gratings”, are formed by high power lasers operating above the damage threshold of the glass. They cause a positive refractive index change of typically an order of magnitude greater than Type I gratings [65]. The gratings described in this study are largely formed through a Type I process, which determines the grating spectral response and characteristics. The following section describes the behaviour of gratings considered in this study.

2.5.1.3 Grating behaviour

Photo-induced gratings can be considered as diffraction gratings. A point structure or a slit of the order of magnitude of an incoming electromagnetic radiation will cause diffraction. A set of such structures periodically spaced by a distance of the same order of magnitude as the wavelength constitute a diffraction grating, as illustrated in Figure 2.13. The field may be reflected or transmitted by the grating and will give rise to a diffraction pattern. An outstanding feature of this pattern is its equally spaced amplitude maxima, namely the diffraction orders. In addition, for narrow slits, the amplitudes of all modes are equal in intensity. In reality, gratings have a finite linewidth and shape. The intensity pattern is apodised and less power is diffracted into the higher order modes.

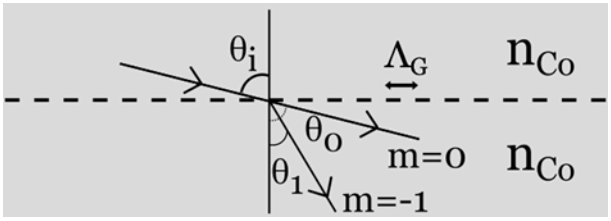

Figure 2.13 – Diffraction of light by a grating.

Given a radiation of wavelength λ incident on a grating structure with period Λ_G at an angle θ_i, the diffraction angle θ_m for the m^{th} radiation mode is governed by the grating equation [66]:

$$sin\,\theta_m + sin\,\theta_i = m\frac{\lambda}{\Lambda_G} \qquad \textbf{(2.15)}$$

Equation (2.15) predicts the direction where constructive interference can occur and can be used to obtain the resonant wavelength for the coupling between two modes. First order diffraction usually dominates in the type of gratings considered in this study [67]. Bragg gratings are fabricated to permit contra-directional coupling of the waveguide mode – see Figure 2.14 (a). One important implication of equation (2.15) is that a system can be engineered to preferentially diffract the radiation into a selected order by tilting the grating planes and effectively changing θ_i. This can lead to the coupling to modes outside of the waveguide as illustrated in Figure 2.14 (b).

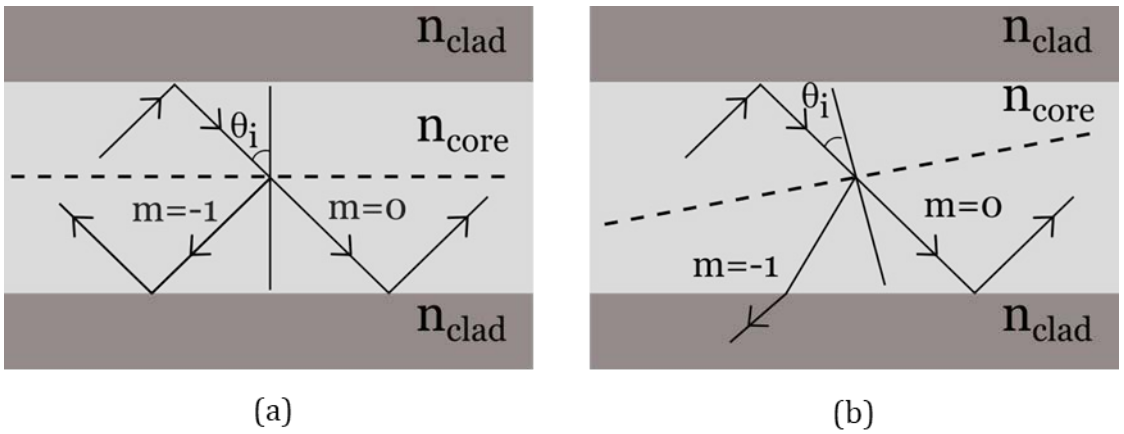

Figure 2.14 – (a) Ray representation grating acting as a contra-directional coupler. (b) Modification of diffraction conditions through the tilting of the grating planes.

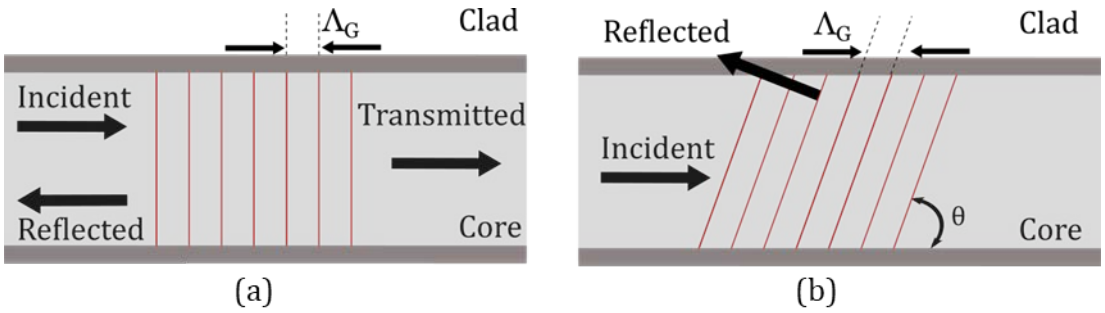

Figure 2.15 – (a) Bragg grating for contra-directional coupling. (b) Tilted grating for coupling out of the waveguide core.

Two main classification of gratings are considered in the context of this study. These are Bragg gratings and tilted gratings, illustrated in Figure 2.15 (a) and (b), respectively. Tilted gratings are oriented at an angle to the propagation axis and Bragg gratings have their grating planes normal to the direction of propagation of the planar wave front.

Contra-directional couplers usually employ Bragg reflectors as narrowband notch filters. They are characterised by a narrow bandwidth spectral response which can be observed through the analysis of the reflected and transmitted spectrum [67]. These have found applications for distributed feedback lasers, external fibre cavity semiconductor lasers, band stop filters and sensing applications [68].

Tilted gratings have the distinctive feature of permitting strong enhancement of coupling out of the core. This can be either through forward or backward propagating cladding modes that propagate through the cladding layers. A limited range of small and large tilt angles permit a diffracted mode to enter this regime. Outside of this range, broadband radiation is permitted out of the core through radiation modes [69]. Tilted gratings can provide wideband grating structure devices around the central design wavelength. Gratings in these regimes of operation have been used as in-fibre grating taps [70] and optical spectrum analyser devices [71], [72], as well as for sensing applications in fibre [73], [74] and planar waveguides [75]–[78].

2.5.2 Grating design

This previous section has reviewed the fabrication process and behaviour of photo-induced gratings. The following section highlights the principles of operation to assist in the design of the structures.

2.5.2.1 Bragg gratings

The periodic perturbation in a waveguide transfers power between two propagating modes if they are quasi-phase matched. The condition stipulates that a periodic perturbation with period Λ_G will permit coupling between two modes with propagation constants β_1 and β_2 if equation (2.16) is verified. In equation (2.16) K_G is amplitude of the grating wave-vector [67], [68].

$$\beta_1 - \beta_2 = \pm\frac{2\pi}{\Lambda_G} = \pm K_G \qquad \textbf{(2.16)}$$

The architecture of a Bragg reflector and its corresponding k-vector description are shown in Figure 2.16 (a) and (b). For the case of counter-propagating modes, $\beta_1 = -\beta_2 = 2\pi n_{eff}/\lambda$. Substituting into equation (2.16) yields the Bragg equation given by Equation (2.17).

$$\lambda_B = 2\, n_{eff}\, \Lambda_G \qquad \textbf{(2.17)}$$

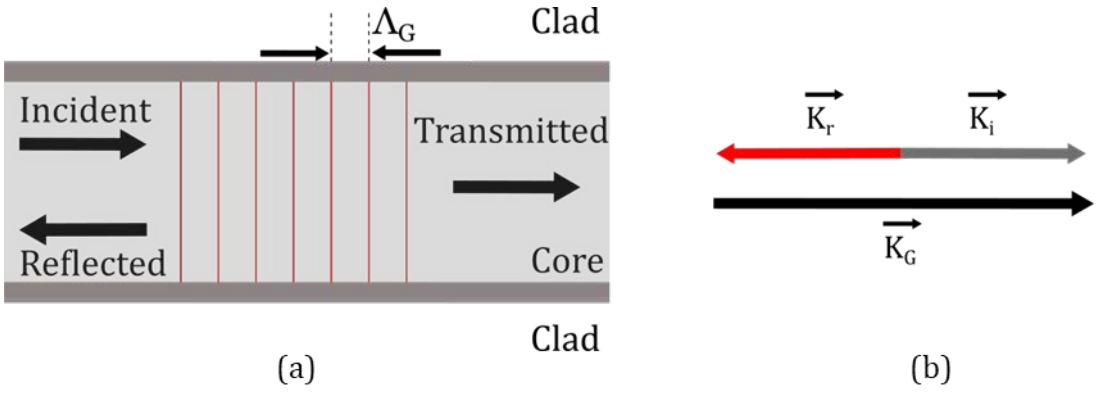

Figure 2.16 – (a) Transmission characteristics of integrated Bragg grating (b) K-vector description of the Bragg gratings.

Equation (2.17) permits the calculation the grating's resonant (Bragg) wavelength, λ_B, for a given of the grating period, Λ_G. The grating properties are related to its effective refractive index, n_{eff}.

2.5.2.2 Tilted gratings

The k-vector description can be readily extended to design tilted gratings [79], [80]. Figure 2.17 (a) describes a tilted grating oriented at an angle θ with respect to the direction of propagation. The k-vector description of the architecture is described in Figure 2.17 (b) and given by equation (2.18).

$$\overline{K_r} = \overline{K_i} + \overline{K_G} \qquad \textbf{(2.18)}$$

Optimal coupling occurs when the incident and reflected k-vectors have equal amplitudes. The amplitudes of the k-vectors are related by $|\overline{K_R}| = |\overline{K_G}|/(2\cos\theta)$. The grating period is then obtained by equation (2.19).

$$\Lambda_G = \frac{\lambda_r}{2\, n_{eff}\, cos\,\theta} \qquad \textbf{(2.19)}$$

The optimal angle of radiation from the waveguide, δ, is related to the tilt angle, θ, by $\theta = \pi - 2\delta$. The control of the grating period can be used as a supplementary design tool to design gratings with preferential radiation angles. In the context of this study, the extraction angle is 90^0 for gratings with tilt of 45^0. For $\theta > 45^0$, the

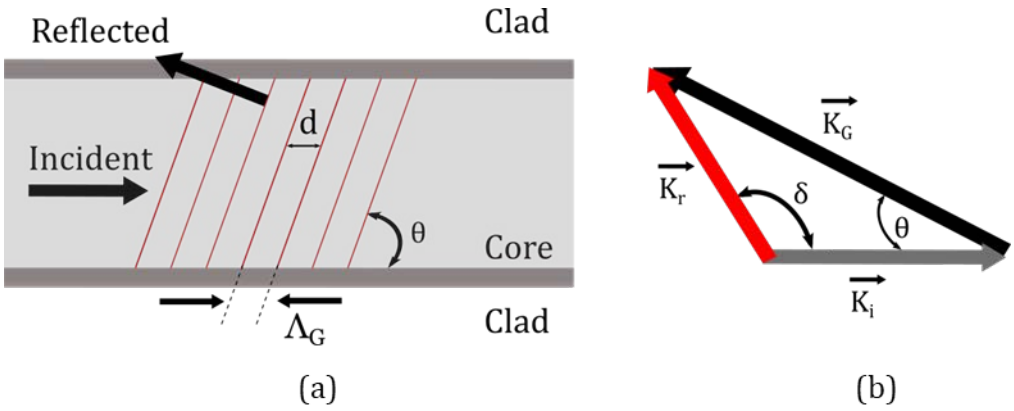

Figure 2.17 – (a) Tilted grating representation. (b) K-vector description of tilted gratings.

reflected radiation will be coupled to a forward propagating mode. For $\theta < 45^0$, the reflected radiation will be coupled to a backward propagating mode.

2.5.3 Simultaneous fabrication of waveguides and gratings

The design principles for gratings structures have been described in the previous section. The k-vector argument permits the design of Bragg gratings and titled gratings operating around at central resonant wavelength. The following section describes the tools for the simultaneous fabrication of gratings and waveguides by direct UV writing.

2.5.3.1 Dual-beam DUW system

An incident radiation is split on a beam splitter with an equal splitting ratio; both beams travel equal optical paths with distances within the coherence length of the laser (~10 mm) and are focused onto the sample to induce a change in the refractive index. An interference pattern is created at the focus of the two beams in the core layer of the chip. The half-angle of the intersection, γ, inherently defines the grating period, Λ_G, for a given UV radiation wavelength, λ_{UV}. The relationship is defined in equation (2.20) [65].

$$sin\ \gamma = \frac{\lambda_{UV}}{2\,\Lambda_G} \qquad \textbf{(2.20)}$$

For Bragg gratings operating near 1550 nm, γ = 13.1°, using Λ_G = 536 nm from equation (2.17). The system permits the fabrication of gratings and waveguides using different interferometer boards. Waveguides and gratings at wavelengths near 800 nm have been demonstrated with this scheme [81].

The DUW system can be controlled to fabricate tilted gratings, in which the grating phase planes are angled with respect to the propagation axis of the waveguide. The fabrication requires the rotation of the stage where the sample is positioned, as shown in Figure 2.18. The grating period, Λ_G, must be compensated as the stage is rotated by an angle, θ, to maintain a central reflectivity around the designed central wavelength, λ_B, according to equation (2.21). This is also achieved through the modulation of the interference pattern to detune from the effective resonant

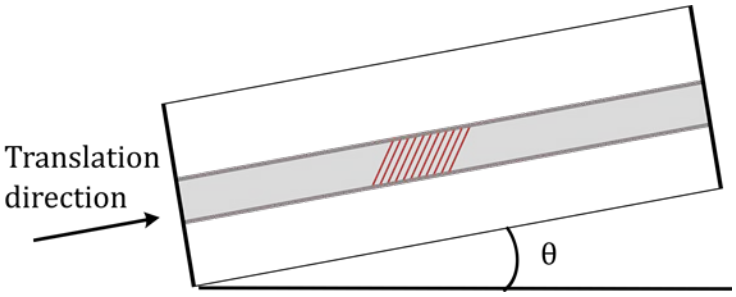

Figure 2.18 – Fabricated tilted grating device. The sample is rotated by an angle of θ during the writing procedure.

wavelength (section 2.5.4) and has permitted the fabrication of integrated waveguides and gratings with small angles of tilt [82].

$$\lambda_B = 2\, n_{eff} \Lambda_G (cos\ \theta) \qquad \textbf{(2.21)}$$

The waveguide and grating writing process is shown in Figure 2.19. The interference pattern is controlled to simultaneously define the waveguide and gratings through the modulation of the phase of the interferometer. Without modulation, the increase in the refractive index is constant and defines a waveguide channel in the core layer. A modulation of the interference pattern produces a periodic variation of the refractive index that forms a grating structure.

Initial investigations were through the modulation of the beam intensity through an acousto-optic modulator in the beam path. The technique reduced the power available and degraded the writing quality. The control of the phase of the beams of the interferometer was implemented, which significantly improved the system by increasing the writing speed and the achievable grating contrast. The phase modulation system was implemented in the ORC prior to this work, and a comprehensive report of this development can be found in [7]. The modulation scheme is described in the following section.

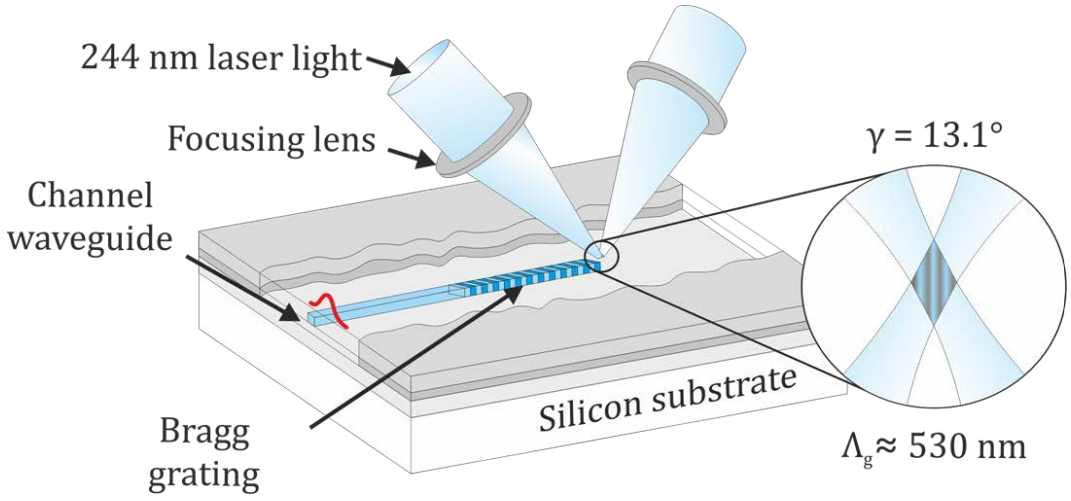

Figure 2.19 – Diagram of DUW setup for simultaneous generation of waveguides and gratings.

2.5.3.2 Electro-optic modulation

The control of the interference pattern is achieved through the modulation of the effective optical path length of one of the beams of the interferometer. The current scheme uses an electro-optic modulator (EOM) comprised of a deuterated potassium dihydrogen phosphate (KDP) crystal. A polarised beam propagating along the z-axis of the crystal incurs a phase change, $\Delta\Phi$, as a function of the electric field applied across the crystal. The relationship between $\Delta\Phi$ with and the voltage applied, V, is given by equation (2.22) [83].

$$\Delta\phi = \frac{\pi}{\lambda} n_0^3 r_{63} V L \qquad \textbf{(2.22)}$$

In equation (2.22), n_o and r_{63} are the electrical properties of the crystal and are available in the literature; λ is the wavelength of operation. The crystal's path length, L, permits the beam to accrue a large phase shift as it travels through the crystal. The crystal is mounted between two electrodes and oriented to allow good modulation of the beam. The crystal has been shown to have a linear optical phase shifts for voltages of 0-10 kV [7]. The control of the modulation process will be discussed further in the following section

2.5.3.3 Control system for grating fabrication

An overview of the DUW optical and control system is shown in Figure 2.20. The optical system is comprised of a beam expander that collimates the incoming laser radiation to route the laser through free-space optics without damaging them. The EOM is placed in one of the two arms of the interferometer setup to modulate the optical path length of the propagating laser beam. The sample is placed on the high-precision stages, and aligned vertically for the two focused laser beams to overlap in the core layer of the sample. The photoluminescence of the hydrogen loaded chips is used as an aid to ensure that the sample is flat so that the incoming radiation is always in focus in the core layer to maximise the refractive index increase.

The control system operates the stages and the modulation signals for the EOM through a programmable interface on a computer. The stage control system provides positioning precision of the order of a few nanometres, i.e. fractions of grating periods. For the definition of a grating, a position synchronised output (PSO) digital signal and a constant analogue output signal are used to control an integrator circuit, creating a sawtooth signal. The signal is routed to a high voltage amplifier (Trek™ 610E), which is used to apply an electric field across the EOM and induce a phase shift in the transmitted beam. The integrator's digital PSO control signal and analogue voltage output are shown in Figure 2.21.

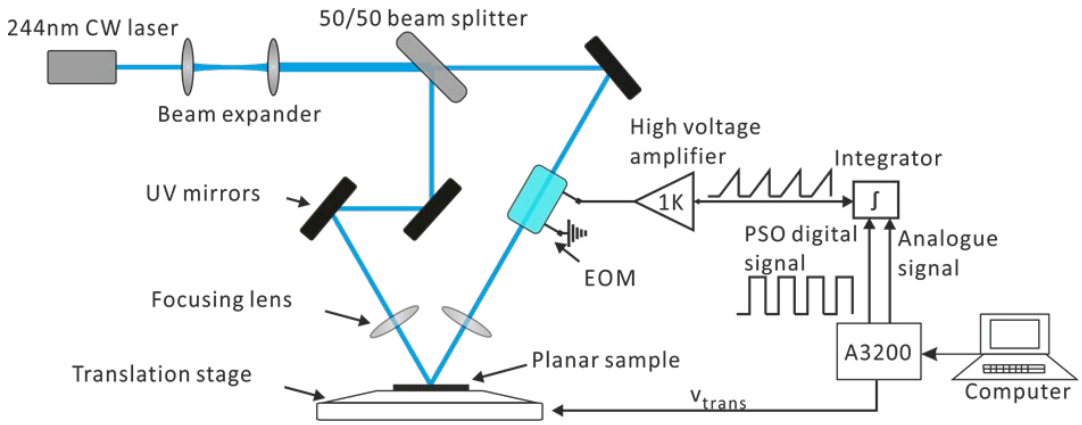

Figure 2.20 – Direct UV writing system with EOM control elements. Nomenclature: PSO: position synchronised output. v_{trans}: stage translation speed.

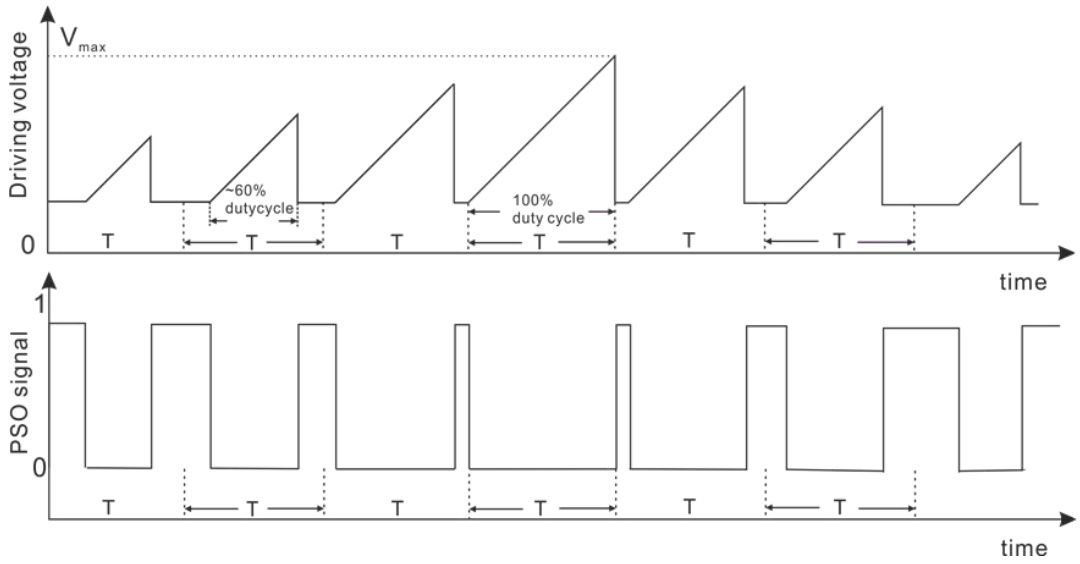

Figure 2.21 – Controller analogue drive voltage and digital PSO signal

The sawtooth voltage profile gradually shifts the interference pattern, typically over the writing period of one grating. Because the amplifier has a limited maximal voltage, each period the integrator is reset using the PSO signal. The interference pattern is therefore in the same position as the start of the previous period. By keeping the PSO on, the maximal driving voltage reached by the integrator circuit is reduced, therefore reducing the maximal amplitude of the refractive index modulation. The "firing positions" where the PSO signal are applied are calculated in software prior to the writing.

For the grating generation, the spot size bears important consequence on the depth of the grating's refractive index modulation. The focused spot for the system contains approximately 10 interference fringes, whose relative positions are defined by the phase control of the system. The small area of exposure and number of fringes greatly benefits the grating modulation contrast and the complexity of the grating apodisation profiles that can be achieved. The scheme has enabled ultra-wide detuning of gratings [84] and complex grating profiles to form Hilbert transformers [85].

The simultaneous generation of gratings and waveguide through the EOM phase control scheme permits the sample translation to be kept at a constant velocity throughout the waveguide writing process. The fabrication process is accelerated with respect to intensity modulation techniques, where the fluence must be

matched during waveguide writing and grating writing, i.e. writing speeds adapted as a function of beam intensity modulation. The waveguide losses through phase control are reduced as the waveguide refractive profile does not suffer from discontinuities causing scattering or unwanted reflections within the waveguide structure. Improved grating contrast has been achieved as more power is available through the scheme. The faster fabrication time improves device quality through reduction of hydrogen outgassing.

2.5.4 DUW platform capability for integrated gratings

Direct UV writing can be controlled to simultaneously define waveguides and gratings in germanosilicate silicate. Type I gratings are formed through this fabrication procedure in a similar process as for the waveguide definition described in section 2.4. Photo-induced gratings can be directly assimilated into waveguide structures to offer different functionality to enrich the functionality of DUW waveguides, without causing excess propagation loss [86].

The description of the grating refractive index profile produced can be obtained through couple-mode theory, and the reader is referred to the literature for ample treatment on the subject [67], [87]. The refractive index profile along the grating in the direction of travel of propagation, $\delta n_{eff}(x)$, is given by equation (2.23).

$$\delta n_{eff}(x) = \overline{\delta n_{eff}} \left\{ 1 + \nu(x) \cos \left[\frac{2\pi}{\Lambda_G} x + \phi(x) \right] \right\} \qquad \textbf{(2.23)}$$

In equation (2.23), $\overline{\delta n_{eff}}$ is the average refractive index perturbation over one grating period, $\upsilon(x)$ is the fringe visibility, Λ_G is the grating period, and $\phi(x)$ is the grating chirp. The fringe visibility is defined by the apodisation function of the grating, which can be understood as an envelope setting the depth of the refractive index modulation. The chirp is a measure for the change in the grating period over length of the grating. Figure 2.22 illustrates the refractive index modulation profile scheme. Δn_w is the photo-induced refractive index modulation (section 2.4.3). The description of the refractive index modulation can be readily applied to the tilted grating geometry, and this description of the grating will be the basis of work in Chapters 3 and 4.

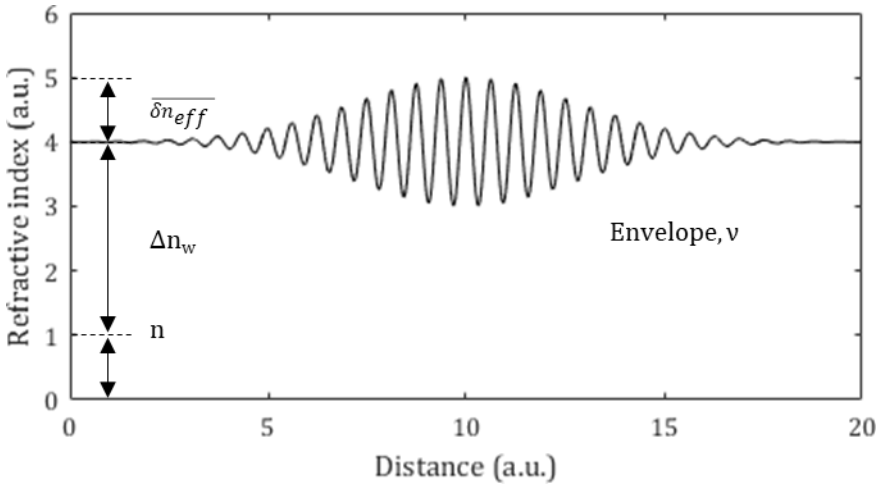

Figure 2.22 – Refractive index modulation for photo-induced gratings.

This section has outlined design principles for both Bragg gratings and tilted gratings. The combination of small-spot DUW and EOM modulation techniques permit the fabrication of complex grating profiles. The EOM modulation scheme has allowed detuning of over 200 nm from the central wavelength of the interferometric fabrication system and grating refractive index contrast of 1×10^{-3} [84]. The constraints on the detuning range of the central grating period ultimately limit the fabrication to tilted gratings with small angles of tilt. Further work will be discussed in later chapters to fabricate gratings with large tilt angle.

The control of the grating length and apodisation profiles permits the tailoring of the reflectivity conditions. Gaussian apodisation permits sideband suppression, which is beneficial for experiments sensitive to noise. The design of the grating strength has permitted simultaneous integration of gratings for characterisation and reflectors permitting the improvement of the efficiency of single-photon detectors for QIP applications [31]. The following section will outline the use of the gratings as diagnostic tools for measuring both grating and waveguide properties.

2.6 Grating-based device characterisation

The spectral characterisation of individual components is essential to validate device functionality and for integration into larger optical networks. This section introduces practical considerations for the characterisation setups used for the testing of the devices fabricated in this study. The methods of characterisation and

data processing vary as a function of the nature of the fabricated grating, and specific considerations will be discussed in the relevant chapters.

2.6.1 General considerations for experimental setups

The characterisation setup uses fibre-based telecommunications equipment. Broadband light sources are used to interrogate waveguide and grating responses across the telecoms C-band (1530-1570 nm). This permits simultaneous interrogation of Bragg gratings with narrow bandwidth, or investigations of the spectral response of broadband tilted gratings.

Light is transported to and from samples using single mode telecoms fibre. It is coupled on and off chips through fibres mounted in v-groove arrays that are directly butt-coupled to the waveguides. The launch can be adjusted with the help of a helium-neon laser source with a visible radiation at 633 nm. Optimisation of the launch is done using a telecoms source and a combination of alignment cards and cameras sensitive to IR radiation. The signal is either coupled back to the launch fibre, or transmitted to a collection fibre, which are connected to an optical spectrum analyser (OSA). The OSA acquires the spectral response of the grating, and further data processing is carried out on a PC.

Polarisation control is essential to enable the study of waveguide properties for different degrees of polarisation. Fibre polarisers, fibre polarisation beam splitters and polarisation maintaining (PM) fibres are used to control the polarisation state of the system. In Figure 2.23, a fibre polariser is used to control the polarisation state

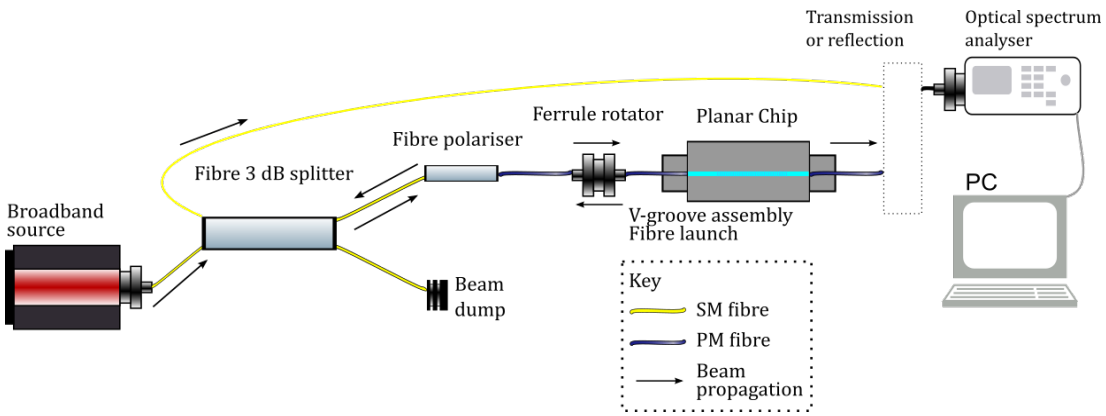

Figure 2.23 – Waveguide and grating characterisation setup.

of the launch signal. Ferrule connectors that align the orientation of PM fibres or rotate one by 90° are used to select the polarisation mode that is launched into the waveguide.

2.6.2 In-situ characterisation of waveguide properties

The characterisation of Bragg gratings has been used to infer important properties of the waveguide itself. Reflection measurements of multiple Bragg gratings fabricated in waveguides permits in-situ characterisation of waveguide losses in a non-invasive manner [86]. Polarisation-dependent transmission loss can be inferred through the control of the polarisation state. SoS DUW waveguides and gratings have been reported with loss values of 0.226±0.026 dB/cm and 0.239±0.026 dB/cm for TE and TM polarisation states, respectively.

The techniques can be readily extended for spectral interrogation of Bragg gratings with central wavelength near 800 nm, with the appropriate source and fibre components. The grating spectral interrogation across a wide range of wavelengths can also provide information on the dispersion characteristics of waveguides to characterise the material properties for non-linear optics applications used in heralded single-photon sources [88]. Further investigation to measure the waveguide birefringence through grating interrogation will be discussed in later chapters.

2.7 Chip and end facet preparation

The chips used in this study have been produced through physical machining tools available in the ORC. This section provides an overview of precision dicing and polishing techniques used to process wafers and chip. The reader is referred to [89] for a comprehensive review of the development of machining techniques for this SoS platform. As an introduction, relevant figures of merit to assess the quality of the end facet preparation are presented.

2.7.1 Surface roughness characterisation

The surface roughness of a sample can be understood qualitatively as the typical height deviation from the mean height values of its profile. It is defined in terms of the average surface roughness, R_a, and the root-mean squared surface roughness,

R_q. R_a and R_q are given by equations (2.24) and (2.25) [90], where z_i and $\bar{z}$ are the measured height and mean height values, respectively, and N is the number of sample points.

$$R_a = \frac{1}{N}\sum_{i=1}^{N}|z_i - \bar{z}| \tag{2.24}$$

$$R_q = \sqrt{\frac{1}{N}\sum_{i=1}^{N}(z_i - \bar{z})^2} \tag{2.25}$$

R_a and R_q are numerically close for surfaces without large deviations; surfaces with holes or bumps will be characterised by R_q larger than R_a. Equations (2.24) and (2.25) characterise a surface in terms of its height along a single spatial coordinate, i.e. a two-dimensional surface represented by a line function of the type $z = f(x)$. Surface scanning techniques typically use data defined in three dimensions, i.e. surface profiles of the type $z = f(x,y)$. The corresponding parameters are S_a and S_q, are the "areal" surface roughness values for a three-dimensional surface; these are defined by ISO 25178-2 [91]. S_a and S_q will be stated when reporting measurements from the surface scanning tools used in this study.

White light interferometry has been used throughout this study as a means of measuring the surface roughness parameters of the end facets of the chips prepared. It is an optical non-contact surface profiling technique that permits the profiling of surface roughness. The system employed (ZeMetrics™ ZeScope™) can perform rapid scans (typically 1 minute) over surface areas of 70×70 μm^2. The system has been shown to be suitable for surface roughness characterisation purposes through extensive comparative studies with other profiling techniques (atomic force microscopy, profilometry), as described in [89].

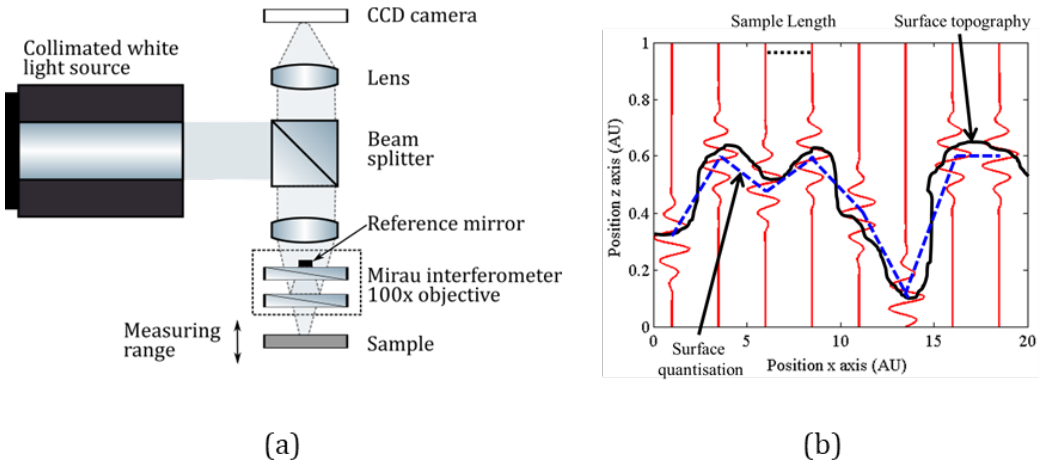

Figure 2.24 – (a) White light interferometer imaging system. (b) Measurement system principles of operation, reprinted from [89].

A schematic of the imaging apparatus and its principle of operation are shown in Figure 2.24 (a) and (b), respectively. The sample is placed on a stage with a range of movement of 200 mm in both x and y axes, and 160 mm in the z-axis. A collimated white light source is used to illuminate the sample. The sample is imaged using a 100x microscope objective set up with a Mirau interferometer. The sample is scanned vertically and a CCD camera is used to record the pixel intensity. Interference fringes are created at the sample surface. The system's control software fits an envelope function to each instance of the interference, which permits a vertical map to be constructed. The system's illumination's short coherence length (~8 µm) permits smaller vertical movements of the sample and fewer fringes in the interference comb to fit. The equipment's quoted vertical RMS resolution is 0.1 nm, with a repeatability of 0.01 nm. The image is then processed in an image analysis software (Image Metrology SPIP™). Surface levelling was applied to the image before calculating the surface roughness parameters, following the equipment manufacturer's recommendations. Multiple scans are repeated across the length and width of the end facet considered.

2.7.2 End facet preparation methods

High quality end facets are desirable at the input and output of waveguides for many applications. Processes are required to achieve end facets that are vertical, with low surface roughness and free from chipping. Appropriate surface roughness

parameters are necessary to minimise scattering losses and optimise waveguide termination. The production of angled facets for the reduction of Fresnel reflections when coupling on and off chips is useful for compatibility with many different systems, such as high power free space laser systems required for non-linear applications (Chapter 5). Good termination of waveguides is particularly important when considering Bragg gratings, where the reflected spectrum is most often used as a characterisation tool. Precision dicing, lapping and chemical-mechanical polishing techniques have been used throughout this study and are discussed in more detail in this section.

2.7.2.1 Precision dicing

Precision dicing has been employed to obtain chips from wafers fabricated through FHD. It offers the flexibility in terms of chip dimensions that can be made; typical test chip dimensions are 20 mm in length and 10 mm in width. The high precision dicing machine used in this study (Loadpoint MicroAce Series 3, shown in Figure 2.25) permits the machining of straight geometries of structures in two-dimensions. Samples are placed on a high-precision sample bed with two-dimensional movement control. The sample can be rotated, permitting the dicing of horizontally angled end facets.

The quality of the dicing can be adapted to suit launch requirements. Where index-matching adhesives can be used for waveguide-to-waveguide or fibre-to-waveguide schemes, the optical finish of the dicing is relaxed, with typical S_a of 15-30 nm. The

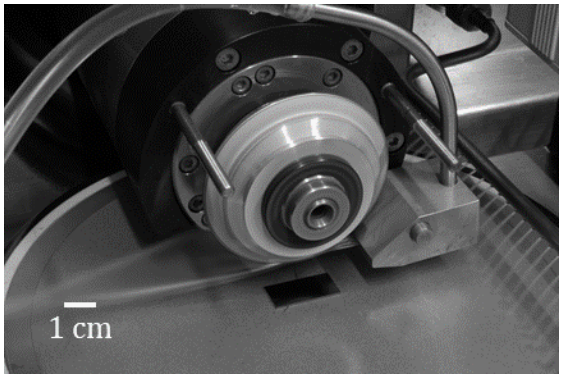

Figure 2.25 – Detail of the precision dicing setup for the physical machining of SoS wafers and chips. Image provided by L. Carpenter.

equipment can be used to provide high-quality end facets through ductile dicing with S_a of 5 nm [92].

2.7.2.2 Lapping and chemical mechanical polishing

Lapping and chemical mechanical polishing (CMP) techniques are traditionally employed where end facets with very low surface roughness are required. The planarisation of samples is achieved through a succession of mechanical lapping and CMP actions with abrasives. Lapping/polishing apparatus consists of a polishing head and a polishing plate. The sample is held in a chuck mounted onto the polishing head. The polishing head is pushed onto the polishing pad, and both the head and plate are rotated. The lapping through mechanical action is used to remove material and ensure sample flatness; the process usually utilises cast iron lapping pads and silicone carbide or aluminium abrasives. Typical surface roughness values by lapping are better than R_a of 400 nm. The CMP action combines mechanical and chemical reactions for a high-quality finish. CMP uses a polyurethane pad with a chemical slurry (typically with colloidal silica) that acts as a wet etchant and removes high points from the surface. CMP is typically be used to achieve S_a of 3-10 nm; optimised processes can yield S_a as low as 0.2 nm [93].

An alternative setup was developed by the author during this study, which has been adopted as the standard process for lapping and CMP for SoS. The equipment (Allied High Tech Products Inc. Multiprep™, shown in Figure 2.26) uses disposable lapping

Figure 2.26 – Allied High Tech Products Inc Multiprep™ lapping and chemical-mechanical polishing equipment.

abrasive sheets placed on a preconditioned polishing pad for lapping. Successive lapping steps are completed to ensure the removal of material and flattening of the sample. The CMP step is conducted with a slurry comprised of colloidal silica using a second pad with a polyurethane surface. The polished chips have been measured with surface roughness better than $S_a = 5\ nm$ through characterisation by white light interferometry. The process has considerably sped up the processing time to about 1 hour, compared to a few hours using traditional polishing tools. Custom jigs have been developed to permit the preparation of flat and vertically angled-polish end facets. This process has been extended for the planarisation of borosilicate glasses for endcaps, and will be discussed further in Chapter 5.

2.7.3 End facet processing overview

The section above has presented two physical machining processes techniques that permit the preparation of high quality end facets with surface roughness better than S_a = 5 nm. A lapping and chemical mechanical polishing (CMP) process was developed by the author, which has been adopted within this research group for the vertical polishing of SoS chips. Both precision dicing and lapping/polishing techniques permit the fabrication of angled end facets to reduce Fresnel reflections. These are attractive for the integration into optical networks, either through free-space, fibre-to-waveguide or waveguide-to-waveguide coupling. An overview of the end facet type that can be achieved through these machining methods is summarised in Figure 2.27.

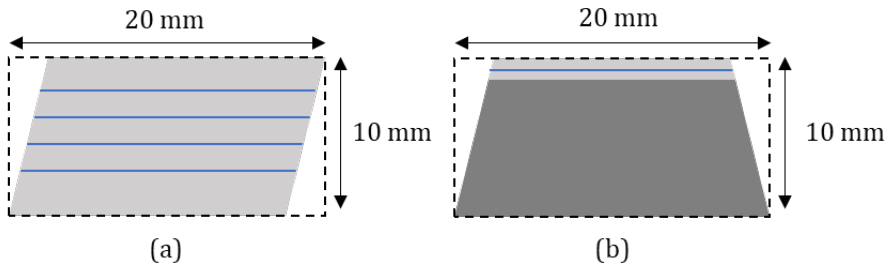

Figure 2.27 – End facet profiles through physical micromachining (a) 8° horizontally angled facets produced by precision dicing (top view). (b) 8° vertically angled facets produced by lapping and polishing (side view). Waveguides have been indicated by blue lines. The pre-processed rectangular chips have been indicated by the dashed lines.

2.8 Conclusions and further work

This chapter has reviewed the fabrication tools used in this study for the production of silica-on-silicon photonics integrated circuits. Flame hydrolysis deposition and direct UV writing permit the fabrication of buried waveguide channels and gratings. Fibre-based characterisation methods can be used to probe the fabricated structures and obtain waveguide and grating properties. The platform is also compatible with physical micromachining techniques permitting the integration of individual building blocks into larger networks.

Flame hydrolysis deposition has been shown to be a suitable fabrication technique to produce slab waveguides with properties that can be tailored to control material stress and photosensitivity. This is of particular interest to control the layer and waveguide birefringence. Chapter 5 will report the adaptation of this technique to develop high-birefringence waveguides for applications in quantum information processing experiments. Direct UV laser written waveguides and gratings permit the development of novel functionality on chip. Tilted gratings in particular offer the route for novel waveguide-based filtering and light routing applications [94], but fabrication is currently limited to small angle tilted gratings. The development of large angle tilted gratings for in-line polarisers and polarising beam splitters will be a focus of study in the following chapters.

Chapter 3 Tilted gratings for integrated polarising devices

Polarisation sensitive devices with the ability to route light are an important component of the integrated photonics component catalogue. The ability to filter polarised light is of interest in systems where the fidelity of the polarisation state is crucial, such as: coherent communications, quantum information processing and high-performance sensing. Chapter 2 presented how direct-UV written (DUW) waveguides in photosensitive silica-on-silicon (SoS) technology offer a low-loss route for further integration of optical functionality on chip.

This chapter presents work on the novel implementation of integrated polarisers in SoS based on 45° tilted gratings. The chapter covers design, modelling, fabrication and characterisation of these devices that have the potential to be used as building blocks in more complex systems. The discussion is supported by further engineering developments for the optimisation of device performance.

3.1 Photonics integrated circuits for polarisation control

There are various integrated approaches to polarise light. These include: coupler schemes to separate polarisation [95], using metallic layers and plasmonic coupling to induce preferential loss [96], or active electrical polarisation control [97]. Each scheme has different merits and disadvantages i.e. increased device complexity, stringent fabrication tolerances or challenging integration into larger optical networks. These factors can be detrimental to device performance in terms of insertion loss and operational spectral bandwidth.

UV-induced tilted gratings (section 2.5.1) can be used for polarisation control and beam routing; these structures have been well studied in silica-based fibre platforms, both theoretically and experimentally [98]–[100]. 45° tilted gratings have been UV-induced into fibres and used to demonstrate in-line fibre polarisers with polarisation extinction ratios in excess of 40 dB, which is comparable to bulk optics components; in addition, the in-line fibre architecture benefits from low insertion loss into a fibre network [101]. The implementation in a planar waveguide is advantageous as it can be readily integrated with other functions and elements of a photonics network. The following section outlines design considerations for the implementation in SoS technology.

3.2 Design of polarisers with 45° tilted gratings

Chapter 2 described the ray propagation mechanisms between materials with refractive indices n_1 and n_2. Snell's law was used to predict the angles of reflection and refraction of the reflected and transmitted rays (section 2.2.1). The reflection at this interface is in fact polarisation dependent and the amplitudes of these reflected and transmitted waves are described by Fresnel's reflection coefficients for TE and TM waves, which can be found in the literature [102]. Based on the aforementioned account, when the Fresnel reflection coefficient for the TE mode is equal to 0, the reflection angle is named the Brewster angle, θ_B, which is given in equation (3.1). No such angle exists for the TM mode. A consequence of the Brewster angle is that the reflection of an unpolarised beam incident on an interface with different refractive indices will be polarised.

$$tan\ \theta_B = \frac{n_2}{n_1} \qquad \textbf{(3.1)}$$

A waveguide with a modulation of its refractive index (a grating) can be considered as such an interface. For small ($<10^{-2}$) differences in the refractive indices, a beam incident on a grating plane incurs negligible refraction in its direction of propagation and small Fresnel reflections for both the TE and TM polarisations. DUW gratings in SoS have a characteristically low refractive index modulation, of the order of 10^{-3} (section 2.5). The highest reflectance difference between TE and TM polarisations occurs at the Brewster angle, given by $\tan \theta_B \sim 1$, which corresponds to a grating tilt

angle of $\theta = 45^0$. The fact is verified numerically [103] and analytically [104], and in agreement with experimental reports in the literature. DUW SoS waveguides with gratings of length of a few to tens of millimetres should have comparable performance to demonstrations of 45° tilted-grating based polarisers in photosensitive silica fibre [100].

The strongest light coupling between a waveguide mode and a grating-induced reflection mode takes place when the phase-matching conditions are met. The wave vectors of the reflected mode ($\overline{K_R}$), core mode ($\overline{K_{Co}}$) and the grating ($\overline{K_G}$) are schematically represented in Figure 3.1 (b) and related by equation (3.2)

$$\overline{K_R} = \overline{K_{Co}} + \overline{K_G} \qquad \textbf{(3.2)}$$

When the grating is tilted at an angle, θ, the amplitudes of the wave vectors are related by equation (3.3).

$$K_{Co} = K_R = \frac{K_G}{2\ cos\ \theta} \qquad \textbf{(3.3)}$$

The magnitudes of the incoming and radiated wave-vectors are equal and given as $|\overline{K_R}| = |\overline{K_{Co}}| = {}^{2\pi n}/_{\lambda}$. Given that the magnitude of the grating wave-vector is $|\overline{K_G}| = {}^{2\pi}/_{\Lambda_G}$, the grating period has been calculated as $\mathbf{\Lambda_G = 756.9\ nm}$ for a tilt θ= 45° operating at λ = 1550 nm. At this tilt angle, based on the k-vector argument, the TM component should be ejected at 90° to the waveguide by the angled tilted gratings planes, as shown in Figure 3.1 (a). This grating period corresponds to a Bragg contra-directional reflector with central wavelength of 2.19 μm (section 2.5.2).

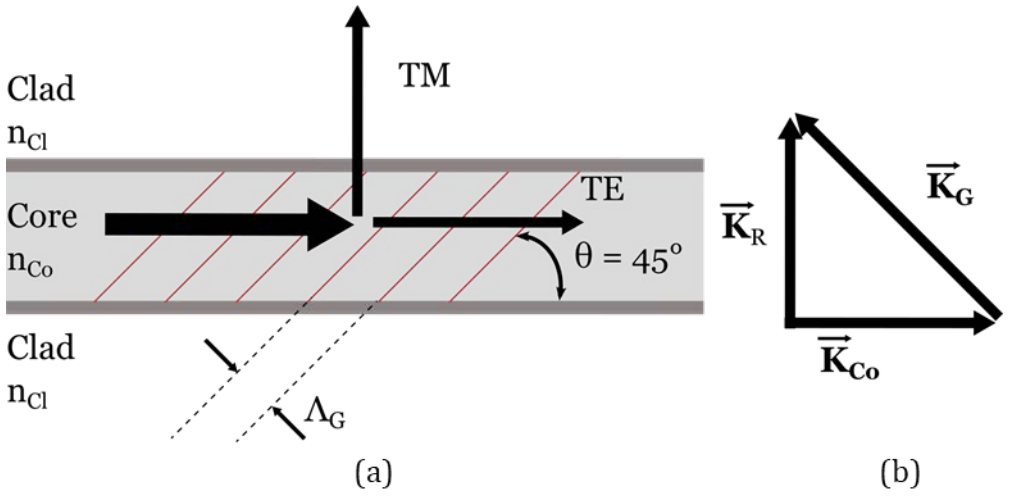

Figure 3.1 – (a) K-vector description of the grating operation. θ is the tilt angle of the grating. (b) Schematic top view of device.

Under these constraints, the waveguide mode is coupled into a radiation mode propagating through the core planar layer. These considerations have permitted the design of a grating structure operating as a polariser in low-refractive index contrast waveguides. The physical properties and spectral responses of these structures are of interest to understand the architecture's operation, and this is discussed next as applicable to DUW waveguides and gratings.

3.3 Modelling of 45º tilted gratings

The following section presents a theoretical study of 45º tilted gratings in SoS DUW waveguides conducted as part of collaborative work with Dr. Nina Podoliak and Dr. Peter Horak from the University of Southampton's Optoelectronics Research Centre (ORC). The contributions are detailed throughout this section and summarised in Appendix B. As a preamble, relevant background on the modelling of these structures is given.

3.3.1 Background

To date, most theoretical and experimental work has been done for tilted gratings in fibres. Erdogan and Sipe carried out detailed theoretical treatment and experimental verification describing the tilting effect on field properties for small tilt angles (<15º) [69]. The work was extended to explore the effects of gratings with large tilt angles [103]; in addition theoretical studies have shown that gratings with

45° tilt achieve the greatest polarisation selectivity in these low-index contrast platforms. However, the methods resort to involved numerical simulations and do not provide full insight into spectral response of tilted gratings.

A report by Yoshino has addressed these limitations with a beam tracing (BT) approach; the reader is referred to [104] for a comprehensive discussion. Yoshino has derived a set of analytical expressions to describe the polarisation extinction ratio (PER) of 45° tilted gratings in waveguiding geometries. The results of the BT model match those of more involved numerical results, which have also been used in conjunction with experimental demonstrations of 45° tilted gratings in fibre [100]. The PER, Γ, is given by equation (3.4) under the appropriate phase-matching conditions.

$$\Gamma = -b\ \Delta n_g^2\ L_g \qquad \textbf{(3.4)}$$

From equation (3.4) it is evident that Γ is linear with respect to grating length, L_g, and quadratic with respect to the refractive index contrast, Δn_g, both of which are parameters that can be controlled in DUW. Γ is a function of an additional parameter, b, which is determined by the interaction of the field with the grating structure. This parameter is described in the following section.

3.3.2 Theoretical description of 45° tilted gratings

The following section describes the development of a theoretical model to extend the BT approach for the SoS DUW geometry. The numerical modelling implementation and analytical derivations of the structures presented in sections 3.3.2.2 and 3.3.2.3 have been conducted by Dr. N. Podoliak.

3.3.2.1 Waveguide and grating theoretical description

The model is based on a planar architecture where a waveguide has been defined in a photo-sensitive core layer by a focused laser spot with a Gaussian profile (Section 2.4.3). The core layer has a refractive index, n_{Co}, greater than the upper and lower clads. The geometry permits vertical confinement of the radiation mode. The refractive index profile of the planar waveguide, n_w, is defined in a 2-dimensional (x, y) plane. The waveguide refractive index profile is given by equation (3.5).

$$n_w(x,y) = n_{Co} + \Delta n_\omega \; exp\left(-\frac{y^2}{\sigma^2}\right) \quad \textbf{(3.5)}$$

In equation (3.5), Δn_ω is the photo-induced refractive index shift with respect to the photosensitive core layer and σ is the radius of the waveguide defined. The waveguide has a fixed refractive index in the x-direction of propagation and a Gaussian-profile in the y-direction as a consequence of the DUW fabrication process. Gratings have been induced through a photosensitive process, yielding a grating refractive index profile n_g with a sinusoidal variation given by equation (3.6).

$$n_g(x,y) = n_{Co} + \left[\Delta n_\omega + \Delta n_G \; sin\left(2\pi\frac{x-y}{\Lambda_G}\right)\right] exp\left(-\frac{y^2}{\sigma^2}\right) \quad \textbf{(3.6)}$$

In equation (3.6), Δn_g is the peak-to-peak index modulation of the sinusoidal grating and Λ_G is the grating period. The final exponential term of equation (3.6) is a consequence of the definition of the waveguide field profile through the DUW fabrication process.

3.3.2.2 Finite-element modelling of tilted gratings

The devices have been modelled in COMSOL Multiphysics ® using finite element modelling (FEM). FEM allows for accurate modelling of structures with sub-wavelength grating periods (here Λ_G = 756.9 nm) by defining a mesh where computations will occur. The low refractive index contrast of DUW waveguides has been found to necessitate long interaction lengths to study higher efficiency grating-based field effects. The computational requirements for modelling gratings of the order of millimetres in length are beyond what is readily achievable using numerical software packages. The preliminary numerical simulations have been implemented using tilted gratings with short lengths (<200 μm) to understand the physical mechanisms governing these structures.

The electric field response of a waveguide with a 45° tilted grating has been investigated with waveguide parameters $\Delta n_g = 2\times10^{-3}$ and L_g = 100 μm. A single-out of plane (TM) polarised electric field is launched into the waveguide at the leftmost port under two excitation conditions. First, a reference (control) waveguide without a grating, and second a test structure with a waveguide containing a 45°-tilted

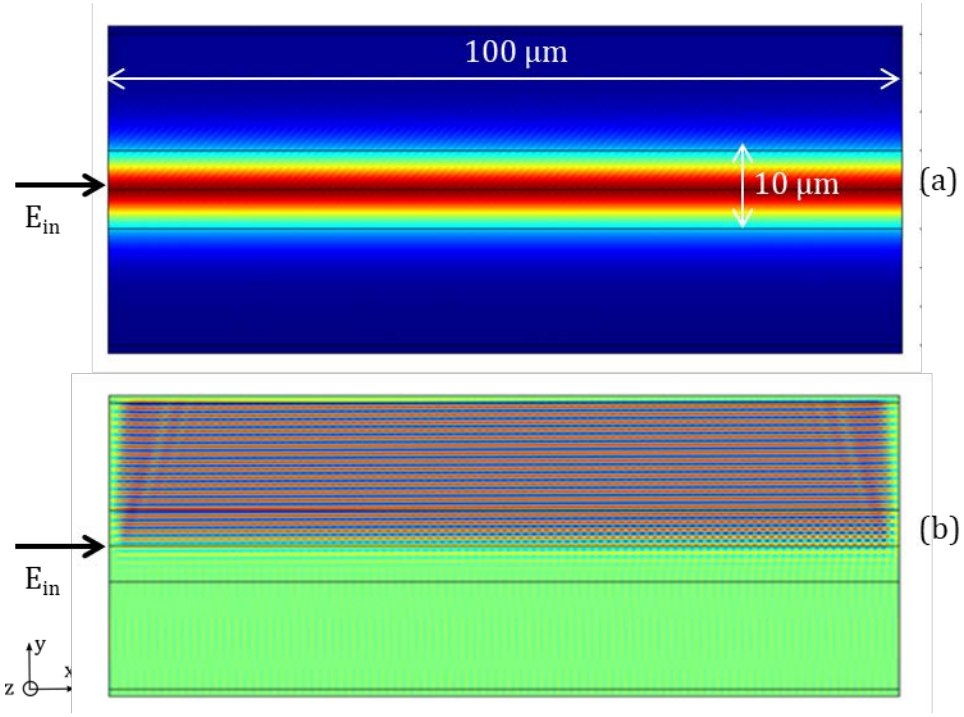

Figure 3.2 – Out of plane polarised electric field simulations of in-line waveguide polariser based on tilted gratings. The input electric field is denoted E_{in}. (a) Out of plane electric field waveguide mode interacting with 45° tilted gratings. (b) Electric field coupled into radiation modes through reflection off tilted gratings. The waveguide boundaries have been outlined for clarity. Simulation figures provided by Dr. N. Podoliak. Dimensions are marked on sub-figure (a) and are identical for all sub-figures. Electric field units are arbitrary.

grating – see Figure 3.2 (a). The reflected field strength is ~2% of the input field. Figure 3.2 (b) presents the electric field profile that has been obtained by subtracting the reference field (i) from the test field (ii). This represents the electric field radiated from the waveguide from the interaction of the waveguide mode with the tilted grating.

The simulation results have highlighted some key features of the device's operation. Firstly, the reflected field remains a highly-polarised quasi-plane wave propagating through the core layer. Fringes in the radiated electric field with a period of the grating have been observed. The formation of this quasi-planar wave front is thought to be caused by the interference between the forward propagating waveguide mode and the radiated waveguide modes. The termination profile of the grating has caused a reflection, leading to ripples in the electric field. The effect has

been reduced with smaller refractive index contrast; as such, with correct experimental fabrication the effect may not be as apparent for SoS DUW devices. Apodisation of the grating should help minimise this effect further; the study of advanced grating engineering for field manipulation is left as an investigation route for future work.

Another feature that has been identified is the presence of a standing wave below the grating. According to the k-vector model presented in section 3.2, downward coupling is not permitted in this architecture's configuration. This effect was found to be caused by reflection from the output port, which has been verified by changing the simulation boundary conditions of the output port to be scattering. The simulation results have highlighted the need for adequate care for experimental characterisation as scattering and back-reflections at end facets are likely to affect the characterisation of these grating-based devices.

The following section presents further investigation into the effect of grating length and refractive index modulation on the device's performance.

3.3.2.3 Analytical description of grating response

The field response of the device has been simulated for ten values of the refractive index contrast (Δn_g = 0.5-5×10^{-3}) and at five gratings lengths (L_g = 10-200 μm). The field radiated by the grating constitutes a form of loss, different from other waveguide losses (scattering, absorption). Under the constraints of 45° tilted gratings with low refractive index contrast, the grating-induced Fresnel reflection loss of the TE mode are negligible. The PER of a grating is usually described as the transmittance ratio of TE against TM modes. The radiation loss per unit length is approximated to the PER of the device in this study. Figure 3.3 (a) and (b) show results of the simulated radiation loss for different grating lengths and refractive index modulation, respectively.

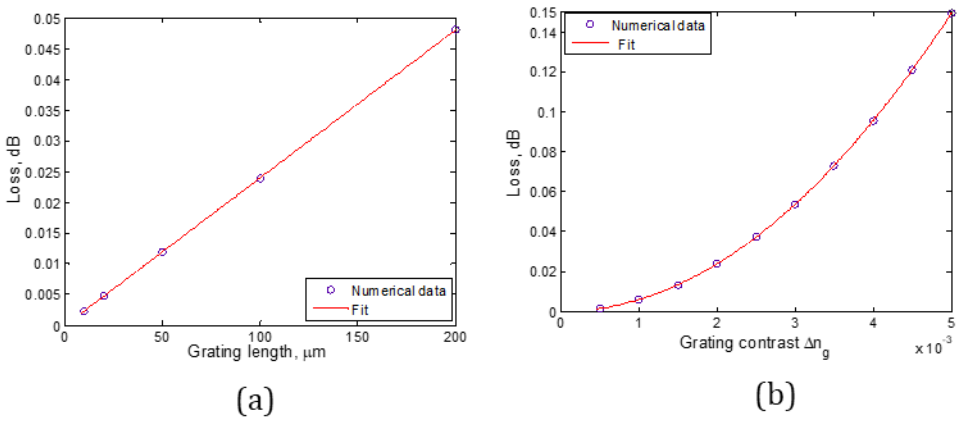

Figure 3.3 – Simulated grating reflection loss and fit of the 45⁰ tilted gratings with respect to (a) length at $\Delta n_g = 2\times10^{-3}$ and (b) refractive index contrast at $L_g = 100\ \mu m$. Simulation results provided by Dr. N. Podoliak.

The simulation results have been fitted and used to derive an analytical expression for the grating response. The PER at the grating resonant wavelength, Γ_0, is given by equation (3.7).

$$\Gamma_0(dB) = 4.34\,\pi^2\sqrt{2\pi}\,\frac{\Delta n_g^2}{\lambda_R^2}\,\frac{\omega_0^2\sigma^2}{\omega_0^2+\sigma^2}\,L_g \qquad \textbf{(3.7)}$$

Equation (3.7) has been defined in terms of the input field parameters and waveguide fabrication parameters: σ is the waveguide radius, ω_0 is the mode field radius and λ_R is the grating resonant wavelength. The grating PER is proportional to the grating length, L_g, and has a quadratic dependence on the grating contrast, Δn_g, which agrees with reports in the literature.

The grating's PER wavelength response was modelled for ten wavelengths from 1500-1590 nm for waveguides with tilted gratings of length 20 mm. The numerical results have been fitted – see Figure 3.4 –and the wavelength-dependent PER is given by equation (3.8).

$$\Gamma(\lambda) = \Gamma_0\ exp\left\{-\frac{2\pi^2\,\sigma^2\,\omega_m}{\omega_m^2+\sigma^2}\left(\frac{n_m}{\lambda}-\frac{1}{\Lambda_G}\right)^2\right\} \qquad \textbf{(3.8)}$$

In equation (3.8), ω_m is the waveguide mode field diameter and Λ_G is the grating period for the central design wavelength. The shift of the central wavelength has

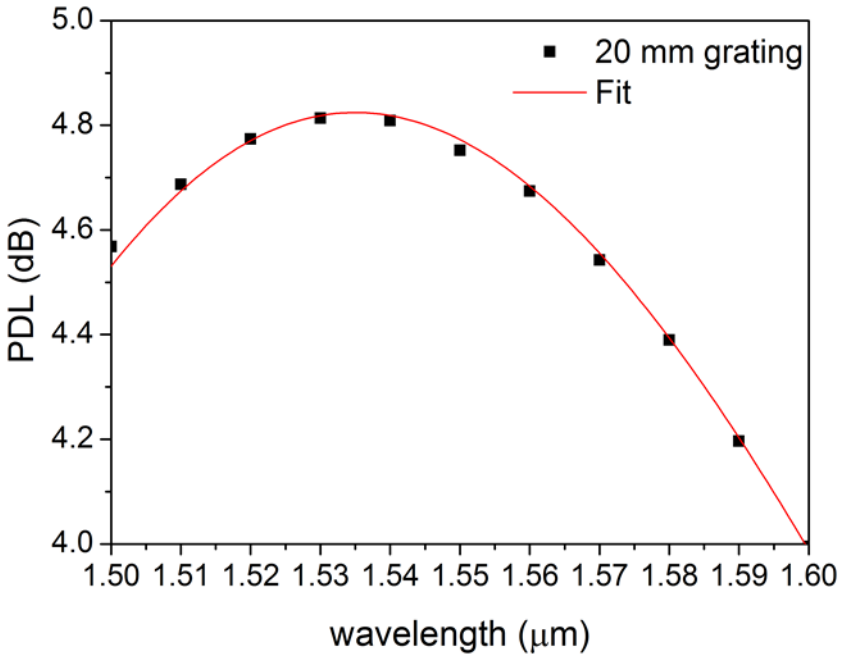

Figure 3.4 – Simulated grating polarisation dependent loss and analytical fit for waveguides with 20 mm tilted gratings.

been caused by the refractive index used for numerical simulations. The wavelength dependent loss is lower than 0.3 dB over the C-band (1530-1570 nm) and less than 0.8 dB over the entire range of wavelengths simulated (1500-1590 nm).

3.3.3 Figures of merit

The expressions from this theoretical study have been compared to the PER results presented by Yoshino in [104]. A direct comparison has been made through investigation of the '*b*' parameter of equation (3.4) with $\Delta n = 1\times10^{-3}$ and $L_g = 10$ mm. The parameter has been calculated from the simulations presented in Section 3.3.2.3 as $b = 60$ μm^{-1} for equation (3.4), compared to $b = 223$ μm^{-1} in [104]. The discrepancy has occurred as the grating contrast in [104] is assumed constant and overlaps the waveguide mode area completely. DUW gratings have a Gaussian profile and may be narrower than the transmitted mode. By accounting for this and following the calculations in [104], this parameter was calculated as $b = 59.1$ μm^{-1}, which is in better agreement with the FEM simulations that have been described herein. The following section presents details of experimental work on the development of integrated SoS tilted grating-based polarisers.

3.4 Fabrication of integrated polarisers by DUW

Chapter 2 has described the DUW platform's ability to fabricate Bragg reflectors and small angle titled gratings. This section presents the technical steps for the fabrication of in-line waveguide polarisers using 45^0 tilted gratings. The wafer employed in this study was fabricated at the ORC by flame hydrolysis deposition (FHD) (Section 2.3). The wafer has a 16.5 μm thermal oxide underclad with a FHD 5.1 μm core and 18.1 μm cladding layer. The refractive index of the core and cladding layers has been measured by a prism coupling measurement technique (Section 2.3.4) and the relative index contrast between the layers has been calculated as 0.66%. The waveguides may exhibit multi-mode behaviour due to a relatively high refractive index contrast. Full details of this wafer (NB12/18) are presented in Appendix C.

3.4.1 DUW interferometer board design and fabrication

The fabrication of gratings with a 45° tilt has required the development of a new dual-beam interferometer board. A schematic of the interferometer layout is shown in Figure 3.5 (a). The whole system has been fixed to an optical breadboard compatible for mounting to the DUW system. The mirrors, beam splitter, electro-optic modulator (EOM) and holders are identical to those on the interferometer boards described previously (Section 2.5). The half-angle of intersection, γ, between the two beams required to obtain the desired interference pattern was given by equation (2.20), which is reprinted for ease of reading.

$$sin\ \gamma = \frac{\lambda_{UV}}{2\,\Lambda_G} \qquad \textbf{(2.20)}$$

Using equation (2.20), γ = 9.27° for a UV laser wavelength of 244 nm and a grating period of Λ_G = 756.9 nm. The lens mount system has been modified with respect to other interferometer boards previously designed at the ORC. The components are highlighted in Figure 3.5 (b). Lens mounts are mounted to magnetic kinetic mounts (1) to facilitate the exchange of lens types in this setup. The kinetic mounts have been fixed on to a high precision zoom lens tube housing (2) for adjusting the vertical position of lenses. The zoom lens tube has been inserted into a 2-D translation mount (3) compatible with different drives for precise positioning of

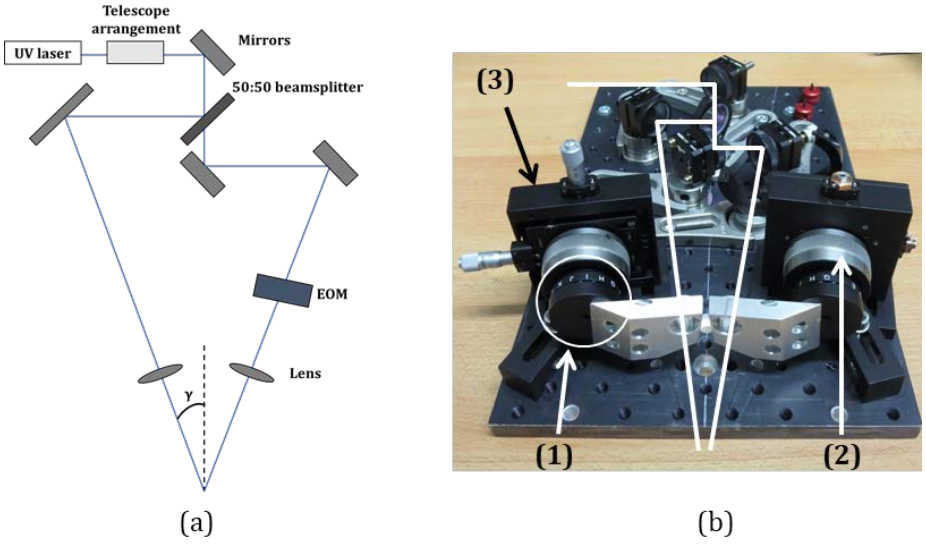

Figure 3.5 – (a) Schematic of the dual-beam interference board utilised for simultaneous waveguide and grating generation by DUW. (b) Interferometer board with magnetic kinetic lens mounts and UV beam path highlighted.

lenses in the laser beam path. The position of the mounts and angle have been marked on the breadboard for accurate positioning of the lenses.

3.4.2 Tilted grating engineering

The following section describes adaptations to the stage control system for the generation of 45° tilted gratings. For DUW, two laser beams have been focussed into the device core layer, which has been illustrated in the inset Figure 3.6. The grey areas in Figure 3.6 (a) and (b) designate a horizontal cross-section of the core planar layer. The black boundaries mark the fixed edge of the chip.

Chips have been placed on a 4-axis air bearing stage and translated under a fixed laser beam spot. The area of overlap of the beams has formed an interference pattern, permitting the simultaneous generation of gratings and waveguides (Section 2.5.3). The grey boundaries indicate the edge of the photo-induced waveguide that are defined during the translation of the chip beneath the focused UV spot.

The standard waveguide and grating generation DUW process has been illustrated in Figure 3.6 (a). The chips have been translated horizontally, resulting in the fabrication of waveguides and Bragg reflectors at a period given by equation (2.20). The chip has been rotated by an angle of 45º during writing for the fabrication of the tilted gratings – see Figure 3.6 (b). The stages have been translated diagonally and at an equal velocity in both the x and y axes of the horizontal plane. The period of the interference pattern is identical, but the gratings have been fabricated at an angle of 45 º relative to the waveguide orientation because the laser spot and interference pattern have not been rotated. The position synchronised output is defined only in the x-axis of translation.

3.4.3 Fabrication of proof-of-concept devices

Twelve waveguides of 20 mm in length have been fabricated on a 10×20 mm chip. Each waveguide has been fabricated with 45º tilted gratings of varying length to measure PER as a function of grating length. The waveguide separation is 500 μm to avoid evanescent waveguide coupling. The test structure layout has been illustrated

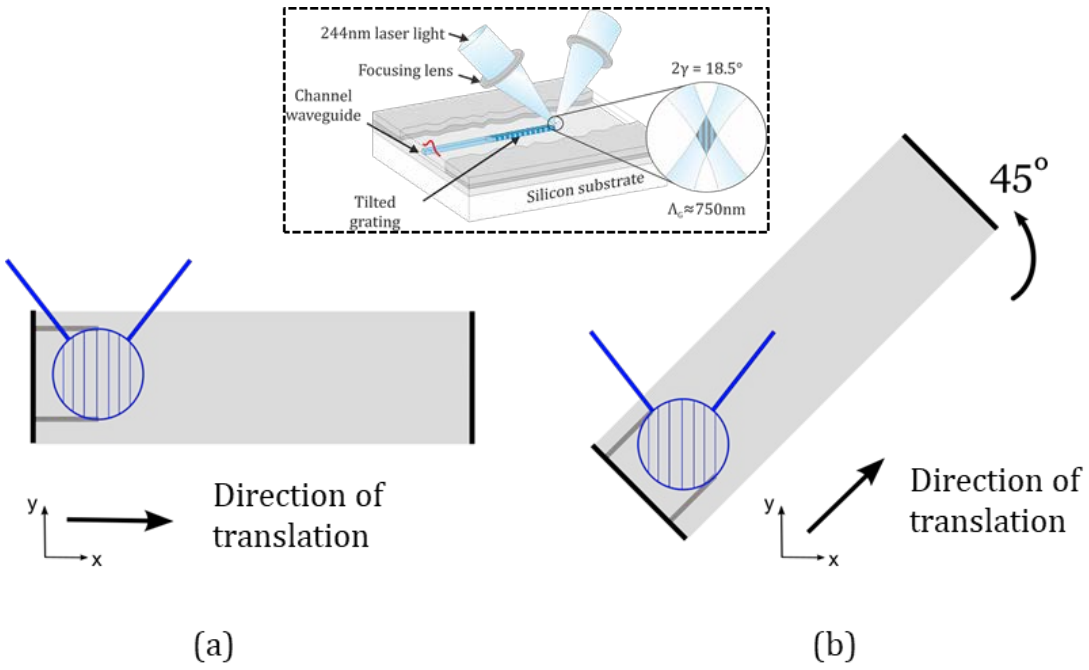

Figure 3.6 – (a) DUW of waveguides and Bragg gratings reflectors in the conventional configuration. (b) Rotation of stage by 45° and change of translation direction for the generation of tilted gratings. Inset: DUW fabrication for waveguides and 45° tilted gratings.

in Figure 3.7 (a). Three identical waveguides with 20 mm gratings have been fabricated to assess reproducibility of our devices and one waveguide with no grating serving as reference. A picture of a fabricated device is shown in Figure 3.7 (b). The presence of the gratings has been verified by looking at the diffraction of the grating under angled white light illumination. A fibre v-groove holder can also be seen to the left of the chip in Figure 3.7 (b). The v-groove block has been used to couple light on and off chip as part of the characterisation process, which is discussed in the next section.

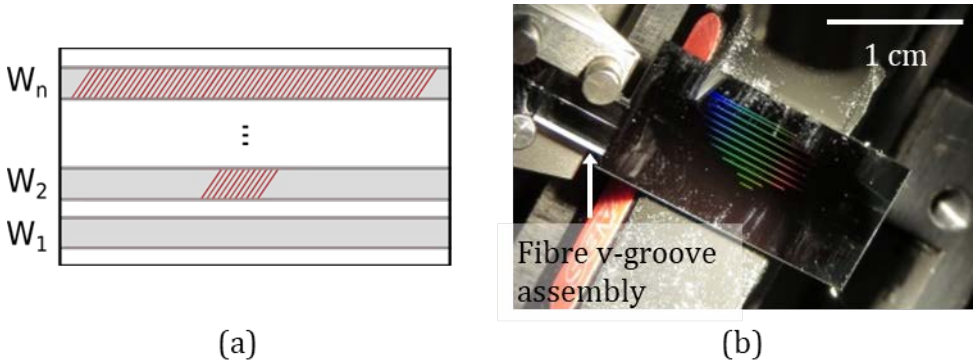

Figure 3.7 – (a) Chip with waveguides containing 45° tilted gratings of increasing length. (b) Picture of 20 mm chip highlighting the gratings.

3.5 Device characterisation

The following section details the characterisation methods used for the investigation of the polarisation extinction ratio of the fabricated waveguides and 45° tilted gratings.

3.5.1 Fibre-based characterisation setup

The device's polarisation dependent response has been characterised in transmission using the setup shown in Figure 3.8. The source used is an erbium-doped fibre amplifier (EDFA) source (IPG Photonics) spanning the C-band (1530-1570 nm). The source has been butt-coupled on chip through a single mode (SM) fibre mounted in a single port v-groove assembly. The source had a characteristically low PER (typical <0.4 dB); the lowest waveguide PER measurement is therefore 0.4 dB. The source will be classed as "unpolarised" in the rest of this discussion. The unpolarised source has permitted a direct self-

referencing measurement of the PER of the gratings in the waveguide. The setup has removed the requirements of narrow-linewidth and highly polarised launch conditions and simplified the alignment tolerance of the launch. The experiment holds providing that the PER of the PM components following the chip are greater than the chip PER; failing this, the experiment is at risk of measuring the PER of the component with the smallest PER in the setup.

The signal has been collected through a 1-meter long polarising maintaining (PM) fibre mounted in a v-groove assembly. Index-matching liquid has been used at the interface between chips and v-groove assemblies to reduce back-reflection and scattering. The collection PM fibre has been connected to a fibre polarising beam splitter (PBS) (Thorlabs PBC1550SM-FC) using a fibre mating sleeves (Thorlabs ADAFC2). The fibre PBS has been used to split the output signal into two orthogonal polarisation modes at two independent ports. Each output fibre of the PBS has been connected to characterisation apparatus, consisting of power metres and an optical spectrum analyser (OSA) for power and spectral interrogation, respectively. All the fibres have been secured to optical benches for added stability. The components listed above have stated PER greater than 20 dB. The measurement of the PER and wavelength-dependency of the grating are presented in the following pages.

3.5.2 Grating-induced polarisation extinction ratio

The chip has been mounted on a translation stage and moved between fixed launch and collection ports. Coupling has been adjusted manually between successive

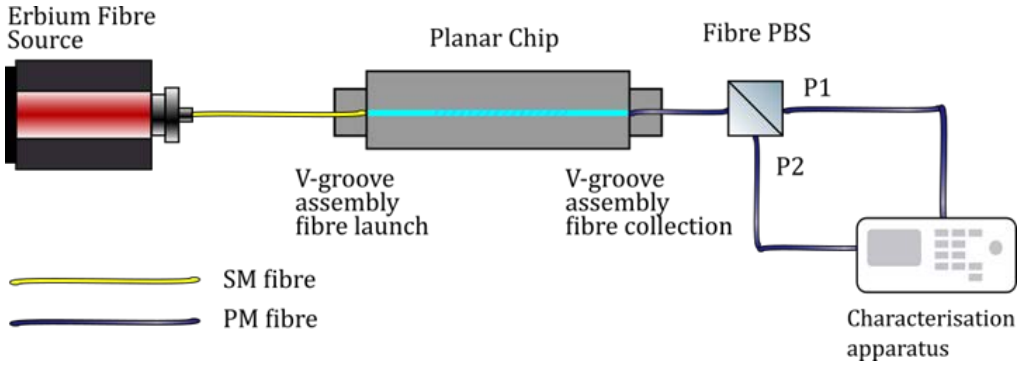

Figure 3.8 – Setup for device characterisation in transmission. The characterisation apparatus is comprised of a power metre and an OSA. Nomenclature: PBS: polarising beam splitter. PM: polarising maintaining. SM: single-mode.

measurements by optimisation of the transmission power through the fibre network. The transmission efficiency has been measured as greater than 50% through the fabricated chip, which includes all coupling and transmission loss up until the output of the collection PM fibre. Power at the output of the collection fibre have typically been 2-3 mW, which has been adequate for power measurements.

The PER has been obtained by simultaneously measuring the transmitted power at each port of the fibre PBS using two optical power meters (Exfo). The optical power metres power readings have been verified to be within 15%; the power readings have been calibrated to adjust for the discrepancy. The PER has been calculated from equation (3.9) for each waveguide fabricated on the chip.

$$PER\,(dB) = 10\,log_{10}(\frac{P_{TE}}{P_{TM}}) \qquad \textbf{(3.9)}$$

The PER has been plotted with respect to grating length in Figure 3.9. The grey area indicates where the PER of the source has restricted the measurement of waveguides with small PER. The chip was fabricated with three waveguides with gratings of 20 mm in length, which have been plotted separately on the graph. The average PER for these waveguides has been calculated as 4.9±0.7 dB; the error has been taken as the standard deviation of the PER measured. The large variation may be caused by variation in the waveguides during the fabrication process.

The theoretical study has predicted a linear increase of PER with respect to grating length. Figure 3.9 plots the measured PER and a line of best fit obtained by linear regression. Previous grating based loss measurements have shown that the difference in propagation losses for TE and TM polarisations to be less than 0.01 dB/cm [86], and the line intercept has been set at the origin. The large variation from the linear regression may also be caused by the multimode nature of the waveguides. The grating refractive index modulation, Δn_g, has been inferred from equation (3.4) as $\Delta n_g = 3.17\times10^{-3}$, which is of the same order of magnitude than previous values of Δn_g that have been measured through grating DUW on SoS (Section 2.5.4). The following section describes the wavelength response of the tilted gratings.

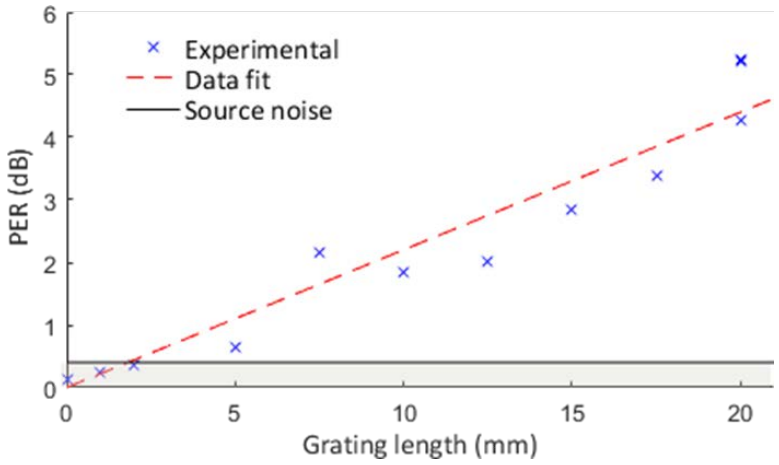

Figure 3.9 – Experimental PER with respect to grating length.

3.5.3 Grating bandwidth characterisation

The characterisation of the waveguide and tilted grating spectral response has been carried out with the setup of Figure 3.8 using with an OSA (Ando AQ 6317B). The transmission of one waveguide with a tilted grating with length of 20 mm has been measured. The spectra from the two output ports of the fibre PBS have been measured successively.

The measured spectra of the system's output and input source has been presented in Figure 3.10. Port 1 and port 2 of the fibre PBS correspond to the TE and TM polarisation modes, respectively. The TE component has been measured as greater than the TM component, as predicted by the theoretical model. The range has been restricted to the C-band for further processing; the limits have been marked on Figure 3.10 (a) by vertical lines.

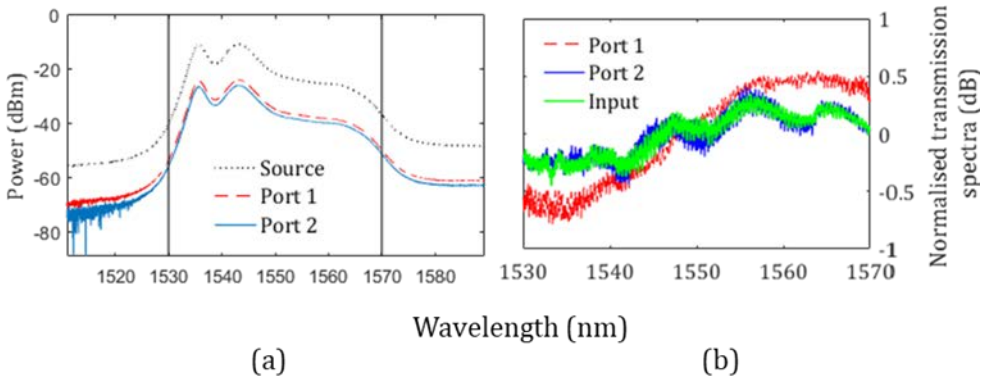

Figure 3.10 – (a) Transmission spectra of 20 mm waveguide with 45^0 tilted grating. (b) Normalised transmission spectra at input and output ports of the fibre PBS.

The spectra of the background have been removed from the spectra of the signals measured at Port 1 and Port 2. The spectra have been normalised to the mean value of the power, which is shown in Figure 3.10 (b) each port of the fibre PBS (P1, P2). The transmission spectra at the output of the chip is labelled as "Input" Figure 3.10 (b). The measurements show good spectral correlations between the input port of the fibre PBS and P2; the standard deviation of both these signals has been calculated as 0.19 dB. The fluctuations in P1 of the fibre PBS have been measured as significantly higher, with the standard deviation of the signal equal to 0.43 dB. Anomalies in the spectra may be caused by the fibre PBS and further characterisation is required. The design, fabrication and preliminary characterisation results have been presented in the proceedings of the 2015 European Conference on Lasers and Electro-Optics [105].

3.6 Fabrication and characterisation enhancement

The following section presents detail of further work that has been conducted to enhance the fabrication and characterisation of tilted gratings by DUW.

3.6.1 Adaptations of bandwidth characterisation test setup

The section describes the modification of the characterisation system to measure the spectral response of waveguides with tilted gratings. The experiment presented in section 3.5.1 was adapted by removing the fibre PBS. The modified setup is shown in Figure 3.11. The scheme for coupling on and off chip was changed. The output PM fibre was mounted in a fibre holder and imaged through a microscope objective. The

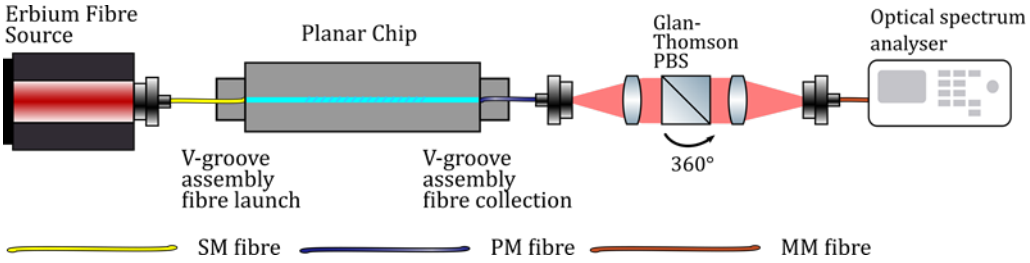

Figure 3.11 – Free space characterisation using Glan-Thomson PBS mounted in a rotation mount. A mirror mounted on a flip mount has been to switch the beam between the power metre and the OSA. Nomenclature: SM: single-mode. PM: polarising-maintaining. MM: multi-mode.

signal was transmitted through a bulk optics Glan-Thomson polariser mounted in a rotation holder. The Glan-Thomson crystal has a polarisation extinction ratio more than 50 dB. The signal was transmitted to another microscope objective for coupling into a multi-mode (MM) fibre connected to an OSA for subsequent spectral analysis.

The system's fibre-to-fibre coupling efficiency has been characterised using a power metre at the output of the MM fibre. The setup coupling efficiency has been measured at 83%. The losses have been attributed to the modal mismatch of the different fibres employed. The rotation of the polariser has caused degradation in coupling; this has been attributed to the displacement of the beam with crystal rotation. For subsequent experiments, the coupling of the beam into the MM fibre has therefore been optimised between each successive measurement.

The transmitted spectra in the C-band has been presented in Figure 3.12 for spectra collected at four different orientations of the polariser. The noise in the data may have been caused as an artefact of the low signal level due to operating near the OSA's noise floor level. A reduction of the spectral bandwidth may improve the noise level of the signal. The flat spectra are indicative that the grating has a wide bandwidth, which agrees with this supporting theoretical study and historical reports in the literature.

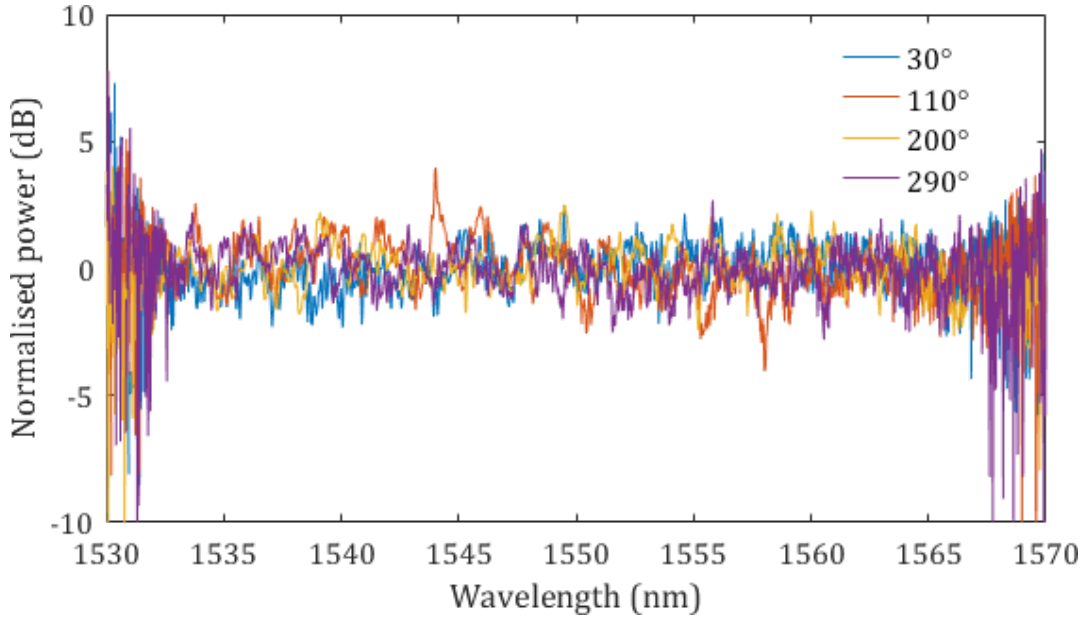

Figure 3.12 – Normalised transmission spectra of waveguide with 20 mm 45^0 tilted grating at 4 different rotation angles of the Glan-Thomson polariser.

3.6.2 Curvature compensation for PER enhancement

The study presented in section 3.5 indicated that the PER efficiency of 45° tilted gratings fabricated by DUW is linear with respect to grating length. The fabrication of longer gratings was investigated as a method for increasing the PER. Longer chips of length 60 mm have been prepared for DUW. Bow in longer chips has been observed, which is an inherent feature of the FHD fabrication process. This section describes the investigation into measuring the curvature of chips and methods for compensating for this.

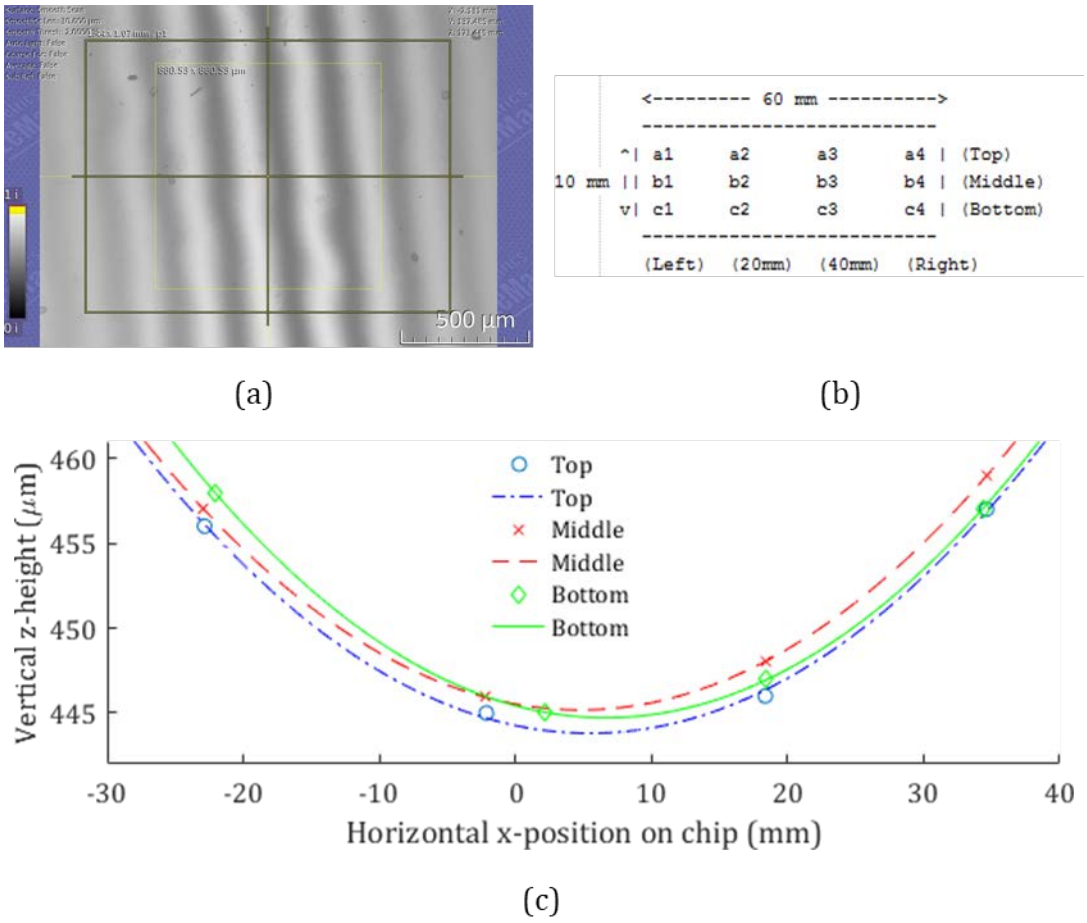

Figure 3.13 – (a) White light interferometry scan of chip showing interference fringes to establish the chip height. (b) Schematic of scan points on the chip. (c) Chip height scans and fits to second order polynomial to establish bow.

The height of the surface of the chip has been measured by white light interferometry. A test chip of length 60 mm and width 10 mm was scanned for interference fringes and taken the reading the associated height –see Figure 3.13 (a). Multiple scans of area ~900×900 µm^2 have been taken across the chip – see Figure 3.13 (b). The resulting chip height (z) across the length (x) and width (y) of the chip have been mapped. The measurements have been fitted to a second order polynomial using the Matlab curve fitting toolbox. Figure 3.13 (c) shows the measured height variation across the surface of the test chip, with the fitted second order polynomial. The bow has been estimated using the second order coefficient of the fitted sample profiles.

Chips are usually mounted in the middle of a vacuum chuck of length 20 mm – see inset of Figure 3.14. Figure 3.14 plots the vertical deviation from the centre of the

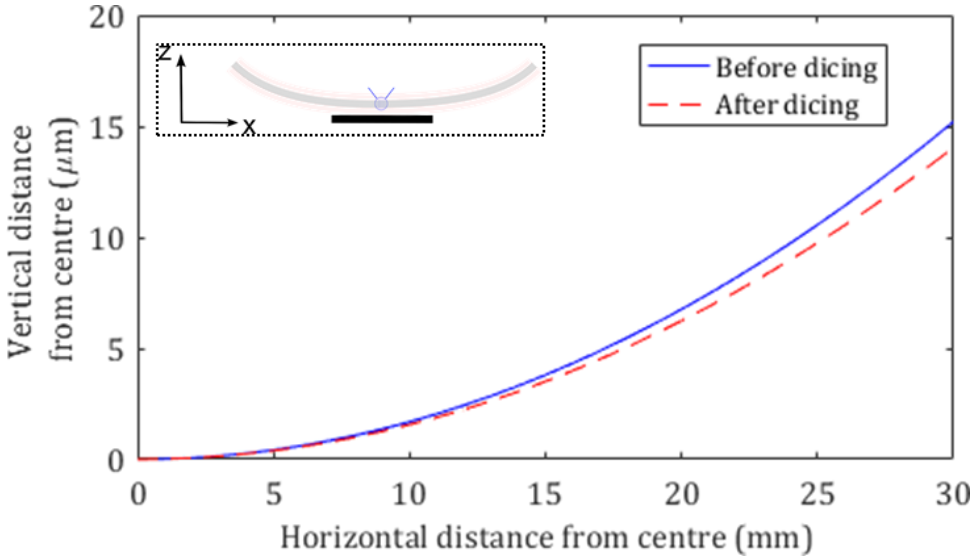

Figure 3.14 – Vertical offset as a function of distance from the centre of the chip caused by bow in chips before and after dicing in the silicon back layer of a chip of length 60 mm chip. Inset: cross-section of chip of length 60 mm mounted on a chip holder of length 20 mm. The core layer has been marked in grey and the position of the UV focused laser spot in indicated on the diagram.

core layer; the origin has been taken as the position of the centre of the core layer at the centre of the mount. For chips of length 20 mm, the implications of bow are not significant as the vertical deviation is less than 2 μm at a distance of 10 mm from the centre. For longer chips (60 mm), the vertical deviation has been calculated as 14 μm at 30 mm from the centre. The large vertical deviation for longer chips may have caused defocusing of the small spot from the core and reduction in the grating contrast. Precision micromachining processing was tested to assess if bow in long chips could be reduced by releasing stress in chips. Five grooves of depth and width 50 μm were made by dicing the silicon underside of the chip across the chip's width. Each groove has been separated by 10 mm. No significant reduction of bow has been measured after dicing – see Figure 3.14.

The issue with bow can be overcome by mapping the bow to compensate for height variation across the chip. Chip curvature compensation would provide an effective strategy for the fabrication of long tilted gratings with optimised refractive index contrast to readily achieve integrated polarisers with PER of 15 dB.

3.7 Conclusions and further work

The chapter has described the theoretical and experimental study for the implementation of 45º tilted gratings in SoS DUW waveguides for polarisers. Proof-of-concept devices have been demonstrated with PER of 0.25 dB/mm and wavelength dependence better than 0.3 dB in the C-band. Strategies for improved fabrication and characterisation methods for achieving devices with bandwidth better than 0.3 dB and PER of 15 dB in the C-band have been outlined. The broadband nature of the grating permits compatibility with SoS wafers systems of different birefringence through DUW.

The work may be extended through the investigation of 45º tilted gratings for broadband polarisers operating at wavelengths in the visible. High PER tilted grating-based polarisers have been demonstrated in fibre technologies [106] and analogous implementations in a planar platform would therefore extend the range of integrated components that DUW offers in these wavelength regimes (Section 2.5.3). Further work would investigate employing different laser processing methods with potential for stronger refractive index modulation. Small angle tilted gratings that have already been realised in fibres using such commercial systems at wavelengths of 213 nm [107]. These direct UV writing schemes have been recently demonstrated as suitable for the fabrication of waveguides by DUW in SoS [108]. This work could result in quadratic improvement of the PER of tilted grating based integrated polarising devices.

The fabrication techniques could be applied for use with other integrated buried waveguide silica-platforms. The techniques could be used in photolithographic buried waveguides to control temperature-related polarisation fluctuations in planar optical gyroscopes [109]. Integration with ring resonator structures will also permit the development of characterisation methods for verifying the loss induced by the grating fabrication process [110]. Investigation of losses caused by grating fabrication may be critical for the adoption of the architecture in schemes requiring low loss components, such as the integration of free space plate polarisers used in for pseudo-random number generators in quantum information processing [111].

Chapter 4 Integrated polarising beam-splitters based on tilted gratings

Polarisation-selective devices are important components for optical networks for applications in communications, sensing and quantum information processing. The polarising beam-splitter (PBS), capable of splitting an input field into two polarised output fields, is one such device. This chapter will describe a novel route towards integrating polarisation selective coupling between two independent waveguides utilising tilted gratings. Design, fabrication and characterisation results demonstrating proof of concept of this architecture are presented. The study is supported by numerical modelling and an analytical theory to permit further optimisation of the coupler performance. Relevant background on PBS technologies is presented as a preamble.

4.1 Background on integrated polarising beam-splitters

Conventional fibre-based PBS devices usually employ bulk optics where the natural birefringence of crystals is used to separate polarisation states, such as Wollaston prisms, Glan-Thomson prisms and Nicol prisms. However, such crystals are bulky and do not offer routes to scaling with further integration. Free-space grating-based architectures have been proposed to separate polarisation states, but either require metallic overlayers that can be lossy [112], [113], complex manufacturing steps [114], or delicate alignment procedures [115]. Various architectures for integrated polarising couplers have been proposed. These include schemes using multimode interference [116], directional couplers [117], Mach-Zehnder interferometers

[118], [119], micro-ring resonators [120], metasurfaces [121], or hybrid plasmonic waveguides [122].

An alternative approach for integrated polarisation-sensitive devices consists of using tilted gratings, as described in Chapter 3. The following section will describe how the fabrication platform used in this study can be used to design novel planar architectures for polarising and signal routing applications.

4.2 Architecture of integrated polarising beam splitter based on tilted gratings

Chapter 3 described how a polariser can be fabricated by expelling the TM mode of a waveguide into a radiation mode. The planar geometry of the SoS platform allows a parallel waveguide containing a grating to perform the reverse phenomenon of collecting the radiation mode and coupling back into a propagating mode. The PBS architecture is illustrated in Figure 4.1.

An unpolarised electric field is launched into an input waveguide (W1) with a grating tilted at an angle $\theta = 45°$. The TM component of W1 is coupled to a polarised radiation mode through the gratings with large tilt angles (Section 3.3.2). A second adjacent waveguide (W2) is used for the output port. W2 contains an identical tilted grating to W1, which allows the polarised component of the radiated electric field from W1 to be coupled to a waveguide mode in W2 – see Figure 4.1 (a). The refractive index of the planar core layer, n_{co}, is greater than that of the surrounding cladding, n_{cl}, which can be achieved through flame hydrolysis deposition (Section 2.3.2). All the inter-channel radiated modes are confined vertically in the planar core layer, as illustrated in Figure 4.1 (b). This propagation mechanism through the slab waveguide layer will be referred to as planar mode coupling (PMC). In Figure 4.1 (b), the orthogonal polarisation states have been represented with white arrows. The large tilt angle allows the coupling to be broadband between independent waveguides W1 and W2 (Section 2.5.1). This chapter's study has focused on the transmission from W1 to W2. In this configuration, the architecture is best described as a polarising coupler.

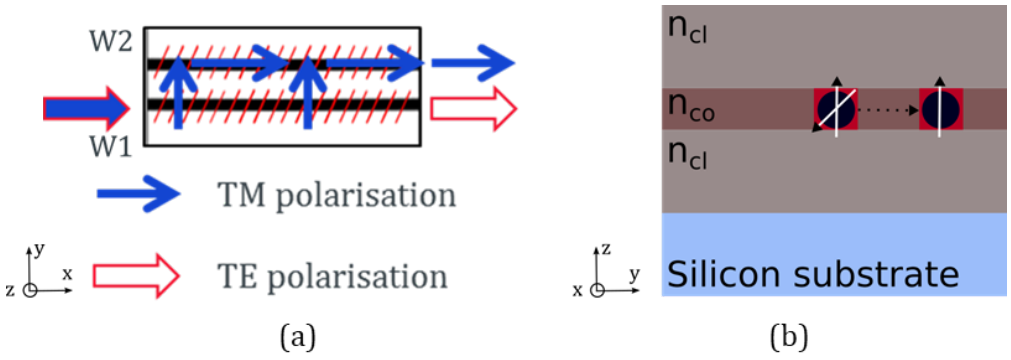

Figure 4.1 – Integrated polarising coupler principles of operation. (a) Top view of the core layer illustrating the ideal coupling of the polarised radiation mode between two independent waveguides. (b) Cross-section of the output facet of the SoS device illustrating planar mode coupling. Here, $n_{co} > n_{cl}$.

4.3 Modelling

The polarising coupler architecture that has been described previously makes use of 45^0 tilted gratings in two spatially independent waveguides in two successive coupling mechanisms: first, (i) from waveguide mode to a radiation mode, followed by (ii) a coupling from a radiation mode to a second waveguide mode. The analysis of waveguide-to-radiation mode coupling for low-index contrast technologies has been largely carried out in fibre geometries [123]–[125], with a gap in the literature for monolithic devices.

The following section presents a theoretical study to further the understanding of this planar architecture. The study has been conducted as part of collaborative work with Dr. Nina Podoliak and Dr. Peter Horak from the Optoelectronics Research Centre (ORC). The contributions are detailed throughout this section and summarised in Appendix B.

4.3.1 Theoretical description of planar mode polarising coupler

The theoretical refractive index profiles of the waveguide, n_w, and grating, n_g, that have been used in this study were presented in Section 3.3.2. The parameters n_w and n_g in a 2-dimensional plane, defined by x and y in Figure 4.1, have been described in equations (3.5) and (3.6), which have been reprinted for ease of reading.

$$n_w(x,y) = n + \Delta n_\omega \; exp\left(-\frac{y^2}{\sigma^2}\right) \tag{3.5}$$

$$n_g(x,y) = n + \left[\Delta n_\omega + \Delta n_g \; sin\left(2\pi\frac{x-y}{\Lambda_G}\right)\right] exp\left(-\frac{y^2}{\sigma^2}\right) \tag{3.6}$$

In equations (3.5) and (3.6), Δn_w is the photo-induced refractive index shift with respect to the photosensitive core layer, σ is the radius of the waveguide defined by DUW, Δn_g is the peak-to-peak index modulation of the sinusoidal grating and Λ_G is the grating period. The numerical modelling implementation and analytical derivations of the structures presented in sections 4.3.1.1 and 4.3.1.2 were conducted by Dr. N. Podoliak.

4.3.1.1 Finite-element modelling of polarising grating coupler

The work presented in this section details the development of a numerical model to describe the coupling between two spatially independent waveguides using 45^0 tilted gratings and planar mode coupling. The waveguides and gratings have been modelled by finite element modelling using the COMSOL Multiphysics ® numerical simulation software package.

The low refractive index contrast of DUW waveguides has been found to necessitate long interaction lengths to study higher efficiency grating-based field effects. The waveguide mode width was reduced and the grating modulation increased for the numerical simulations to improve the efficiency of the grating-based field effects in these structures. A preliminary study was conducted to determine the '*b*' parameter, which was introduced in Section 3.3.3 as a figure of merit to compare the waveguides. The simulations parameters used were σ = 2.15 μm, $\Delta n_g = 1\times10^{-2}$. The *b*-parameter was calculated for this waveguide and grating as b = 63.4 μm^{-1}. The *b*-parameter of this model is in good agreement with the '*b'*-parameter presented in Chapter 3 (b = 59.1 μm^{-1}). The polarisation-dependent responses in terms of Δn_g and L_g have also been found to be consistent with the work presented in the previous chapter. This architecture allows the coupling of waveguide modes to a highly-polarised quasi-plane wave radiation mode, which agrees with the simulations seen in Chapter 3.

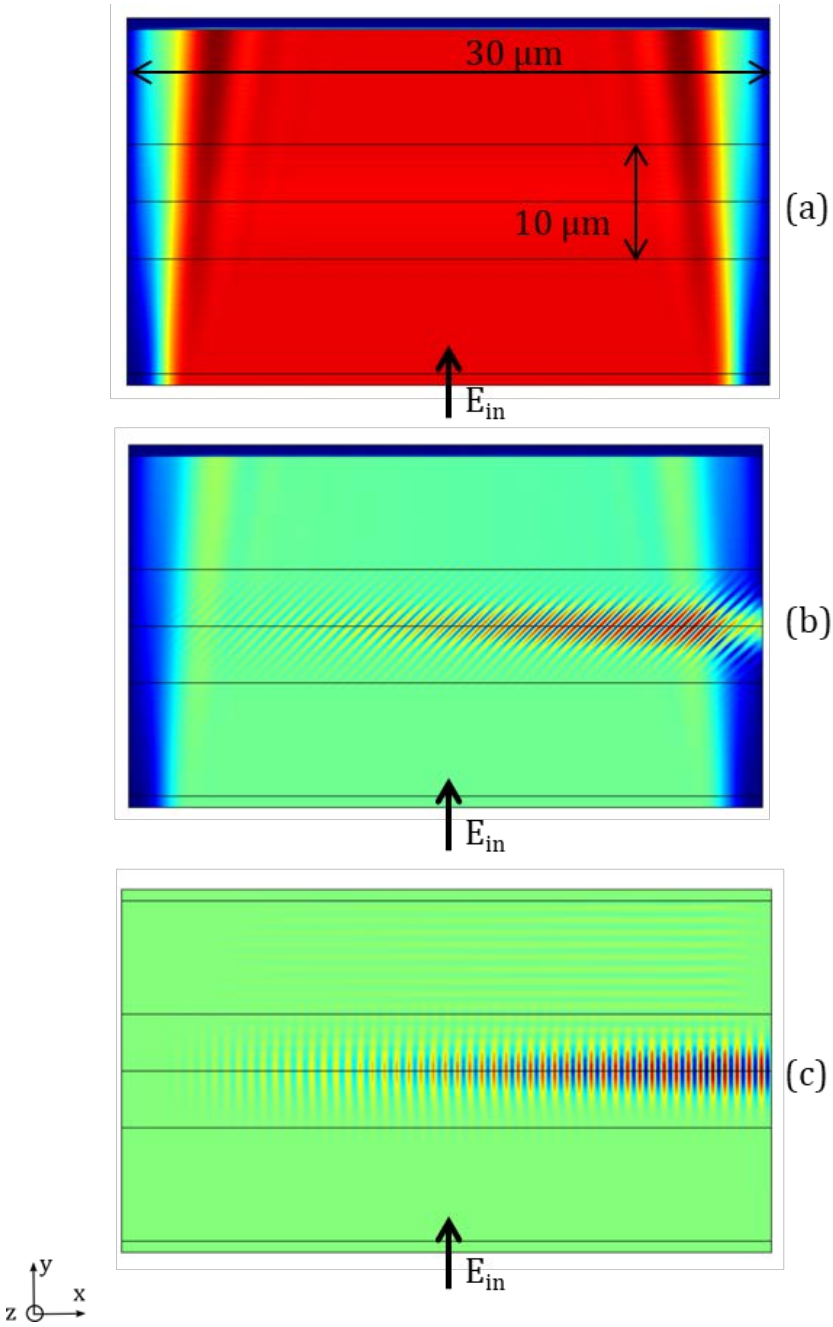

Figure 4.2 – Electric field simulations of the polarising tilted grating coupler. The input electric field is denoted E_{in}. (a) Propagation of planar wave through slab waveguide layer with no grating in the waveguide (b) Coupling into waveguide through tilted gratings. (c) Electric field build-up through waveguide. The waveguide boundaries have been outlined for clarity. Simulation figures provided by Dr. N. Podoliak. Dimensions are marked on sub-figure (a) and are identical for all sub-figures. Electric field units are arbitrary.

To investigate the reverse coupling process, the interaction between a plane wave and a tilted grating in a waveguide was modelled. An electric field with a single-out

of plane (TM) polarisation has been excited at the bottom surface of the test structure. This has been used to approximate a quasi-plane wave propagating through the planar core layer, which corresponds to the electric field radiated from the in-line tilted grating based waveguide polariser described in Chapter 3. Figure 4.2 summarises the electric field response. The system dimensions have been indicated in Figure 4.2 (a) and they are identical for each sub-figure. The grating length is L_g = 50 μm.

Two systems have been simulated. First, a reference waveguide without a grating – see Figure 4.2 (a). The electric field distribution shows that the plane wave travels through the planar layer and does not couple into a waveguide mode. A second test structure – see Figure 4.2 (b) –contains a waveguide with a grating. The electric field distribution is aligned with the grating planes, suggesting that there is indeed an interaction between the slab waveguide mode and the grating.

Figure 4.2 (c) shows the difference in electric fields between the solutions of the reference (a) and test (b) structures. The light has coupled to the fundamental mode of the waveguide. A build-up of the field has been observed along the waveguide's direction of propagation, showing that there is coupling from the plane wave to the waveguide mode through the grating structure.

Waveguide-to-waveguide coupling based on tilted gratings has been modelled. Two spatially independent waveguides with identical tilted gratings have been used. The radiated quasi-plane wave from the input waveguide has interacted with the collection waveguide. The electric field response has been found to be in good agreement with the simulations results presented in Figure 4.2. Simulations have been conducted with twelve gratings of different lengths, with L_g between 10-200 μm. The numerical model has provided insights into the scaling of the device, which has been used to develop an analytical description of the architecture.

4.3.1.2 Analytical description of the architecture

This section presents an analytical solution to the architecture described above in terms of the DUW fabrication parameters. The normalised optical power of the TM-polarised mode along the length of the grating, *x*, in the output waveguide has been given by equation (4.1). The expression has been found to be in good agreement

with the numerically calculated optical power in the output waveguide –see Figure 4.3 (a).

$$P_2(x) = \alpha^2 x^2 exp(-\alpha x) \tag{4.1}$$

In equation (4.1), the parameter α is given in terms of the DUW fabrication parameters, and is related to the refractive index modulation, Δn_g, waveguide radius, σ, mode field radius ω_0 and grating resonant wavelength, λ_R. The parameters have been linked by equation (4.2).

$$\alpha = \pi^2 \sqrt{2\pi} \frac{\Delta n_g^2}{\lambda_r^2} \frac{\sigma^2 \omega_0}{\sigma^2 + \omega_0^2} \tag{4.2}$$

Δn_g can be controlled during the DUW process but is limited by the photosensitivity of our devices and the writing system. ω_0 is intrinsic to achieving single mode operation at the design wavelength and the corresponding λ_R is used as a grating design parameter. σ is linked to the DUW step in the fabrication process and has been empirically obtained (Section 2.4.3). The model has assumed of Gaussian mode and sinusoidal gratings, as has been described by equations (3.5) and (3.6). The model has also assumed that the operation wavelength is resonant with the grating and there is perfect propagation of the electric field in the waveguides neglecting the propagation loss.

Equation (4.1) predicts that the power coupled to the output waveguide reaches a maximal value of 54% of the input power independently of Δn_g. The optimal grating coupling length is given by $L_C = 2/\alpha$. A hypothesis for this observation is described in Figure 4.3 (b). The TM component of the field in W1 has been coupled to a radiation mode by the tilted gratings. The field intensity of W1 has decreased as it has propagated through the waveguide. The radiated field has been coupled into a waveguide mode by the tilted gratings in W2. The field in W2 has increased in strength coherently during the propagation through the waveguide, up until the field has reached a critical point where it has been coupled out of the waveguide mode to another radiation mode. The implications of these findings are summarised in the following section.

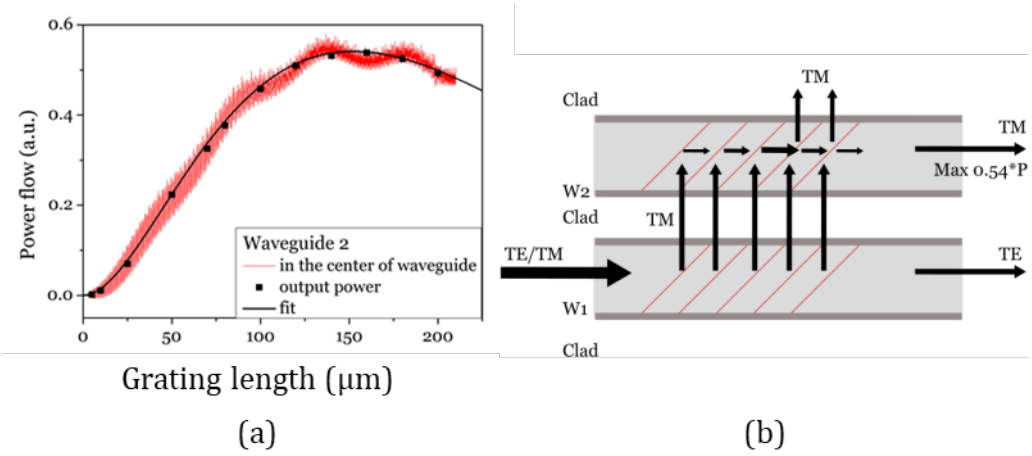

Figure 4.3 – (a) Spatial dependence of the power in output waveguide as a function of grating length. Figure provided by N. Podoliak. (b) Schematic description of the decreasing coupler efficiency for devices with long gratings.

4.3.2 Application to fabricated devices

This study has developed a theoretical framework to describe how spatially independent monolithic DUW waveguide-pairs can be combined to form polarising couplers through 45^0 tilted gratings. The gratings used have been identical. The architecture has permitted the coupling of a highly polarised input waveguide mode to an output waveguide mode that is spatially independent. This has been achieved through planar mode coupling between waveguides using radiation modes. Figure 4.4 shows the normalised polarising coupler output as a function of grating length described by equation (4.1). The optimal coupling length, L_C, has been calculated at ~15 mm for the devices described and fabricated in Chapter 3. The following section describes the fabrication of the polarising coupler architecture through PMC. The three waveguides with gratings of 20 mm from the chips fabricated in Chapter 3 will be considered in the following discussion. The grating length is therefore not optimised for the refractive index modulation of the grating that has been calculated.

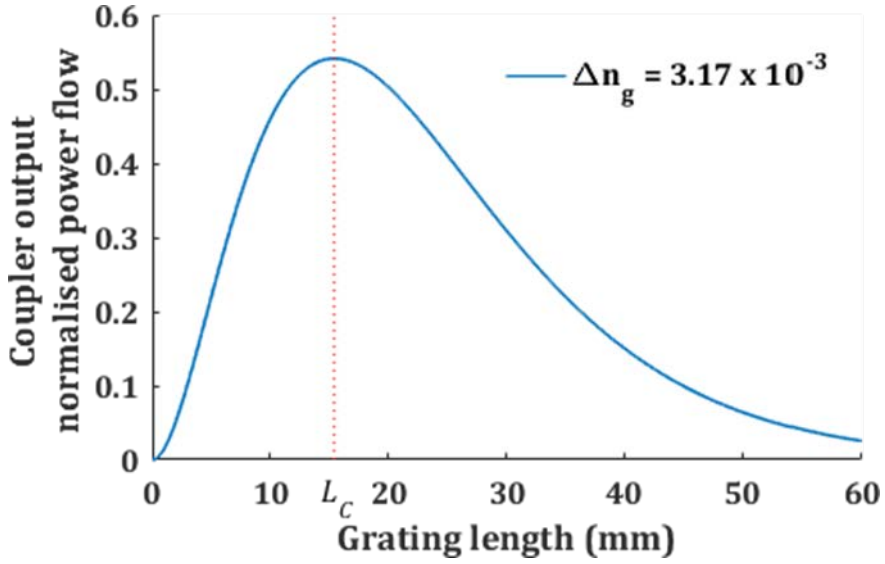

Figure 4.4 – Normalised output coupler power as a function of length of a tilted grating waveguide pair, taken from equation (4.1). The optimal coupling length, L_C, for the devices presented in Chapter 3 has been indicated.

4.4 Fabrication of polarising couplers

The polarising coupler architecture requires two identical and spatially independent waveguides with phase-matched pairs of gratings. The chip must also support PMC. The following section will highlight how the DUW fabrication steps have permitted the realisation of these devices.

The wafer platform must support the propagation of a quasi-plane wave that is vertically confined. Wafer NB12/18 was used for this study. The wafer has a 16.5 μm thick thermal oxide underclad. A 5.1 μm photosensitive germanoborosilicate planar core layer has been deposited by flame hydrolysis deposition (FHD), followed by an 18.1 μm FHD overcladding layer. The overclad layer has been matched to the index of the underclad. The refractive index contrast between the core and cladding layers has been measured as 0.66%. The refractive index contrast has permitted vertical confinement in the core layer, which is a requirement for testing PMC. Full details of the wafer have been presented in Appendix C.

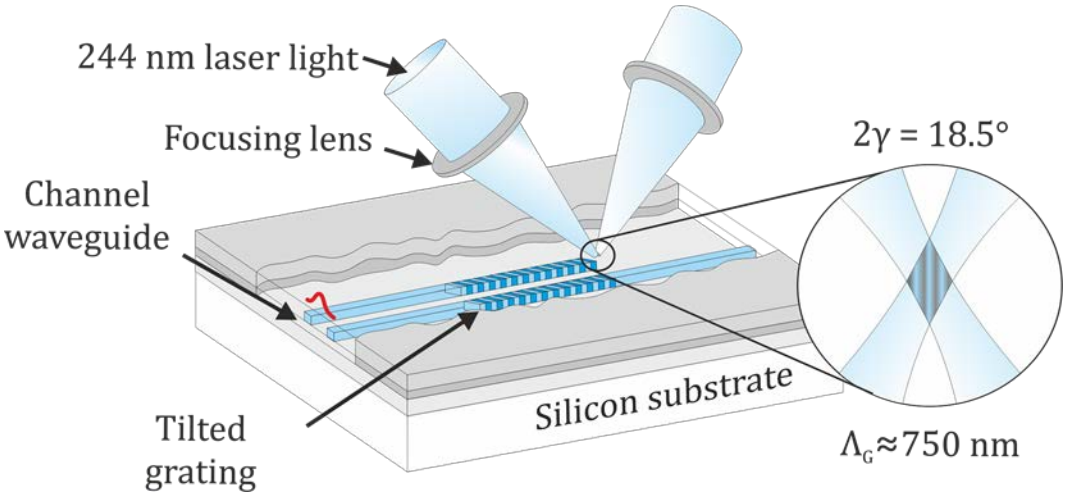

Figure 4.5 – DUW for fabrication of waveguide-pairs with 45° tilted grating for polarising couplers.

Two parallel waveguides with 45° tilted gratings of equal length (20 mm) have been fabricated by DUW in the core layer of a planar chip, as illustrated in Figure 4.5. The waveguides were separated by 250 μm to avoid evanescent coupling. The phase tolerance of the fabrication system allows the gratings of the independent waveguides to be phase matched.

4.5 Characterisation of polarisation couplers

The following section describes the characterisation system for the first demonstration of an integrated polarising coupler based on tilted gratings operating in the C-band, with polarisation extinction ratio (PER) greater than 28.5 dB.

4.5.1 Fibre-based setup characterisation

The polarisation coupler device was characterised in transmission with the setup described in Figure 4.6. The source was an unpolarised erbium-doped fibre amplifier (IPG Photonics) spanning the C-band (1530-1570 nm). The source was launched through port A through a single mode (SM) fibre mounted in a single port v-groove assembly and butt-coupled to the chip.

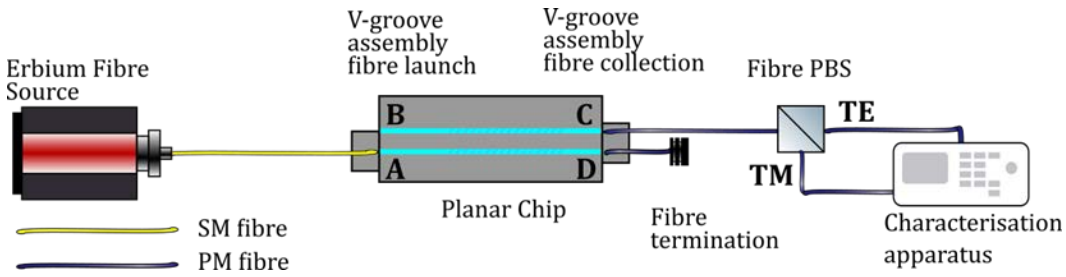

Figure 4.6 – Fibre-based characterisation setup for measurement of the PER ratio of integrated polarising coupler based on tilted gratings.

The transmitted signals were collected simultaneously at both ports C and D through two 1-metre long polarising-maintaining (PM) fibres mounted in a two-port fibre v-groove array. The polarising coupler response are given with respect to the transmission from ports A to C. Port D has been terminated to avoid back-reflection into the chip. The output signal at port C was connected to a commercial fibre PBS (Thorlabs PBC1550SM-FC). The fibre PBS was used to split the orthogonal polarisation components, which were measured successively using an optical spectrum analyser (OSA) (Ando AQ 6317B). Index-matching liquid was used at the interface between the chip and the v-groove assemblies to reduce back-reflection and scattering.

4.5.2 Spectral transmission characteristics

To investigate the spectral response of the system, the transmitted spectra at port C were normalised to the source spectra. Figure 4.7 shows the unfiltered spectra at port C (denoted “Insertion loss”), and the filtered TM and TE signals after the fibre PBS. The insertion loss from ports A to C has been measured as 15.5 dB. This includes transmission and all coupling losses, including fibre-waveguide coupling, grating coupling loss and planar mode coupling. The principle component is thought to arise from the PMC. The loss between port C and the TM out-coupled signal has been measured as 5.9 dB. This high loss has been attributed to the fibre PBS components employed in the setup.

The TM component of the output has been measured as stronger than the TE component. This indicates that the TM polarisation state has mainly been ejected from the input waveguide and collected at the output of the coupler. The flat spectral response observed for the TM mode indicates that the bandwidth of the grating is

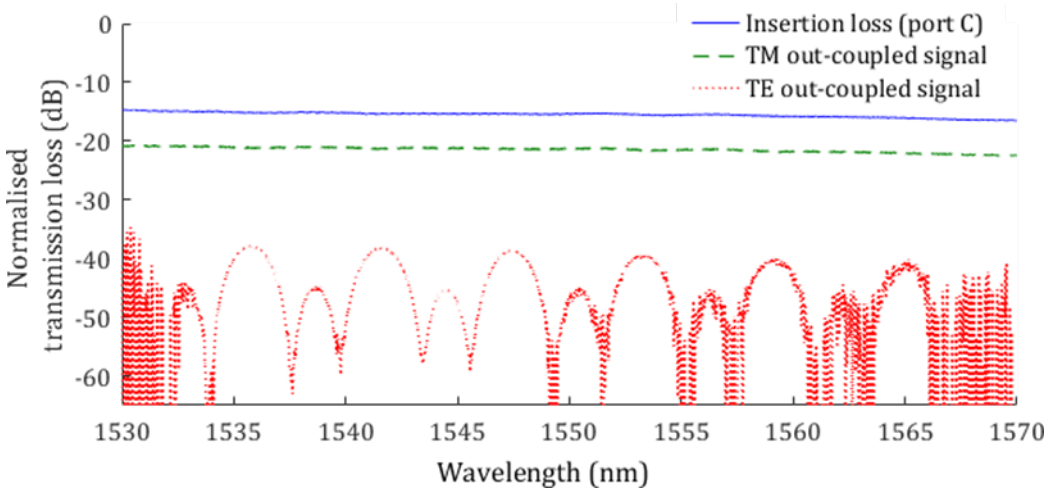

Figure 4.7 – Transmission spectra at port C of the integrated polarisation coupler.

extremely large. As expected, the tilted gratings do not operate like a conventional Bragg reflector (Section 2.5.1).

The TE output characteristics are of interest. The spectra show a 6-nm periodic separation between the high peaks. The chips are susceptible to higher order modes due to the large refractive index contrast between the core and cladding layers. Mode beating has been considered as the cause of this effect. However, in view of previous measurements obtained for similar multi-mode waveguides [8], this is unlikely due to the period of oscillation.

The phenomenon is believed to be an artefact of the fibre PBS unit used in this characterisation setup. The behaviour has been reproduced using an in-line fibre polariser in lieu of the fabricated chip. After the device, both a large TM and small residual TE component may be travelling through the system at a different velocity due to birefringence. Due to imperfections in the fibre PBS, a leaky TE component may appear; the leaky TE mode at the fibre PBS may beat with the residual TE mode travelling through the PM fibre. This occurs due to the phase difference between the two fields, causing beating between the TE modes and leading to the spectral fringes observed. The PER between the flat TM spectra and the peaks of the TE spectra is approaching the specified PER of the fibre PBS (18 dB). Consequently, under the current setup it not possible to characterise the PER of this device any further.

4.5.3 Preliminary discussion

The preliminary results presented above demonstrate the proof of concept of the architecture as a polarising coupler with PER greater than 17 dB for waveguide-pairs. The insertion loss from ports A to C has been measured as 15.5 dB. This includes transmission and all coupling losses, including fibre-waveguide coupling, grating coupling loss and planar mode coupling. The principle component is thought to arise from the PMC. The wavelength dependence variation has been measured as less than 1.9 dB across from 1530-1570 nm, which is one order of magnitude greater than predicted by the theoretical investigation. This could be caused by variations in the planar layer and stage tolerances, which would reduce the bandwidth.

The TM output signal collected after the fibre PBS has revealed an additional loss of 5.9 dB, which has been attributed to losses in the fibre PBS. The PER characterisation of the device under test has been experimentally limited by the in-line fibre components. The following section describes improvements to the characterisation setup.

4.5.4 Polarisation extinction ratio measurement

The characterisation setup was modified to measure higher PER at the output coupler port (port C) of the device – see Figure 4.8. The signal was collected using a PM fibre, which was coiled to act as a spectral mode stripper. This has been necessary to collect only the transmitted waveguide mode and filter any scattered light that may be coupled into the cladding modes of the collection fibre. The setup was first tested where the output of the waveguide was directly imaged using a microscope objective. With this arrangement, the highest PER measured was under

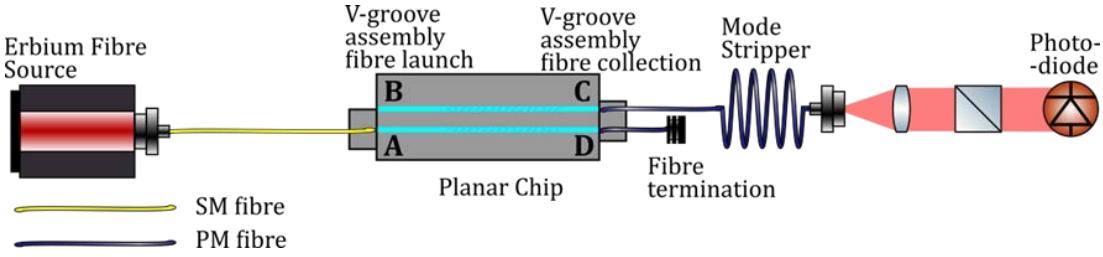

Figure 4.8 – Characterisation setup with spatial filtering using bulk crystal polariser.

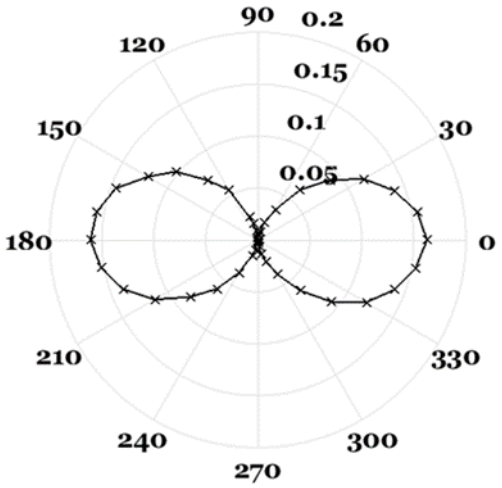

Figure 4.9 – Measured output power as a function of the rotation of bulk optic polariser, showing single polarisation.

5 dB. In principle, no TE light should couple to waveguide 2. However, scatter from the launch may occur and spatial filtering of the output, via the PM optical fibre, was required to improve the PER measurements.

The PM fibre was imaged by a microscope objective and transmitted through a Glan-Thomson polariser with a high PER (> 50 dB). The crystal polariser has been mounted in a rotation mount. The collected beam power has been measured with a photodiode as function of the angle of the crystal polariser; the power measurements have been plotted in Figure 4.9. The PER at port C has been as 28.5 dB. The PER is likely to be limited by the alignment tolerance of the PM fibre within the v-groove assembly which is specified as 29 dB (angular misalignment of 2°).

4.6 Conclusions and further work

This chapter has described the first demonstration of an integrated polarising coupler based on 45° tilted gratings in waveguides fabricated by DUW. The study has been published in the proceedings of the 2016 OSA Advanced Photonics Congress [126]. A summary of the device transmission properties is shown in Figure 4.10. The PER measured at ports C and D are 28.5 dB and 4.9 dB, respectively. The fabricated device has relied on the coupling to and from radiation modes between waveguide modes, and their propagation through a slab waveguide through planar

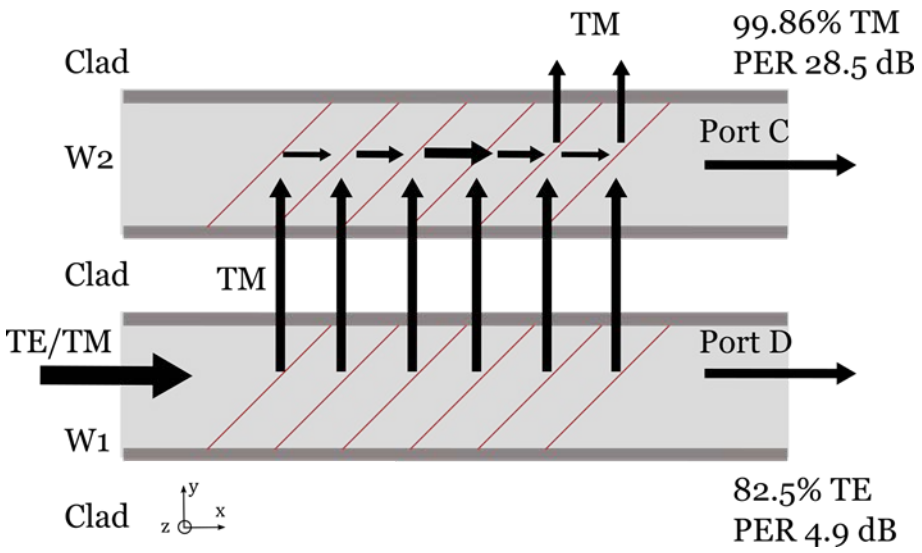

Figure 4.10 – Summary of the device transmission properties.

mode coupling (PMC). This novelty of this implementation is its reliance on the excellent phase stability of the DUW fabrication platform.

The study has been supported by a theoretical framework for the design and optimisation of polarising couplers based on tilted grating. The study predicts optimised coupling efficiencies of 54% and bandwidth impairment less than 0.2 dB is possible with the architecture with uniform gratings. The high experimental losses and greater wavelength dependence observed in this study may be caused by variations in the planar layers fabricated by flame hydrolysis deposition. Further investigation into improving the uniformity of planar core layers help overcome these limitations.

The theoretical framework developed in this chapter has provided tools to design a two-port device for the fabrication of a balanced integrated polarising beam splitter. The grating coupler efficiency may be improved through studies of the apodisation profile of the tilted gratings for low loss applications in fibre networks. Apodisation control is a feature already available on the DUW platform, so further modelling work is required to optimise the grating coupler efficiency. An optimised scheme may be useful as an on-chip inhibitor for cascaded Raman scattering in non-linear processes in SoS; these will be discussed further in the following chapter.

The work may be extended to further exploit waveguide architectures making use of the PMC. The polarisation coupler can be extended through the development of

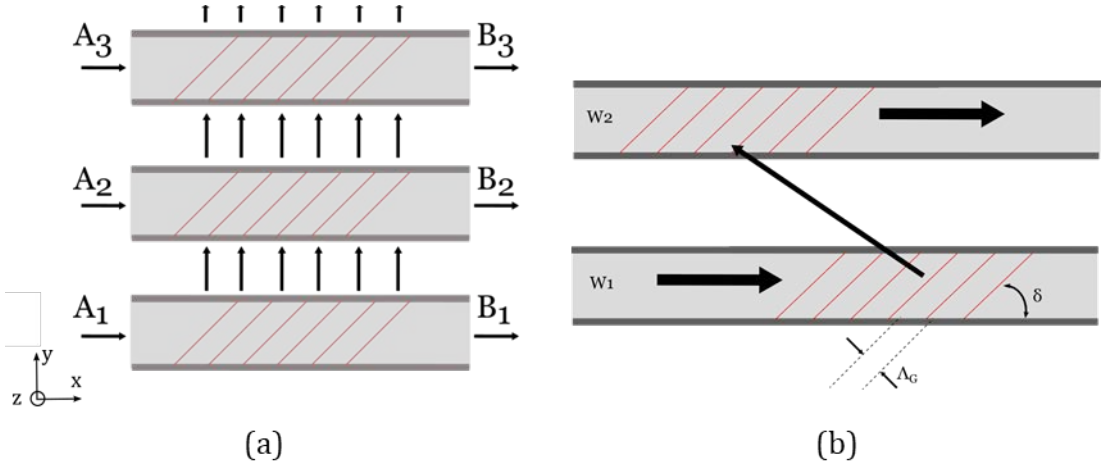

Figure 4.11 – (a) 1-n polarisation-based beam splitting and switching. (b) Planar mode coupling between spatially independent waveguides using tilted gratings with small angles of tilt.

multi-port polarisation dependent beam-switching with coherent control of input beams – see Figure 4.11 (a). The use of tilted gratings with lower angles may be of interest for polarisation independent coupling schemes between spatially separated waveguides through PMC – see Figure 4.11 (b). Both device rely on fabrication systems providing excellent phase tolerance for grating generation and highly uniform planar layer for good propagation through slab waveguides.

Chapter 5 Engineering heralded single-photon sources

Silica-on-silicon (SoS) photonics integrated circuits (PIC) offer a route for the scaling of complex quantum information processing (QIP) experiments through the integration of sources, circuits and detectors fabricated by direct UV writing (DUW) (Chapter 1). This chapter focuses on the adaptation of the fabrication and characterisation methods presented in Chapter 2 to produce a scalable architecture for heralded single-photon sources.

The following pages report the design, fabrication and characterisation of novel SoS highly-birefringent waveguides for the generation of photon-pairs in the visible and telecommunications spectral regions. The study is complemented by experimental investigation to support the development of a scalable platform for the integration of on-chip four photon-pairs source arrays. First, the concepts related to heralded single-photon sources by spontaneous four-wave mixing are presented.

5.1 Silica-based heralded single-photon sources

Quantum photonics emitters may be formed in a plethora of different medium; a review of the current state of the art in single photon sources is not in the scope of this study and the reader is referred to reports in the literature for further information [127]. The following section focuses on the schemes for generating heralded single-photons by spontaneous four-wave mixing (SFWM) in silica to highlight the compatibility with the fabrication platform used in this study.

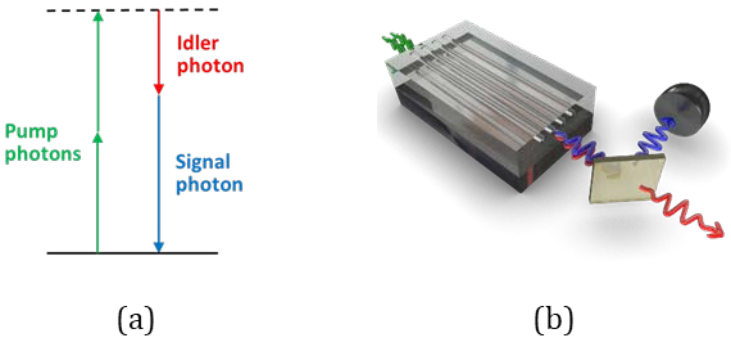

Figure 5.1 – (a) SFWM energy conservation principles. A level scheme depicting the SFWM process. Two pump photons are annihilated to generate two new photons at the signal and idler wavelength. This process inherently obeys energy conservations. (b) Implementation of SFWM in birefringent waveguides, with signal and idler photons separation by dichroic mirrors off chip (Figure courtesy of P. L. Mennea).

SFWM in silica occurs due to a third order, $\chi^{(3)}$, non-linear process [128]. Two photons from pump pulses are converted to a pair of daughter photons, the signal and idler, under the conditions of phase-matching and energy conservation – see Figure 5.1 (a). Birefringent waveguides permit the production of signal and idler photons by SFWM [128] – see Figure 5.1 (b). The signal and idler photons are entangled: the detection of the signal photon heralds the presence of its idler, which can be transferred to a QIP networks for subsequent processing.

SFWM schemes are non-deterministic, and a low $\chi^{(3)}$ in silica limits the photon flux. However, the generated photon-pairs are contained to well defined waveguide modes that can be transferred to optical fibres with minimal coupling loss due to the similarities in waveguide modal properties (Section 2.2). This and low transmission losses permit silica-based SFWM sources to have good preparation efficiency (80%), speed (3.1×10^5 photons per second) and purity in excess of 90% [129]. The same study remarks that silica sources can operate with a large range of pump wavelengths, and have been shown to maintain highly non-classical correlations between photon-pairs generated from the visible to telecommunications spectral regimes. 3-photon pair interference experiments in SoS DUW waveguides have demonstrated excellent waveguide uniformity, with birefringence variations better than 1×10^{-6}, and low-loss coupling to fibre optic networks (Section 1.2.2).

The experiments to date have been undertaken with the production of photon-pairs in the visible region of the electromagnetic spectrum. Current sources are susceptible to broadband Raman noise and loss-inducing Rayleigh scattering for shorter wavelength photons [130]. Further, it is desirable to operate sources with photon-pairs in the visible (810 nm) and telecommunications (1550 nm) regions to make use of state of the art avalanche photodetectors and low-loss telecommunications fibre networks (Section 1.2.1). The following section will discuss how these shortfalls can be overcome with a platform using high-birefringence DUW SoS waveguides.

5.2 Spontaneous four-wave mixing heralded single-photon sources for telecommunications wavelengths

The section below presents detail of the design considerations and fabrication techniques to develop high-birefringence DUW waveguides for SFWM sources operating in both the visible and the near-infrared (NIR) regions of the electromagnetic spectrum. The fabrication work is supported by classical characterisation methods to assess the suitability of the platform developed.

5.2.1 Waveguide design considerations

The spectral position of the signal and idler photon as a function of pump wavelength can be predicted by the wave-vector mismatch obtained for SFWM processes in cross-polarised birefringent waveguide [131]. For pump wavelengths far from the zero-dispersion wavelength of silica, the material dispersion dominates the total dispersion and the self- and cross-phase modulation terms described in [131] are negligible. The wavevector mismatch Δk is then given by equation (5.1).

$$\Delta k = 2\,\frac{\omega_p}{c}\,n(\omega_p) - \frac{w_s}{c}\,n(\omega_s) - \frac{w_i}{c}\,n(\omega_i) + 2\,\Delta n\,\frac{\omega_p}{c} \qquad \textbf{(5.1)}$$

In equation (5.1), c is the speed of light in a vacuum and Δn is the birefringence of the waveguide. Δk is equal to zero for the phase-matched case. ω_p, ω_s, ω_i are the pump, signal and idler field frequencies respectively. $n(\omega_p)$, $n(\omega_s)$, $n(\omega_i)$ are the refractive indices at the pump, signal and idler frequencies respectively, determined by the fitted Sellmeier coefficients for the respective polarisation axes. The Sellmeier

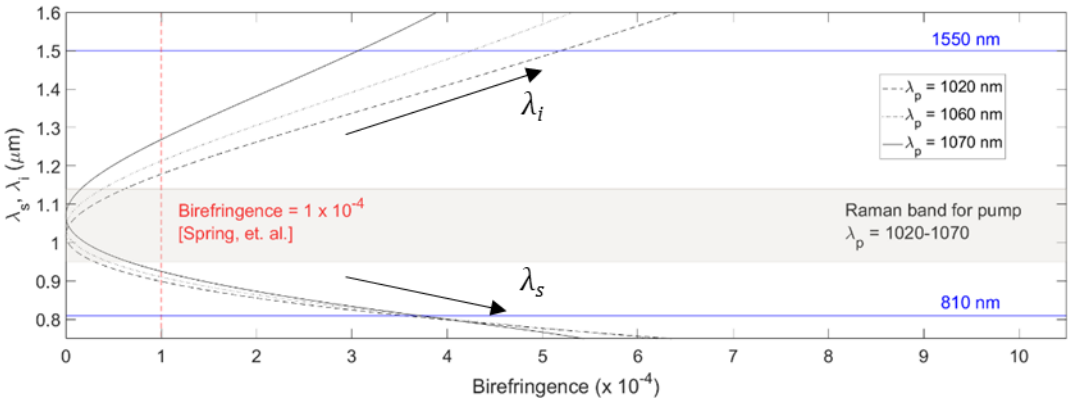

Figure 5.2 – Line plot of the solutions of the wave-vector equation for phase-matched energy conserved case as a function of birefringence at three pump wavelengths between 1020-1070 nm. Each contour line indicates the solution when the wave-vector mismatch is equal to 0 and for each different pump wavelengths a different type of dash is used. The lower and upper sections of the contour lines represent the signal and idler wavelength λ_s and λ_i, respectively.

coefficients for the DUW waveguides fabricated and tested by Spring et al. [30] have been obtained by multi-order interrogation of DUW gratings [88]. The solutions of equation (5.1) as a function of Δn for the phase-matched conditions with energy conservation are shown in Figure 5.2 for three pump wavelengths in the range 1020-1070 nm. Signal and idler fields are generated and detuned from the pump wavelength. In Figure 5.2, the signal wavelength, λ_s, is detuned towards the lower wavelength and the idler wavelength, λ_i, towards higher wavelengths. This wavelength region is convenient to use since a variety of high-power pulsed laser systems are available.

Current DUW SoS waveguides typically have birefringence of $\Delta n = 1\times10^{-4}$. These silica-based sources are susceptible to the broadband cascaded Raman noise from the pump [30], [132]; the range of the noise for pump wavelengths range of 1020-1070 nm is highlighted by the greyed area in Figure 5.2. High-birefringent platforms with birefringence greater than $\Delta n = 1\times10^{-4}$ will reduce filtering needed as a consequence of the limited detuning of signal and idler photons from the pump wavelength [129]. For waveguides with birefringence greater than $\Delta n = 3.5\times10^{-4}$, the platform generates photon-pairs that are in the visible (810 nm) and

telecommunications (1550 nm) spectral regions. The following section describes the routes to achieve this.

5.2.2 Fabrication of high-birefringence wafers

The following section describes adaptation made to the flame hydrolysis deposition (FHD) process to create high-birefringence DUW waveguides. The reader is referred to Chapter 2 for the background on wafer and waveguide fabrication techniques.

5.2.2.1 Background on high-birefringence waveguides

Planar waveguide birefringence is largely caused by the thermal-expansion mismatch between different materials, which leads to anisotropic distribution of the stress [41]. It is well understood that a reduction in the concentration of germanium and boron dopants in silica layers leads to an increase in the glass melting point [46]. Prior work has however concentrated on the reduction of birefringence in waveguides. Whilst FHD-based PICs can be integrated with other processes to obtain high waveguide birefringence, such as metal-doping ($\Delta n = 3.5\times10^{-4}$) or stress applying films ($\Delta n = 5.5\times10^{-4}$) [133], these result in undesirable increased losses and have not been considered in this study.

5.2.2.2 Wafer fabrication and characterisation

The fabrication of new SoS wafers follows the process described in Section 2.3. Slab waveguides are fabricated by the consecutive deposition and consolidation of silicate soot layers. Silicon substrates of thickness ~1 mm and diameter 15 cm were used to fabricate wafers with different core layers varying in boron and germanium composition. The FHD dopant flow rates of germanium tetrachloride ($GeCl_4$) and boron trichloride (BCl_3) relative to those of the wafers used for visible SFWM heralded single-photon sources are shown in Figure 5.3. The original wafer (NB88/90) used to make these chips had $GeCl_4$ and BCl_3 flow rates of 43 sscm and 61 sscm, respectively. Wafers v1, v2 and v3 correspond to wafers NB236, NB231 and NB241, respectively. The corresponding FHD recipes, with exact dopant flow rates, are presented in Appendix C.

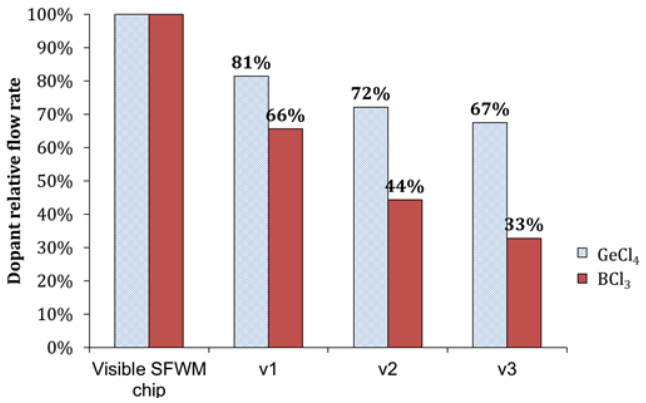

Figure 5.3 – Germanium and boron dopant flow rates relative to their respective flow rates used for the original "Visible SFWM chip" used by Spring et al. for heralded single-photon source arrays in the visible [30].

Each wafer has undergone independent FHD and sintering steps to generate first a germanoborosilicate photo-sensitive core layer, followed by a borophosphosilicate overclad layer. The core layer composition in boron and germanium are controlled by a mass flow controller and a bubbler control system (*SG Controls TD0197*), respectively. The FHD layers were characterized by the prism coupling measurement (Section 2.3.4). The core layers have a refractive index contrast of 0.2% of the cladding and the overclad have a refractive index matched to that of the thermal oxide underclad at 1553 nm.

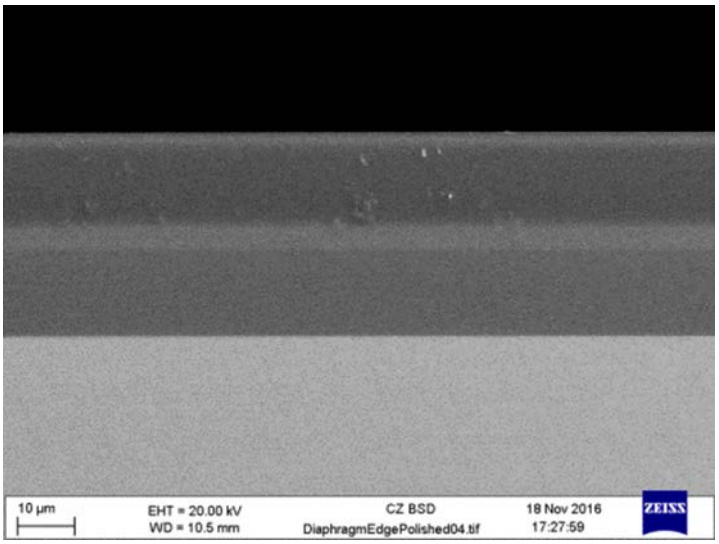

Figure 5.4 – Scanning electron microscope image of end facet of diced chips from wafer NB231. (Image courtesy of A. Jantzen.).

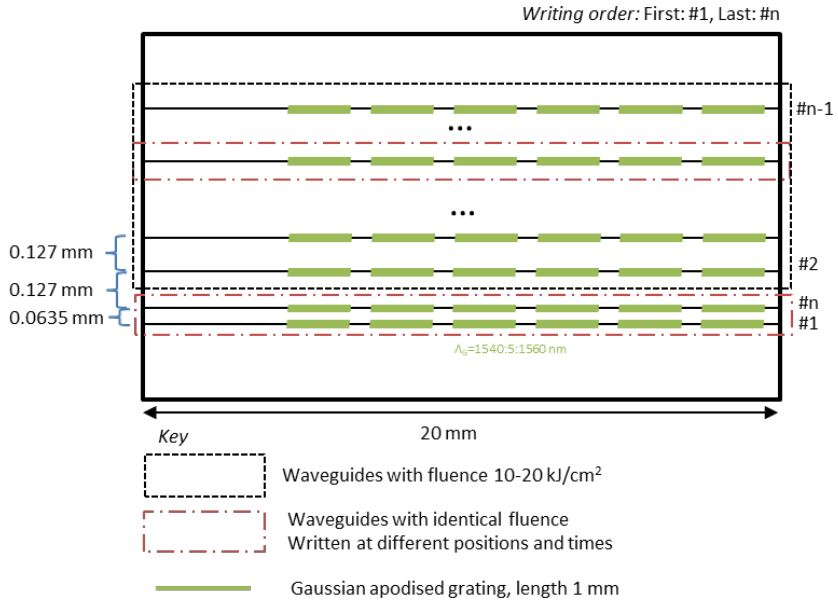

Figure 5.5 – Test chip structure for measuring birefringence as a function of fluence, position on chip and time of writing.

Chips were diced and the end facets were inspected by scanning electron microscopy to inspect layer quality. Figure 5.4 shows clear distinct FHD layers for wafer v2, which is representative of layers in all three fabricated wafers. The chips were hydrogen loaded more than 240 hours to enhance photosensitivity (Section 2.4.1) prior to subsequent DUW processing.

DUW was used to define the waveguides and gratings simultaneously into the photosensitive core layer for chips from each of the 3 new wafers developed. 11 waveguides (length 20 mm) each with 6 diagnostic gratings (length 1 mm) and each separated by a lateral distance of 127 μm were made by DUW on three chips with different core layer composition. 8 waveguides have been written at fluence of 10-20 kJ/cm^2 to study waveguide formation by DUW in chips from each wafer. 3 identical waveguides have also been written to verify birefringence variation as a function of waveguide time of writing and position on the chip. The DUW is sensitive to the outgassing of hydrogen from the chip, so one of the test waveguides has been written adjacent to the first waveguide to study the effect on birefringence with outgassing time. The gratings were used to measure birefringence along the waveguide. The layout of the waveguides on the chip is shown in Figure 5.5.

5.2.3 Grating-based waveguide birefringence characterisation

The waveguides were characterised through interrogation of the gratings' spectral reflection properties using the setup described in Figure 5.6 (a). The radiation signal was an amplified spontaneous emission (ASE) erbium fibre source operating in the C-band (1530-1570 nm). The reflected spectrum was collected through a 50:50 fibre beam-splitter and an optical spectrum analyser (OSA). The polarisation of the launch signal was controlled through a fibre polariser and the launch polarisation (TE, TM) was selected by a ferrule rotator. Figure 5.6 (b) illustrates typical reflected spectra from the Bragg gratings for a waveguide written at a fluence of 12 kJ/cm^2.

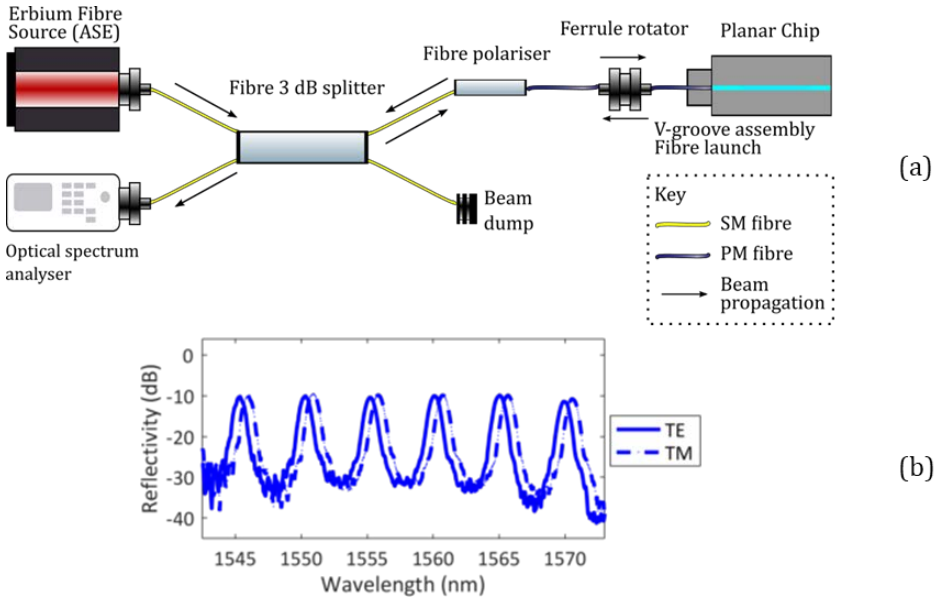

Figure 5.6 – (a) Characterisation setup for interrogation of TE and TM back-reflected radiation from on-chip DUW waveguide-gratings. (b) Representative Bragg grating reflection spectrum for TE and TM mode of fabricated devices.

5.2.3.1 Grating spectra processing

The birefringence is directly obtained by computing the cross-correlation of the TE and TM reflected signals, respectively represented as *f* and *g* in equation (5.2).

$$f \otimes g[n] = \sum_{\lambda=-\infty}^{\infty} f(\lambda) g(\lambda + n) \qquad \textbf{(5.2)}$$

The value of *n* represents the lag of the function, i.e. the displacement between both functions. The wavelength values, λ, are constrained by the sampling window. The signals overlap with a lag of integer-value, n_{max}, which is the lag at which the cross-correlation function is maximal. The wavelength shift, $\Delta\lambda$, is calculated from the OSA measurement resolution, $\delta\lambda$, and is given as a function of the grating period, Λ_G, yielding a birefringence, Δn, given by equation (5.3).

$$\Delta n = \frac{\Delta\lambda}{2\,\Lambda_G} = \frac{n_{max}\,\delta\lambda}{2\,\Lambda_G} \qquad \textbf{(5.3)}$$

The data processing techniques are used in the following section to calculate the birefringence in the fabricated waveguides at the position of each grating.

5.2.3.2 Waveguide birefringence

Figure 5.7 (a) shows the average waveguide birefringence as a function of DUW fluence for each of the three chips. The waveguide birefringence is calculated as the average value of the birefringence measured from the six different gratings. The error bars shown in Figure 5.7 (a) indicate the standard deviation calculated from the six different gratings in each waveguide. Wafer v2, with relative Ge:B doping of 72:44 % of the wafers used in [30], meet the minimal birefringence requirements for SFWM sources operating in the visible and telecommunications spectral regions. It can be seen from the data of wafer v3 that further dopant reduction does not yield higher birefringence, setting an approximate upper bound for the birefringence that can be achieved using this approach. The uniformity of the waveguide birefringence has been measured using waveguides written at a fluence of 12 kJ/cm^2 at different positions and different times on the sample. The waveguide birefringence is $B = 4.5 \pm 0.2 \times 10^{-4}$, as summarised in Figure 5.7 (b).

The wafers developed were found to offer a range of birefringence compatible for heralded single-photon sources operating in the visible and NIR. Two additional waveguide chips from wafer v2 were fabricated by DUW with waveguides at a fluence of 12 kJ/cm^2. Each chip contained three test waveguides with gratings situated on either side of the straight waveguides for local chip characterisation. Each of these test waveguides had 11 Bragg gratings with central wavelengths in the range of 1535-1585 nm, and each grating was spectrally separated by 5 nm. The

birefringence of the chips was measured as $\Delta n = 4.5\times10^{-4}$ and $\Delta n = 4.9\times10^{-5}$ for chips 1 and 2, respectively. Variation of position on the wafer is a likely cause for the variation in birefringence between chips.

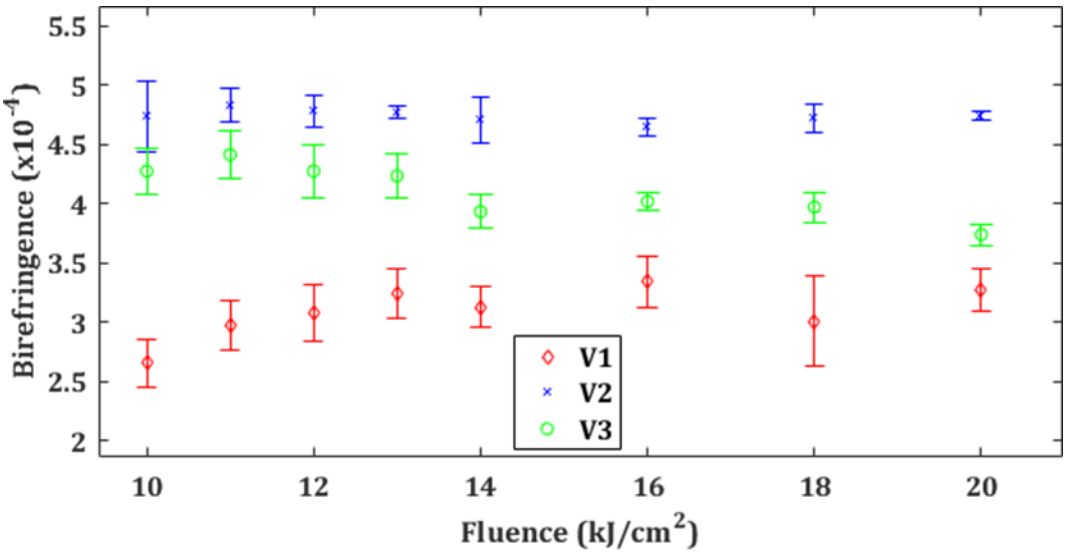

(a)

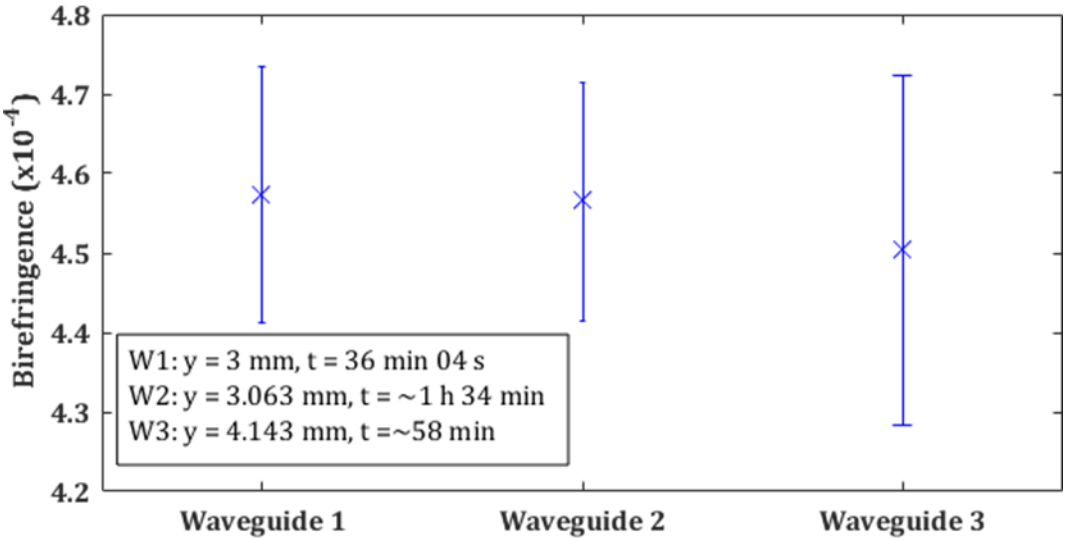

(b)

Figure 5.7 – (a) Waveguide birefringence as a function of fluence for waveguides in three chips with three different material compositions (b) Birefringence of identical test waveguides written at different times and position on chips. For each waveguide, the time indicated is outgassing time and the y-position is position relative to the bottom left hand corner of the chip.

5.2.4 Waveguide optical mode profiling

The following section describes experimental work to measure the waveguide optical mode profiles and determine theoretical waveguide-to-fibre coupling efficiency. The work is intended to support verification of SFWM heralded single-photon source waveguide fabrication. The optical mode profiling apparatus used is described first.

5.2.4.1 Optical mode profiling apparatus

An optical mode profiling apparatus has been developed at the University of Southampton by Rex H. S. Bannerman, which has been used in this study to characterise the mode field diameters (MFD) of waveguide modes.

The equipment's data collection and manipulation procedures are in accordance to standard ISO11124-2 [134]. The source used for the waveguide interrogation is a superluminescent light emitting diode (SLED, Exalos EXS210067-03) mounted in a laser diode driver (Thorlabs CLD1015) operating at a central wavelength of 790 nm and with a bandwidth of 20 nm. The broadband source is used to limit interference effects. The polarisation of the source is controlled by an in-line fibre polariser. For the waveguide characterisation configuration shown in Figure 5.8, the radiation is launched into waveguides by butt-coupling waveguide chips to commercial fibre v-groove assemblies. Fibres are directly connected to the fibre polarisers. The setup shown permits the direct measurement of optical beam widths by second moment analysis to extract of the $1/e^2$ MFD in vertical (y) and horizontal (z) axes (Section 2.2).

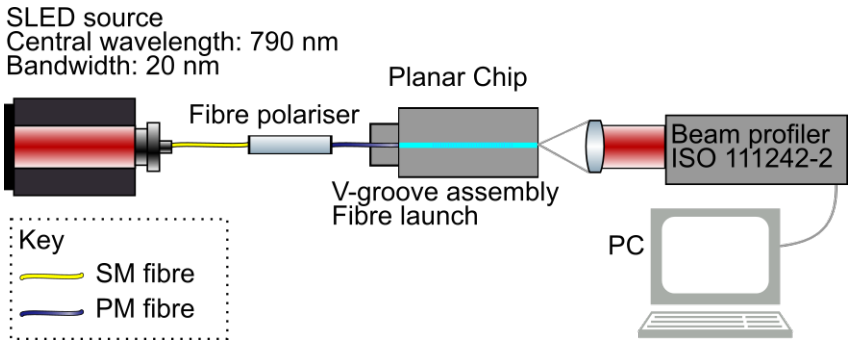

Figure 5.8 – Optical beam profiling setup.

The waveguide MFD for the fabricated chips was measured as 3.61 μm and 3.67 μm in the horizontal and vertical directions, respectively. The waveguide profile has good symmetry. Further measurements taken by Rex Bannerman have been performed for PM fibre (Nufern PM780-XP). The horizontal and vertical MFDs were measured as z = 2.92 μm, y = 2.76 μm. The loss caused by modal mismatch has been calculated as 0.19 dB and 0.35 dB in the horizontal and vertical axes (Section 2.2.2).

5.2.4.2 Numerical modelling of waveguides

The measured parameters have been used to develop a waveguide geometry in the numerical mode solver package FIMMWAVE (Section 2.2.3). The model has been simulated with an excitation wavelength of 790 nm to obtain the mode field profiles. In the absence of adequate detectors to measure optical mode profiles at the pump and idler wavelengths, the same waveguide geometries were used to simulate the waveguide mode profiles using excitation wavelengths at 1060 nm and 1550 nm. For each geometry considered, the fundamental mode was selected. PM fibre geometries have also been developed in FIMMWAVE for existing PM fibre technologies. The extracted electric field parameters for the fundamental mode have been used to measure the fibre to waveguide coupling ratio, which is described next. The simulated waveguide modes at 790 nm and 1550 nm are presented in Figure 5.9 (a) and (b), respectively.

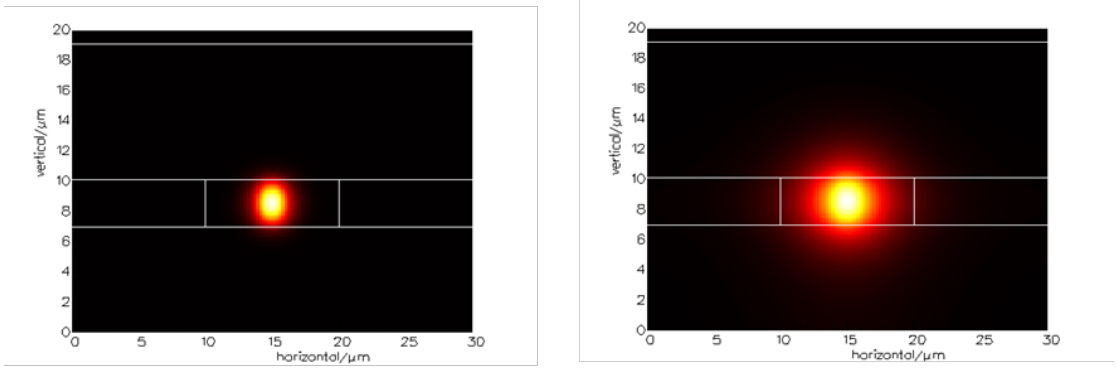

Figure 5.9 – Numerical modelling of waveguide fundamental modes with the same geometry (a) Excitation at 790 nm (b) Excitation at 1550 nm.

5.2.4.3 Fibre-to-waveguide coupling

The power distribution of the fundamental modes for waveguides and fibres have been used to establish the theoretical fibre-to-waveguide coupling. The fractional power coupled between the fundamental mode of two Gaussian beams is given by [34]

$$T = \left| \int_{-\infty}^{+\infty} \int_{-\infty}^{+\infty} \psi_1 \psi_2^* \, dxdy \right|^2 \qquad \textbf{(5.4)}$$

The modelled field parameters for the waveguide and fibre modes are not defined in terms of Gaussian beams and require solving the integration of equation (5.4) numerically. A Gaussian quadrature permits the numerical estimate of this integral. The integral evaluation is based on the Gauss-Kronrod implementation described in [135] and the source code was provided by Dr. James C. Gates. The source code for the computation of the fibre-to-waveguide coupling efficiency was provided by Paolo L. Mennea. The theoretical mode fibre-to-waveguide coupling at 1550 nm was 67%. Simulated waveguide-to-fibre coupling at 790 nm was 80% and 91% at 1060 nm. The implications of these findings in the context of the development of high-birefringence SFWM heralded single-photon sources is discussed next.

5.2.5 Preliminary discussion

The section above has described the development of FHD wafers compatible with DUW for the generation of high-birefringence waveguides. The findings have shown DUW waveguides with birefringence higher than previously reported and that permit the generation of heralded single-photon sources in the visible and telecommunications spectra regions. These results have been presented in [136].

Test chips have been sent to collaborators from the University of Oxford's Ultrafast Quantum Optics and Optical Metrology research group for further investigation. Experiments have been conducted by Thomas Hiemstra and collaborators to classically assess the suitability of this platform for heralded single-photon sources through seeded joint spectral intensity measurements [137], [138]. Preliminary results show that local chip birefringence can be compensated by tuning the pump

wavelength to obtain signal-idler signals in the desired telecommunications and visible spectral regions.

The wafers described above were designed for waveguides capable of supporting single mode operation at the wavelengths of the pump (1060 nm), signal (800 nm) and idler (1550 nm). This requirement has resulted in a limited experimental coupling efficiency of the idler field, which was measured at 65%. The coupling efficiency is in good agreement with the simulation results presented above.

The limited coupling efficiency at the idler wavelength is detrimental to source operation, which ultimately will limit scalability. The high-birefringence platform needs to be adapted for optimal fibre-to-waveguide coupling at idler wavelengths around 1550 nm. To this end, three new wafers with different core thicknesses and based on the material composition of wafer NB231 have been fabricated. The production parameters for wafers NB284, NB285 and NB286 are presented in Appendix C. At the time of writing, no conclusive grating-based evidence can be reported due to ongoing technical difficulties with the DUW system.

A long-term ambition of this technology is to enable the scaling of the complexity of the QIP experiments through the integration of multiple sources of identical heralded single-photons on chips. A number of technical requirements are needed to achieve this goal and the following section presents technical work undertaken to this end.

5.3 Towards on-chip heralded 4-photon pairs sources

The DUW silica-on-silicon platform has demonstrated its suitability as a platform for integration of identical heralded single-photon sources on chip in the visible [30]. The simultaneous excitation of three waveguides has been achieved by free-space launch. Bulk optics setups ultimately limit the scalability of QIP experiments. Further scaling would require the excitation of more waveguide modes simultaneously with a single pump. This section presents the development of a modular architecture to scale the complexity of the experiments.

5.3.1 Architecture

This section describes the architecture required for the generation of four pairs of heralded single-photons. A pump laser is launched into the input of a 1×4 splitter chip, which splits the beam equally. The output of the splitter chip is connected to a source chip, where the waveguide-based SFWM occurs across the waveguide array. The architecture relies on both the splitter and source chips to have well-matched modal properties, for good coupling efficiency, and different birefringence, for the phase-matching conditions to be only permitted on the source chip. Compact 50:50 splitters have been developed with DUW SoS [59], and the implementation of these structures is left as an area of future work.

The low $\chi^{(3)}$ of silica requires pumping with a high-average power pump laser. The maximal optical power that can be launched onto chip is set by the silica damage threshold; this has been experimentally shown to be about 150 mW at the air-silica interface and has been reached in current experiments [130]. One strategy to overcome this limit is to enlarge the surface area of the incoming beam at the air-glass interface. Fibre technologies use coreless endcaps on end facets that allow a larger beam size at the air-silica interface [139], [140]. Typical end facets of DUW SoS chips are 10×1 mm, which is a much larger surface than for their fibre counterparts. An endcap application process compatible with this platform is required.

This section will present the development of a fabrication process for the integration of endcaps with this platform to permit further integration with integrated splitter-

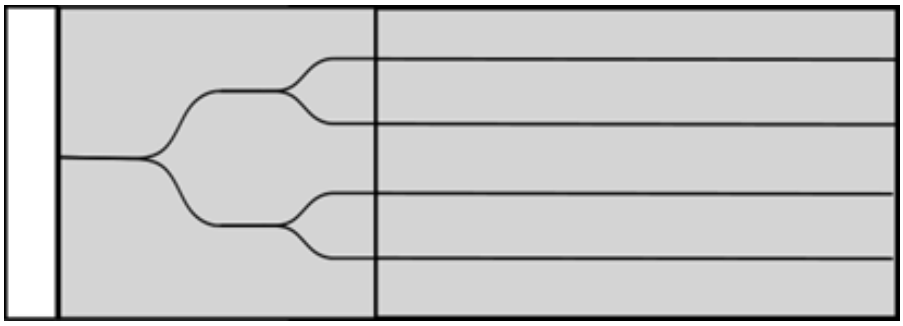

Figure 5.10 – Integrated splitter and SFWM birefringent source chips with coreless endcap on end (left).

source chips. The architecture of the SFWM heralded single-photons source array shown in Figure 5.10 could be scaled further in future work.

5.3.2 Endcaps for high power management

The following sub-section will detail experimental work into the development of endcaps for SoS planar chips. A primary requirement for endcaps is to be index-matched to the silicate layers deposited by FHD, with the intention of minimising Fresnel back-reflection from refractive index discontinuities. As a reminder, the refractive indices of the upper and lower claddings are typically n = 1.4480, with a refractive index contrast of 0.2-0.3% for the core layer.

5.3.2.1 Thermal bonding of endcaps with FHD soot

Chapter 2 described how the sintering of FHD soot resulted in uniform silicate layers. This concept was extended to study if the FHD soot could be used as bonding agent between optical windows and chips. A requirement for this process is to use soot that sinters at lower temperatures to avoid reflowing of the FHD layers. FHD germania and phosphogermanate soot with lower sintering temperatures have been used. The soot has been developed in the ORC in parallel to this work by Miranda Turvey. Quartz (microscope) slides, which are index-matched to SoS planar chips and have high melting temperatures, were used.

Layers of germania and phosphogermanate soot were placed on one bare silicon wafer and one silicon wafer with a thin thermal oxide. Quartz windows were placed on top of the soot on each wafer. A quartz slide without underlying soot was also mounted on both wafers to act as a reference. FHD chips with an upper cladding were also placed on each wafer to control whether bonding occurred at the maximal temperature tested. An example test wafer before thermal processing is pictured in Figure 5.11 (a). The wafers were inserted into a furnace (*Severn Thermal Solutions SP2030*) and the temperature was controlled according to the temperature ramp profile shown in Figure 5.11 (b). The maximum temperature, T_{Max}, was iteratively increased in this experimental investigation, from a starting temperature of 950°C and in steps of 50°C.

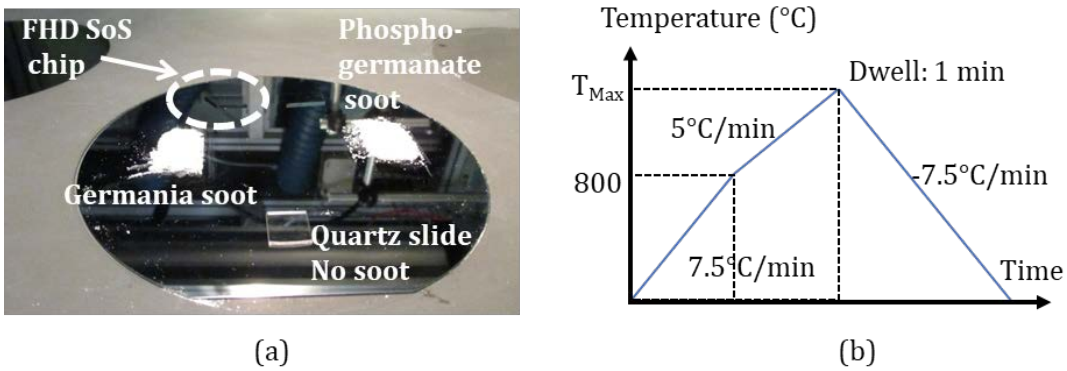

Figure 5.11 – (a) Test silicon wafer, before heat treatment, with quartz slides placed on FHD soot to investigate thermal bonding through soot sintering. A quartz slide and an FHD SoS chip (inside white ellipse) are used as control chips. (b) Temperature ramp profile of furnace for thermal processing.

No modification of the soot was observed for $T_{Max} < 1050°C$. At $T_{Max} = 1050°C$, germania soot started to crystallise and form patches – see Figure 5.12 (a). At $T_{Max} = 1100°C$, the effect was more pronounced. At $T_{Max} = 1150°C$, cracks were observed on both the bare silicon and thermal oxide silicon wafer originating from the junction area between the wafers and the quartz windows on top of germania soot – see Figure 5.12 (b) and (c) respectively. No cracks were observed at the junction between the quartz window and the wafers where no soot was present. Furthermore, no bonding between the silicon wafer and the control chips placed upon it was observed, nor were there any structural modification of the chips (rounding of edges, cracking). The observations indicate that the sintering of the soot has caused the window and wafer to bond temporally.

The cracking can be explained by considering the thermal expansion coefficient of the systems interacting. The thermal expansion of silicon is $2.55\text{-}4.56\times10^{-6}$ K^{-1} from room temperature to 1500 K [40]. The thermal expansion of commercially available quartz windows with high melting temperature can be 2-3 times greater. The mismatch in linear thermal expansion coefficient leads to unequal stresses during the cooling process and subsequent cracking of the chips.

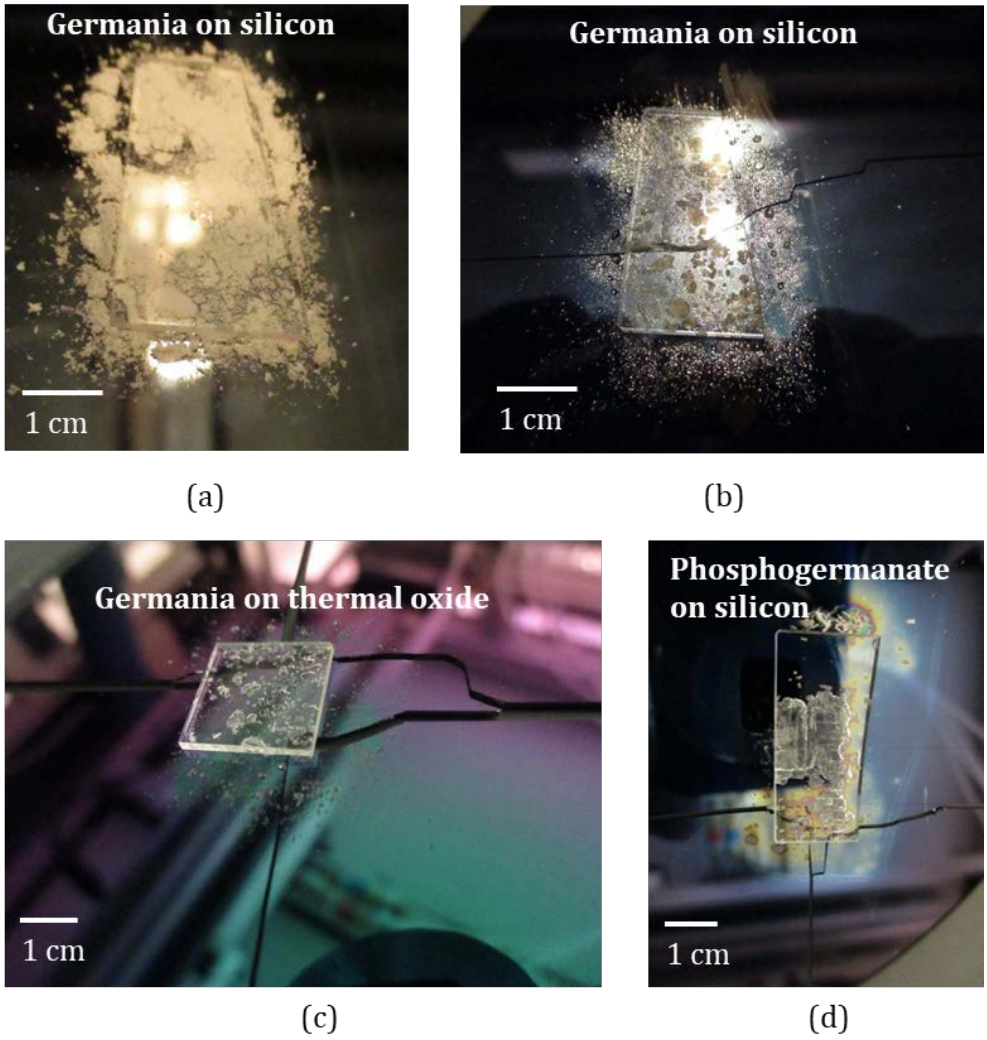

Figure 5.12 – Experimentation of bonding of quartz windows onto wafers with FHD soot (a) $T_{Max} = 1050°C$: formation of crystallised patches of FHD germania soot. (b) $T_{Max} = 1150°C$: formation of cracks at junction between quartz slide and thermal oxide wafer with the presence of FHD germania soot. (c) $T_{Max} = 1150°C$: formation of cracks at junction between quartz slide and thermal oxide wafer with the presence of FHD germania soot. (d) $T_{Max} = 1200°C$: formation of cracks junction between quartz slide and thermal oxide wafer with the presence of FHD phosphogermanate soot.

The experiment was continued with the phosphogermanate soot. At $T_{Max} = 1200°C$, cracking was observed on the bare silicon wafer, along with clear crystallisation of the soot – see Figure 5.12 (d). Again, no cracks were observed at the junction between the quartz window and the wafers where no soot was present. The linear thermal expansion coefficient of the thermal oxides on silicon wafers is not known precisely. Fused silica typically has linear thermal expansion coefficients of 0.40-0.55×10^{-6} K^{-1} [39]. Thermal oxide growth happens through the oxidisation of silicon [42] and it is likely that these thermal oxide layers have a linear expansion coefficient between that of fused silica and silicon. The FHD soot does not permit the bonding between glasses with different thermal expansion coefficients, and the observations motivate the need to assemble endcaps with chips using materials of similar linear thermal expansion coefficient.

5.3.2.2 Thermal bonding of endcaps by wetting

The use of silica windows with a linear thermal expansion coefficient closer to that of silicon was investigated. Low expansion borosilicate glass (LEBG, Comar Optics) was selected for its linear thermal expansion coefficient of 3.2×10^{-6} K^{-1} and refractive index (n=1.472), which are near to the SoS silica layers. The furnace was operated between the quoted LEBG maximum operating temperature (500°C) and the melting temperature of the FHD silica layers. The LEBG window is expected to transition to a liquid phase, wetting the contact layer, and forming a bond upon returning to a solid phase during furnace cool down.

LEBG windows were diced into endcap strips of 10×1×1.3 mm (length × width × height); the strip height was greater than the chip thickness (~1.1 mm) to ensure that the entire end facet was in contact with the LEBG. Both contact layers were wiped clean with a cotton bud with acetone, followed by a rinse with by DI water. The chip and endcap were mounted on a custom jig made of a ceramic material (Macor ®) capable of operating above the maximum operating temperature of the LEBG. The jig was angled at 45° to permit the chips to push down on to the endcap. The mounted chip and endcap were placed on a support wafer – see Figure 5.13 (a) – and placed in the furnace. The temperature ramp profile was identical to that of Figure 5.11 (b) and T_{Max} = 850°C.

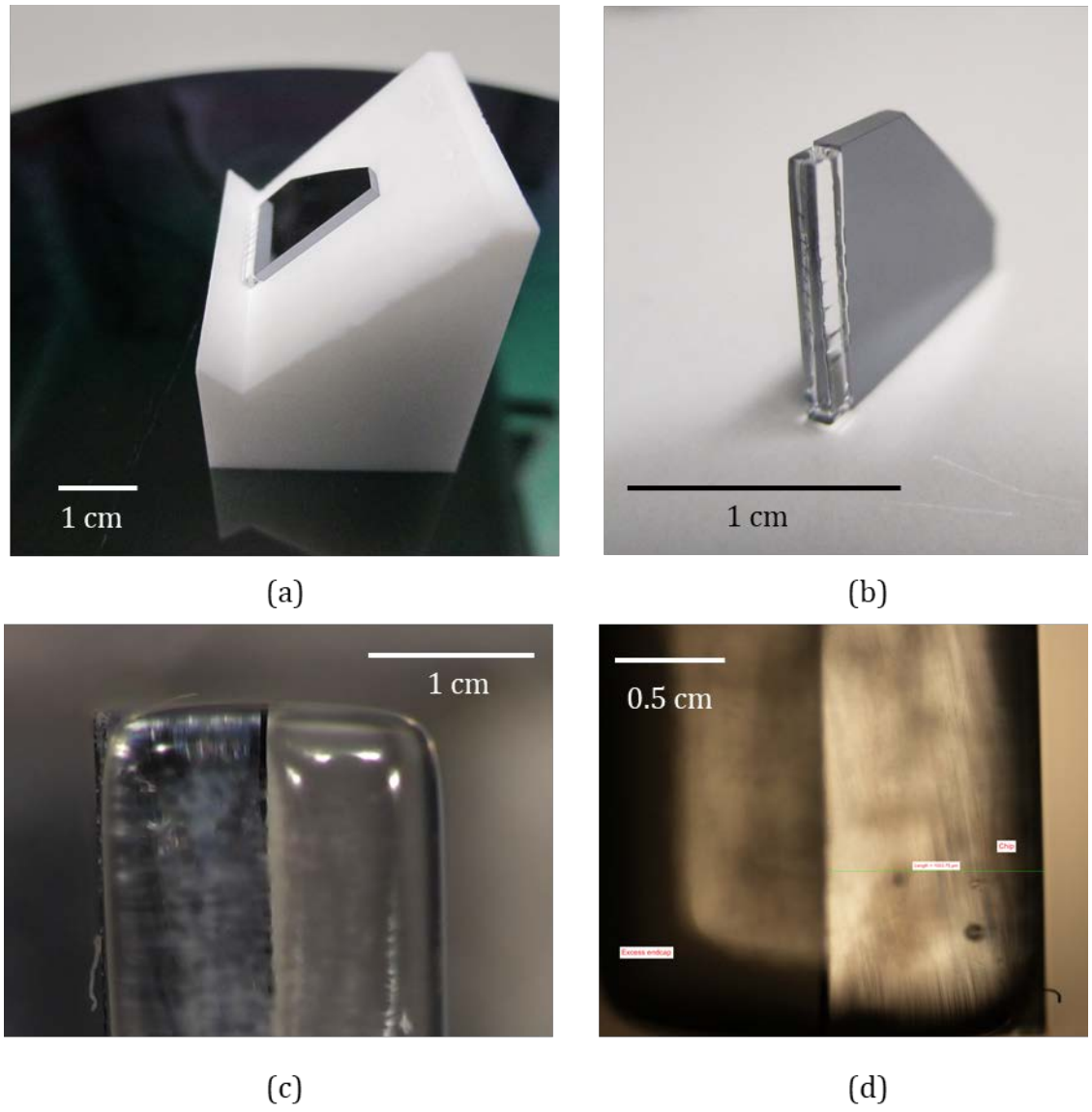

Figure 5.13 – (a) Chip and endcap mounted on Macor ® jig prior to thermal processing. (b) SoS chip with thermally bonded endcap. (c) Endcap inspection under optical microscope showing the rounding of the edges of the endcap. (d) Optical microscope image of the chip-endcap interface, revealing no cracks or air bubbles from thermal processing.

Successful bonds between the LEBG and the end facet of the chip were observed. A typical device is shown in Figure 5.13 (b). The edges of the LEBG endcaps have rounded off – see Figure 5.13 (c) – during the thermal processing, which may be as a result of operating the furnace above the quoted maximum operating temperature of the glass. The SoS chips were not rounded off. The interface between the LEBG and chip has been inspected under an optical microscope (Nikon Eclispe LV100) and

no cracking or air bubble formation at the interface was observed – Figure 5.13 (d). No refractive index discontinuities could be measured through inspection by white light interferometry microscopy (ZeScope), confirming that there has not been the formation of air bubbles, cracks, etc. during the thermal process.

5.3.2.3 LEBG endcap processing

Optical quality end facets are necessary for the launch of high-power free space optical beams used for the source schemes described in this chapter. The following pages describe processes for polishing and cleaning of end facets of endcaps that have been developed by the author.

The endcap lapping and chemical-mechanical polishing process was developed using the *MultiPrep™* (*Allied High Tech*) equipment described in Section 2.7. The system uses lapping sheets of different grit type and size, permitting rapid testing and verification of procedures. At each stage, it is desirable to remove three times the amount of material compared to the previous grit size. Silicon carbide grits were found to remove significant amounts of material for grit sizes greater than 15 µm. They were found to leave scratching on the top surface of the chip end facets. For smaller grit sizes, the removal rate was below the typical desired amount and no improvement of the end facet was noted. Using aluminium oxide grit sheets did not

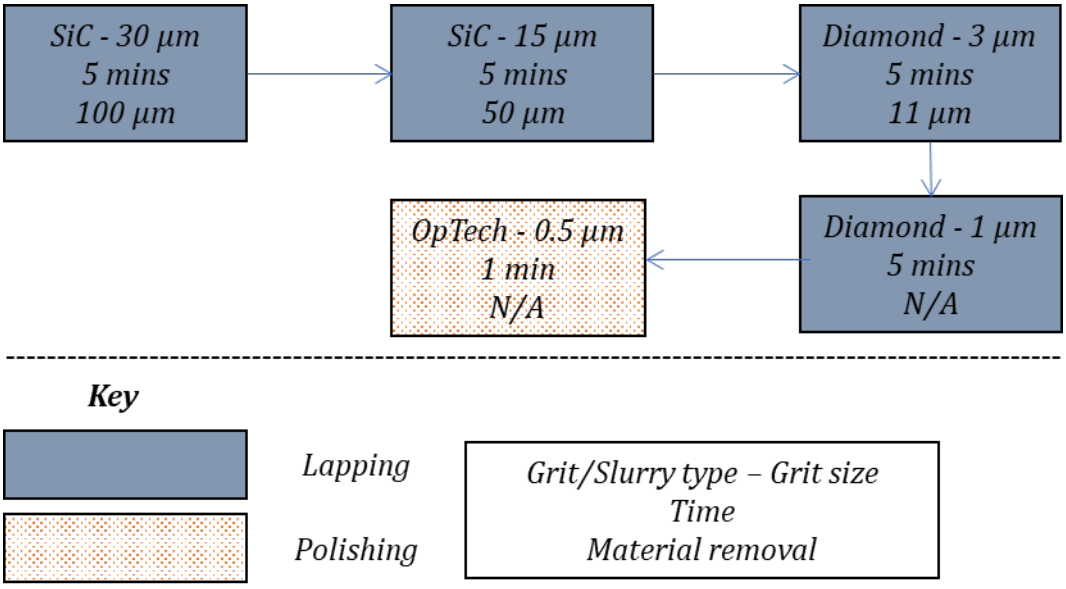

Figure 5.14 – Developed LEBG endcap lapping and polishing process flow.

result in further removal of material, nor did it improve the quality of the surface. Sheets with 3 µm diamond grit were found to have both adequate material removal and to improve the end quality of the end facets. Lapping with 1 µm diamond grits did not remove material, but did result in an observable improvement of the scratching observed. Smaller grit size did not yield observable improvement to scratching. The final polishing step was performed using a 0.5 µm grit slurry (OpTech 9018800). The final developed process flow is summarised in Figure 5.14.

The end facets' surface roughness was characterised by white light interferometry microscopy (Section 2.7.1) at 3 areas across the sample close to the core layer – see Figure 5.15. The RMS surface roughness measurements (S_q) was better than 2.7 nm. Some residual dirt was noted, and a cleaning process was developed as a result.

A test chip underwent 2 successive ultrasonic baths (~10 mins each) in solvents (acetone, IPA), followed by a bath in DI water and rinsing in DI water. No deterioration of bond quality was noted by microscope and white light interferometry techniques. Surface cleaning by the application of solvents with cotton buds was also possible without detrimental effects to the endcap-chip structures.

Test chips have been placed in a hydrogen cell at a pressure of 120 bar to test compatibility with hydrogen loading needed to enhance photosensitivity for DUW.

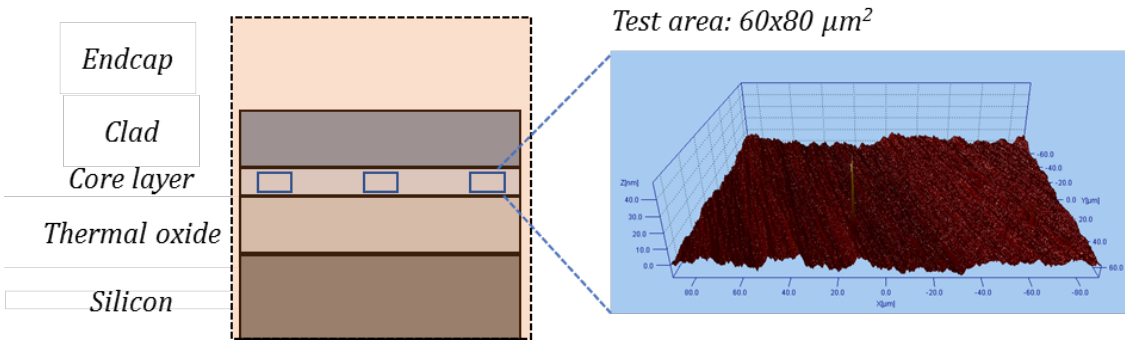

Figure 5.15 – Schematic of endcap overlaid onto SoS chip, indicating areas of scans to determine surface roughness measurement at air-endcap interface. The layer thicknesses are not to scale. Shown on the right is a typical surface roughness profile for a 60x80 µm² area.

The endcaps withheld this process step and no deterioration was noted. After hydrogen loading, standard chips are usually placed in liquid nitrogen to reduce the rate of hydrogen outgassing (Section 2.4.1. The endcaps did not survive this step, and therefore chips with endcaps must go through the DUW step immediately after removal from the hydrogen cell. This is likely due to the small thermal expansion mismatch and possibly the large difference in thermal conductivity.

5.4 Discussion and further work

This chapter has demonstrated the suitability of the SoS fabrication process to fabricate high-birefringence waveguides by DUW for potential applications in quantum science experiments, such as SFWM heralded single-photon sources operating in the visible and NIR. Grating-based characterisation has been used as a verification tool for chips to be integrated into QIP experiments. Chip-to-chip variation of the birefringence has been observed. The development of the FHD process to optimise layer uniformity, and hence birefringence uniformity, would be required for further scaling and connectivity between different chips. Seeded JSI experiments have shown that compensation of wafer level-variation of birefringence is possible by tuning the pump wavelength. Work is underway to develop a high-birefringence platform for optimal fibre-to-waveguide coupling at idler wavelengths around 1550 nm.

This chapter has reported the development of a process for the application of endcaps to permit high power handling in silica. The process is compatible with polishing and cleaning steps of the platform presented in Chapter 2. Thermal processing can be a time consuming and costly process, however alternative endcap processing techniques could be investigated, such as sodium silicate bonding which is suitable for large surface areas [141]. It has recently been shown that it is possible for consolidation of FHD silica soot using 9.3 μm CO_2 laser [142]. The technique could be employed for the assembly of a wider variety of coreless endcaps, without the need for thermal processing.

The architecture requires further integration with components available in the DUW library. Low loss cross-couplers operating across a wide range of pump wavelengths may be useful for the scaling of QIP experiments for fabrication of arrays of identical

heralded single-photons. DUW tilted gratings structures presented in Chapter 3 may be employed as preliminary on-chip pump suppression of Raman noise, reducing the filtering requirements off-chip.

One prerequisite to this technology is optimal coupling between waveguide circuits and fibre networks, and to this end optical beam profiling apparatus operating across a wide range of wavelengths is being developed as a design verification tool. Low-loss connectivity with fibre networks is critical and this topic forms the subject of the following chapter.

Chapter 6 Interfacing modular components for large scale quantum networks

Photonic interlinks are well regarded as tools to connect modular building blocks for quantum information processing (QIP) networks for a vast array of different technology implementations [143]. Silica optical fibres are an obvious candidate for a low-loss interface with direct-UV written (DUW) waveguide-based modules (Chapter 1). The DUW waveguide packing density can be readily matched to commercial fibre v-groove arrays – see Figure 6.1 – thus overcoming bulky free space optics and permitting the integration and scaling of the network functionality. Insertion losses remain a critical part in the scaling process. This chapter concerns itself in the study of v-groove assemblies and the implications of their stated tolerance fabrications on coupling loss.

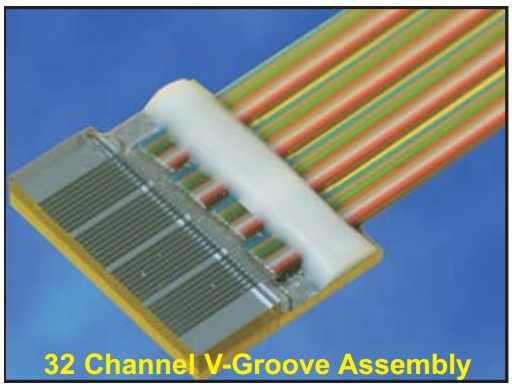

Figure 6.1 – Photo of 32 channel v-groove assembly (www.amstechnologies.com).

6.1 Motivation: minimising interface losses

One of the important characteristics of fibre arrays mounted in v-groove assemblies is their alignment accuracy, errors in which will cause transverse misalignment loss. When coupling between two single-mode (SM) fibres with identical mode field diameter (MFD), ω, and assuming a perfectly matched Gaussian mode, the loss, α, caused by an offset, u, is given by equation (6.1) [34].

$$\alpha\ (dB) = 4.34 \left(\frac{u}{\omega}\right)^2 \qquad \textbf{(6.1)}$$

As illustrated in Figure 6.2, SM fibres with a smaller MFD have considerably more misalignment loss for a given offset position caused by fabrication tolerance. A commercial 16-port device from OzOptics will typically have a stated ±0.5 μm tolerance in the position of each port; the worse possible scenario for multi-port arrays are insertion losses of 0.14 dB (3.2%) for 800 nm SM fibre (SMF-800) and 0.04 dB (0.9%) for 1550 nm SM fibre (SMF-28). However, the tolerance does not specify the exact position of the fibre in each port. Precise knowledge of these may inform on the need to develop "adapter" chips between v-groove assemblies and waveguide arrays to minimise coupling losses, especially at shorter wavelengths. The following sections present experimental investigation of the properties of fibre v-groove assemblies with operating wavelengths near 1550 nm and 800 nm.

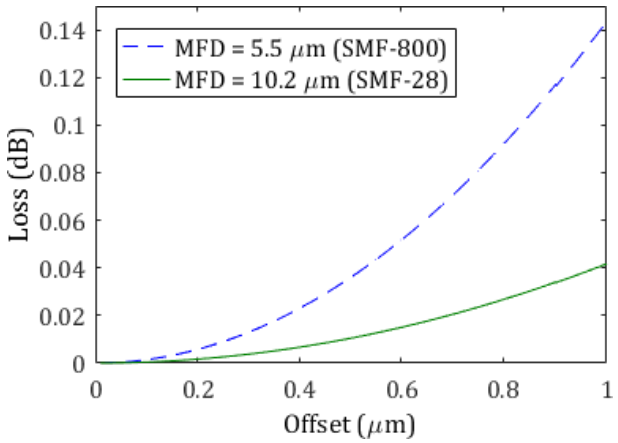

Figure 6.2 – Losses caused by misalignment between two identical single mode fibres with operating wavelengths near 800 nm and 1550 nm.

6.2 Experimental setup

This section describes the development and implementation of a characterisation setup for studying the position of fibres in v-groove arrays – see Figure 6.3 (a). A list of devices tested and their provenance is provided in Appendix D.

The fibre-to-fibre imaging system was comprised of a matched aspheric lens pair (Thorlabs C220MP) mounted in an internally threaded lens tube. The launch fibre has been mounted into a fibre holder. Spacers have been inserted inside the lens tube to correctly set the fibre at the focal point of the aspheric lens pair. A v-groove fibre array has been mounted vertically on to a fibre array holder (Thorlabs HFA001) that has been fixed to an ultra-high precision air-bearing stage system (Aerotech™ ABL 9000). The output fibre was connected to a InGaAs photodetector (Thorlabs PDF10). The output voltage was read through the stage's control system analogue input and processed with a PC. Two separate imaging systems have been

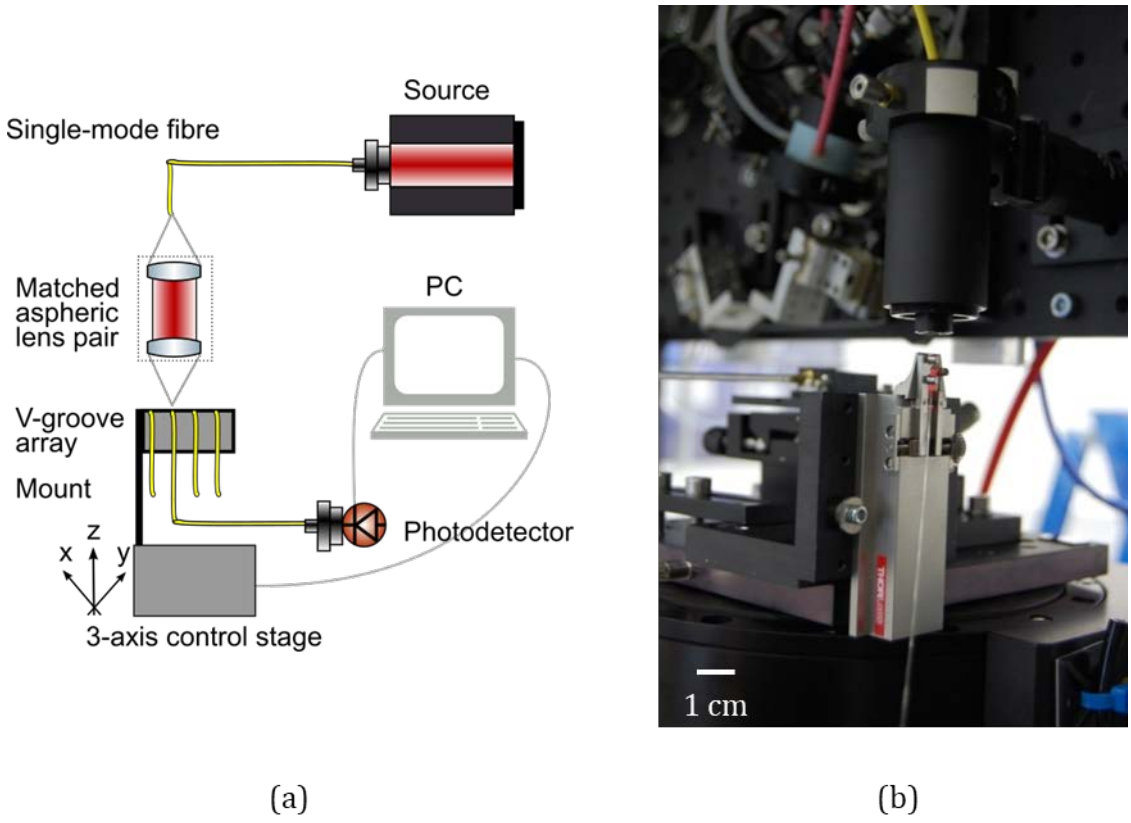

Figure 6.3 – (a) V-groove array characterisation setup. (b) Photograph of the imaging system. The matched aspheric pair and launch fibre holder are mounted in a threaded lens tube.

built for use with SM fibre at wavelengths near 1550 nm and 800 nm. Each optical setup has used a matched aspheric lens pairs with antireflection coating at the appropriate wavelength.

6.3 Data collection and processing

The outermost fibre of the v-groove array was designated as a reference fibre. The coupling between the reference fibre and the launch fibre was optimised manually prior to data collection. Subsequent processing has been automated using the stage system control software. The data collection and processing procedure has been highlighted in Figure 6.4. Individual scans of each port have been taken. A square grid of m^2 pixels is produced, where *m = scan size (μm) / step size* (*μm*). The photodetector voltage has been mapped to each stage position on the grid – see Figure 6.4 (a). The stage has been moved automatically from port to port based on the v-groove specification (typical fibre separations are 127 μm or 250 μm) and the measurement has been repeated for each fibre in the array – see Figure 6.4 (b). A human operator must manually change the fibre connected to the photodetector between each port measurement.

The data collected has been processed in Matlab using the curve fitting toolbox. The fibre modes are assumed to be two-dimensional Gaussians, for which the analytical expression is given by equation (6.2).

$$f(x,y) = A\ exp\left(-\left[\frac{(x-x_0)^2}{\omega_x^2} + \frac{(y-y_0)^2}{\omega_y^2}\right]\right) \qquad \textbf{(6.2)}$$

In equation (6.2), *A* is the amplitude, x_0 and y_0 are the central coordinates of the two-dimensional Gaussian function, and the spot sizes in the x and y direction have been designated by ω_x and ω_y, respectively. Equation (6.2) has been used to fit the data with the intention of locating the centres (x_0, y_0) of the fibres on each port – see Figure 6.4 (c).

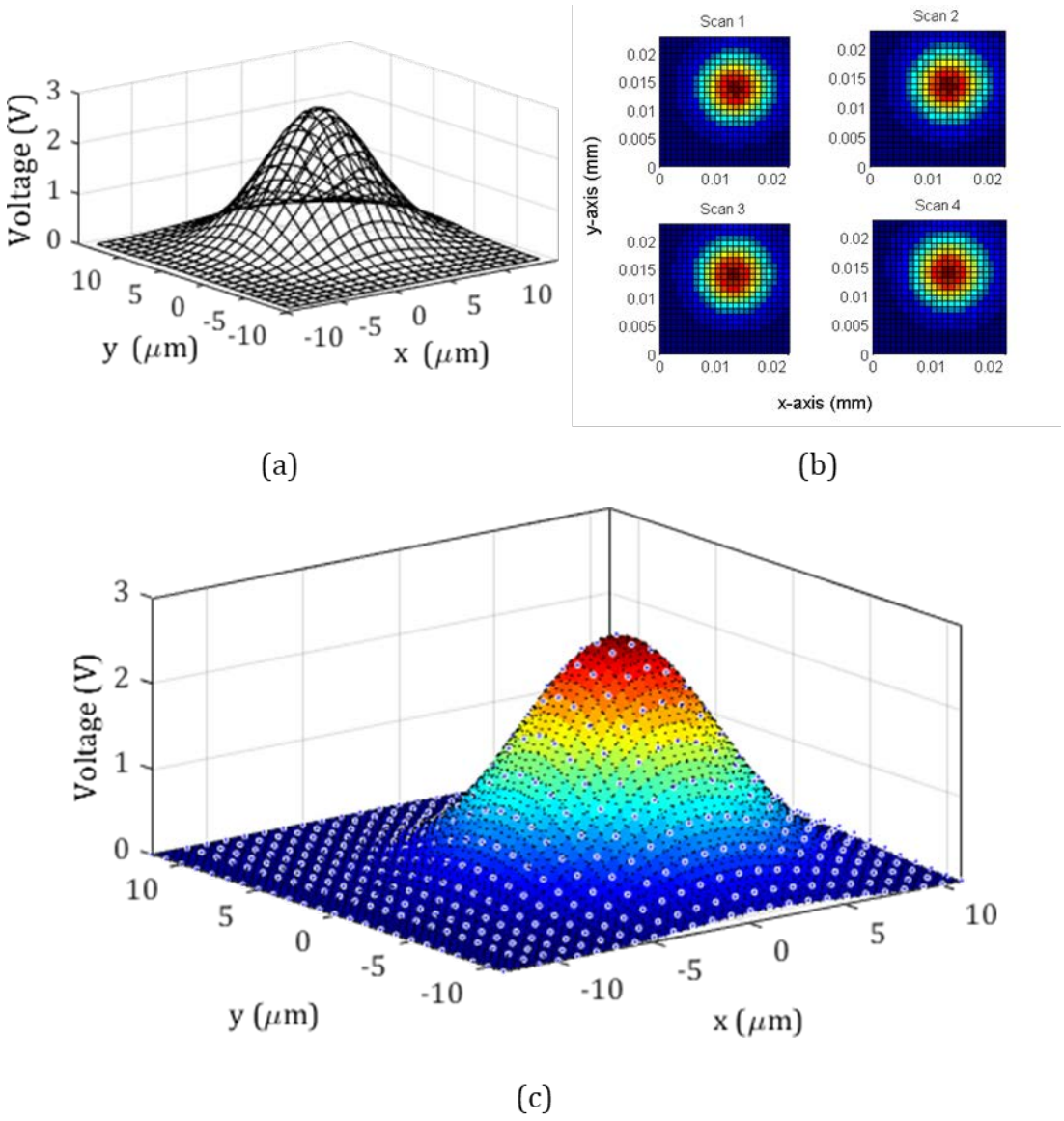

Figure 6.4 – Summary of the data processing scheme. (a) Voltage spatial distribution for unique scan. (b) Multiple checkerboard intensity plots of successive fibre scans. (c) Contour plot of data fitted to a 2D-Gaussian. Raw data is indicated by dots.

6.4 Measurement system calibration

The initial investigation of the v-grooves has highlighted a drift in the central points (x_0, y_0) over repeated scans. This observation has motivated further investigation into the characteristics of the measurement system; multiple scans of the same port were taken for the following scan parameters:

- Grids ($m \times m$ µm^2): m = 35, 24, 12, 8, 6, 4.
- Step size: 1 µm.
- Number of repeated scans: 10.

The drift coefficients in both axes were quantified linearly and the standard error of the repeated measurement was calculated. Smaller scans exhibited a smaller drift and a smaller standard error – see Figure 6.5.

During further investigation into the system's resolution, the dataset obtained from using the 24×24 µm^2 grid was reduced by a scaling factor. Results show that the linear drift and standard error of the binned data clutter in a region close to the original dataset, but have not been reduced to the standard error. Linear drift characteristics of the datasets have been plotted in Figure 6.5. From this investigation, a grid size offering the largest scan area with negligible linear drift was selected.

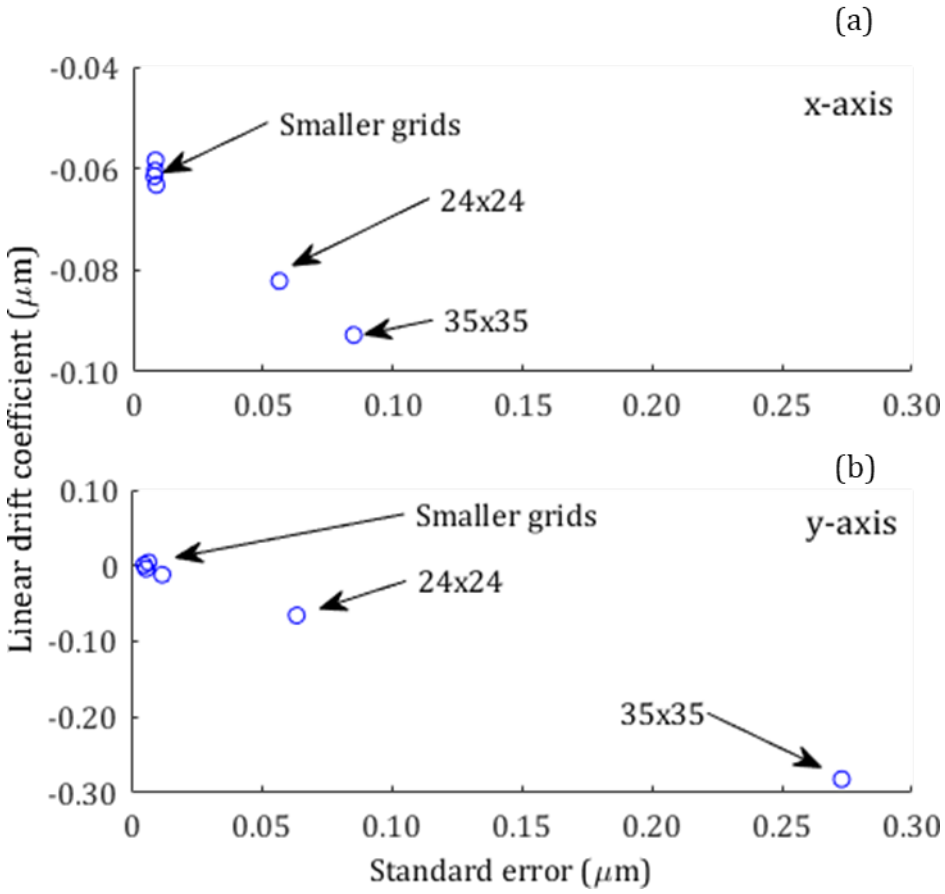

Figure 6.5 – Calculated linear drift with respect to standard error. Grid size $m \times m$ is in µm^2 (a) x-axis (b) y-axis.

The drift in the measurement system has been attributed to the imaging system itself: expansion of the stages with heat fluctuations may explain the errors measured in the x and y direction. The scan area has been reduced to 15×15 μm^2 with a step size of 1 μm based on these observations. For each device tested, successive identical measurements of a single port have been performed to quantify the drift in the system. The typical drift values have been measured as 5-10 nm per scan, which has provided a lower limit for the measurement uncertainty. The scan of the first waveguide has been repeated at the end of experiment to give an indication of drift error throughout the experiment. The misalignment error caused by drift has been used to characterise the error of the measurement system.

6.5 Characterisation of commercial v-groove assemblies

Figure 6.6 illustrates how the vertical and horizontal offsets have been calculated for a 4-port device. For each device scanned, the data collected has been fitted linearly to account for the lateral tilt of the mount. The offset in each axis has been defined with respect to an ideal device. The horizontal position of the leftmost fibre has been taken as the reference. The horizontal (x-axis) deviation for successive fibres has been measured as the offset from ideal fibre centres offset from the reference fibre. The vertical (y-axis) deviation from the "ideal line" defines the vertical offset. The total radial offset can be inferred from the offset of each individual axis. The corresponding losses due to misalignment have been calculated using equation (6.1). The technique has been used to measure the spatial positioning

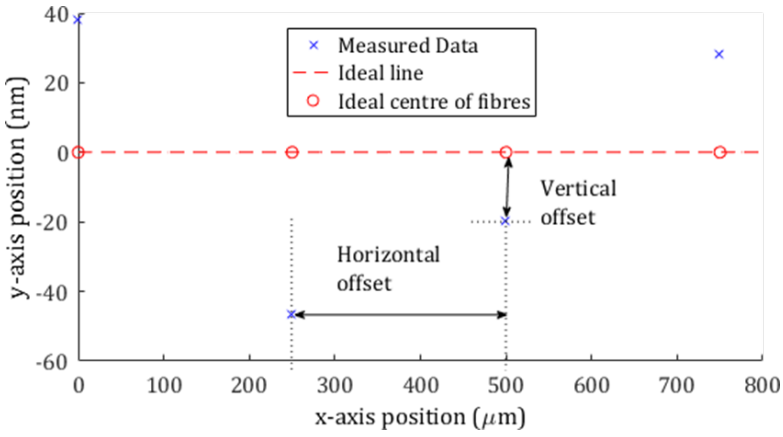

Figure 6.6 – Locating the horizontal and vertical offsets in the ports of the v-groove array.

of fibre arrays with four and ten ports. The measured offsets and associated losses have been listed in Appendix D for reference.

6.5.1 V-groove fibre arrays for wavelengths near 1550 nm

A characterisation dataset for a 4-port device at 1550 nm (SQS-4-1-1550) has been shown in Figure 6.7. The location of each fibre port is marked by a cross and shown in relation to the "ideal" centre of the fibres. The arrows have been used to indicate the loss induced by the magnitude of the radial offset. The manufacturer has specified the total offset misalignment for each fibre port, which has been drawn as a green circle. All fibre positions were found to be within specification for this device. The error of the measurement by drift of the system has been measured as 25 nm; this has not been drawn on Figure 6.7.

Separate measurements were undertaken on four additional 4-port devices for wavelengths at 1550 nm from another manufacturer (OzOptics). The devices under test were found to be well within the stated specification of ±0.5 µm. The average horizontal and vertical offsets have been calculated as $\overline{x} = 279 \pm 34$ nm and $\overline{y} = 139 \pm 37$ nm. The uncertainty has been stated as the standard error of the measurements; it is approximately equal to the drift in the measurement system.

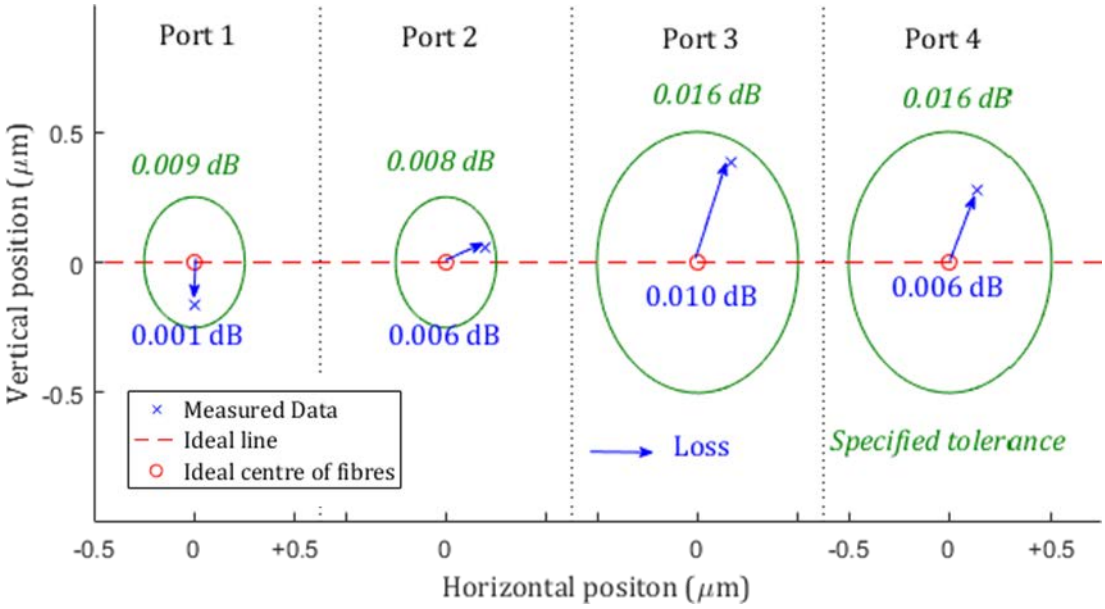

Figure 6.7 – Mapping of fibre positions and misalignment losses on 4-port fibre v-groove array operating at wavelengths near 1550 nm. Device: SQS-4-1-1550.

The corresponding horizontal and vertical misalignment losses are $3.25\pm0.05\times10^{-3}$ dB and $0.81\pm0.06\times10^{-3}$ dB, respectively. The total inferred misalignment loss was calculated as $5.85\pm1.62\times10^{-3}$ dB.

6.5.1 V-groove fibre arrays for wavelengths near 800 nm

Two 4-port fibre v-groove arrays for operation at wavelengths near 800 nm have been characterised. The measurements results from one of the two devices (SQS-4-1-800) have been summarised in Figure 6.8 using the same methodology as in the previous section. The offset and error in positioning for ports 2 and 3 in these devices have been found outside of manufacturer's specified tolerance, resulting in losses as high as 0.28 dB in port 2. The discrepancy may have been caused by the different measurement techniques. This is illustrated by considering the average radial offset of the device.

The measured radial offset for each port of this device is based on the reference system described previously. The average radial offset has been calculated as $\overline{r_1} = 780 \pm 410$ nm. The error stated is the standard deviation of the measurements, which has been found to be significantly higher than the drift. This device's corresponding average misalignment has been calculated as $\overline{r_{S1}} = 738 \pm 359$ nm,

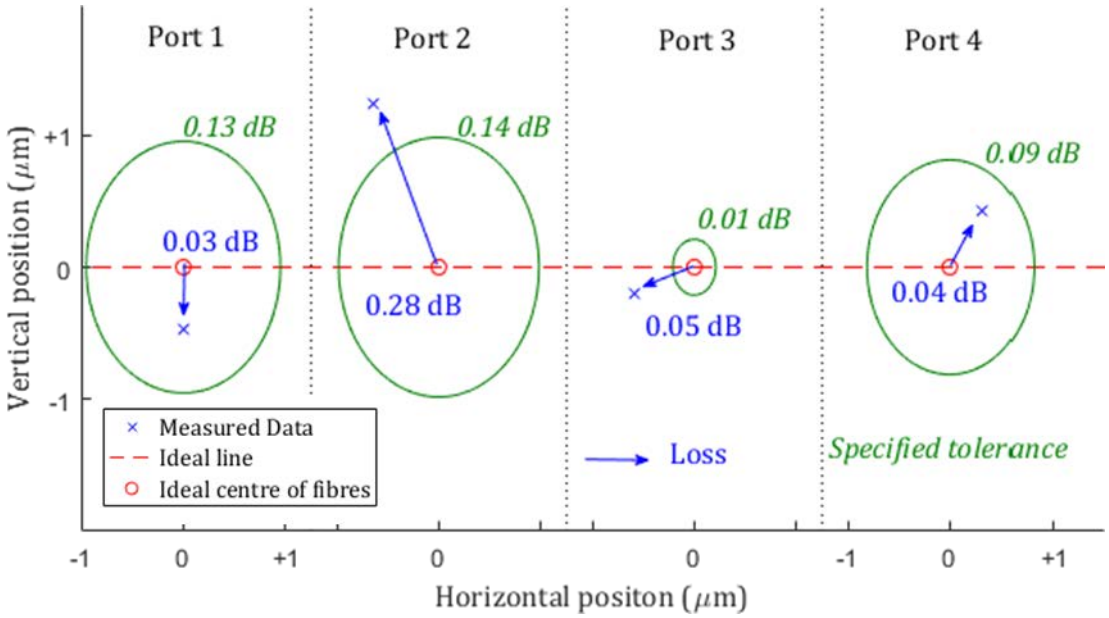

Figure 6.8 – Mapping of fibre positions and misalignment losses on 4-port fibre v-groove array operating at wavelengths near 800 nm. Device: SQS-4-1-800.

based on the manufacturer's specification. The stated error is the standard deviation in the offset position and the average offsets have been found to be within one standard deviation of each other.

Similar findings have been noted for device SQS-4-2, and an analogous discussion has been presented for completeness in Appendix D. Under typical alignment procedures, the average loss due to misalignment may be tolerable. The DUW platform can be used to create adapter chips to correct horizontal offsets, offering improvements in coupling efficiency of up to 0.058 dB per port at 800 nm for the two devices that have been characterised as part of this study. The results motivate further investigation into 4-port v-groove assemblies to support development work into fabricating DUW adapter blocks to minimise fibre-to-waveguide connection losses for these two v-groove fibre arrays. It was remarked that both devices were issued from the same fabrication batch.

Further characterisation was conducted on a 10-port fibre v-groove assembly for wavelengths of operation near 800 nm. The device has been issued from a different fabrication batch. The average horizontal and vertical offsets for the 10-port v-groove array have been measured respectively *as* $\overline{x} = 152 \pm 66$ *nm and* $\overline{y} = 95 \pm 66$ *nm. The error has been taken as the drift error in* the system. The corresponding horizontal and vertical misalignment losses have been calculated as $3.30 \pm 0.62 \times 10^{-3}$ dB and $1.30 \pm 0.88 \times 10^{-3}$ dB, respectively. The total inferred misalignment loss was calculated as $7.03 \pm 0.62 \times 10^{-3}$ dB. The specification sheet with the alignment tolerance of each port was not available for this device; however, the offsets are considerably better than those for the 4-port devices that have been considered in this study.

6.6 Conclusions and further work

The work in this chapter has investigated the losses associated with fibre positioning in v-groove arrays to inform on these devices' suitability as low-loss interconnects for QIP networks. The author has developed a characterisation and data processing system for the measurement of the horizontal and vertical positioning of individual fibres in v-groove arrays. Fibre positioning has been found to be within average specified radial tolerance. The experimental study has found

that worst coupling efficiencies from horizontal misalignment are 99.81% per port at 1550 nm. The average insertion efficiency with vertical misalignment has been measured as 99.93%. For devices operating near 800 nm, the worst coupling efficiency measured from horizontal misalignment was 98.67%. The coupling efficiencies have been found to be batch dependent; indeed, the average coupling efficiency for the 10-port device considered in this study has been measured as 99.92%. Horizontal misalignment compensation adapter chips could be fabricated through DUW to cancel these coupling losses, in particular for devices that have been specified to have poorer fabrication tolerances.

The study has found that average losses from vertical misalignment to be of the same order of magnitude to horizontal offsets. Further work would use the characterisation results to compensate for both vertical and horizontal offsets through, for instance, the development of 3D waveguide adapter chips fabricated by femtosecond laser writing in bulk glass for instance [144]. The characterisation system could be extended to study v-groove fibre arrays for schemes requiring photonics interlinks at shorter wavelengths [145]. Misalignment losses, calculated from equation (6.1), could be as high as 0.69 dB (~15% loss) for SM-400 fibre (MFD = 2.5-3.4 μm at 480 nm) mounted in v-groove arrays with misalignment tolerances of ±0.5 μm.

Misalignment losses is one of the contributors to insertion loss. Modal mismatch (Chapters 2 and 6) is an important parameter to optimise the coupling efficiency between waveguides and fibres. The fabrication of adapter chips would require careful optimisation of the mode profile of laser written waveguides, as good coupling to commercial fibre is imperative for optimal fibre-to-waveguide coupling.

The research into the characterisation of the v-groove fibre arrays has permitted preliminary characterisation of the drift in the DUW system. The implementation of a self-referencing system could be developed to minimise the degradation in precision linked to scanning more ports consecutively. System drift occurs as a function of time, and may be detrimental for larger phase-sensitive devices. The results motivate the need to write small chips to minimise drift occurring during fabrication with the current system.

Chapter 7 Pathways to impact: an optical engineering approach to public engagement with research

Photonics has been recognised as a "key enabling technology" [1] with far-reaching economic potential in and beyond the 21st century. Despite this, much work remains to be done to inform the public on the science and technologies that benefit from photonics research.

This chapter will outline how the "traditional" research activities cannot be disentangled from the social responsibility that researchers face. The work carried out as part of the author's PhD has been undertaken in an evolving socio-economic climate and a dynamic framework for delivering and assessing research-inspired activities for engaging with the public. This study reports the extension of this framework to implement research-inspired activities to engage with the public, with focus on methods to measure "Impact". The study distinguishes itself from traditional physics education research [146] in its approach to designing, implementing and evaluating research-inspired activities to engage with the public outside of formal education environments (school, university). The use of the acronym *PER* in this chapter denotes public engagement with research and not physics education research.

The structure of the chapter is as follows. Section 7.1 outlines the drivers for taking the research out of the laboratory through diverse "experiments" in outreach

education and public engagement with research activities. Section 7.2 presents a case study highlighting methods to design, deliver and evaluate activities intended to reach new audiences, with emphasis on methods for evaluating Impact. Section 7.3 highlights how the interactions between researchers and diverse publics have been fed back into the research exercise through the development of key transferable skills and renewed enthusiasm to complete a full cycle of engagement, measured through case studies of research-inspired projects for school curriculum enrichment. The chapter will conclude by offering a summary of lessons learnt and future perspectives. The account is based on the following works published by this author and collaborators at the University of Southampton [147]–[152], and references to supporting articles will be made throughout this chapter. Funds in excess of £35,000 GBP have been raised by the author to support this work and four awards have resulted from these endeavours; a list of these grants and awards is presented in Appendix A.

7.1 Drivers for engagement

The following section describes socio-economic drivers that are enabling researchers to develop activities for the education of school students and the public on fundamental optical sciences and their applications in industry and research.

7.1.1 Widening participation

The UK suffers from a well-documented skills shortage of students in science, engineering, technology and mathematics (STEM) disciplines in higher education [153]. Intake into STEM-related subjects is hindered by multiple barriers of entry such as gender, ethnicity, public perception, specialist teaching as well as socio-economic factors. Raising aspirations and broadening the horizon of students to include research and science based careers are essential elements towards addressing this shortfall [154]. Universities have taken measures to work with a wider pool of potential students through outreach activities to boost student recruitment [155]. Since the 2012 increase in tuition fees for UK students to attend UK universities, an Access Agreement has been imposed on universities by the UK government's Office for Fair Access (OFFA). OFFA stipulated that full fees could be

charged if a percentage was spent on reaching disadvantaged students. As a direct consequence for this need to *Widen Participation,* universities have invested funding in the development of education programmes driven by researchers that will reach a student population as broad as possible. An important factor in such programmes is the development of strong partnerships with schools, which will be discussed in section 7.3.

7.1.2 Public engagement with research

Public engagement with research is defined by the UK's National Coordinating Centre for Public Engagement (NCCPE) as "*a two-way process, involving interaction and listening, with the goal of generating mutual benefit*" [156]. UK researchers now have "a strategic commitment to public engagement" and "are recognized and valued for their involvement with public engagement activities" [157]. As a result, they have a duty to demonstrate 'impact', i.e. to show "a demonstrable contribution that excellent research makes to society and the economy" [158]. The activity must be designed accordingly to measure 'impact' through *reach* and *delivery quality*. The purpose of photonics "outreach" has consequently been enriched to become an activity encouraging a two-way dialogue between the public and academics about the university's actual photonics research.

7.1.3 Raising Science Capital

Science Capital is "a conceptual device for collating various types of economic, social and cultural capital that specifically relate to science" [159]. An individual's Science Capital can be considered as an integrated measure of their science related knowledge, skills and experiences and it has been demonstrated that the amount of Science Capital affects attitudes towards science with high scorers more likely to follow STEM subjects. This concept also provides a tool to assess how people engage with science and the influences that impact on this engagement, that as discussed above, include school, home and family, science learning and experiences gained via the environment and everyday life and events.

The dynamic environment found in higher education institutions and the education actions they propose can considerably enrich the public's engagement with STEM

subjects, although a comprehensive review of these would be too consequential in the context of this discussion. The plethora of proposed outreach events can contribute to the raising of an individual's aspirations and thus their Science Capital through increased exposure to different activities and in addition by providing friends and family with information on opportunities available in STEM careers. This in turn plays a mediating role on the aspirations of children towards careers in science [160]. Thus, engaging with a broader range of audiences is key to outreach and public engagement endeavours. An illustrative case study is presented in the following section.

7.2 Reaching new audiences through creative partnerships

One strategy to gain access to wider areas of the community is to diversify the offerings of engagement and education actions to different types of events outside of academic environments. This section will present a case study of the development of a novel engagement platform, the 'Reflecting Photonics' show garden, to engage new audiences with research through a creative collaboration linking art and research. The author was part of the university's project management team and the contributions of individuals are detailed in Appendix E. The details provided below are based on a paper presented in reference [148].

7.2.1 Reflecting Photonics: garden design and delivery

The 'Reflecting Photonics' show garden was exhibited at the 2015 Royal Horticultural Society (RHS) Flower Show in Tatton Park, UK, to celebrate the International Year of Light and Light-based Technologies (IYL 2015). Elks-Smith Garden Design collaborated with researchers, marketing and outreach professionals from the University of Southampton to design, construct and exhibit a photonics-themed garden. The garden and supporting exhibition united science and art to reach new audiences, particularly family groups alongside other key influencers to the young.

The garden was designed through extensive collaboration between the external partners and photonics researchers. The design process included a tour of the university's cleanrooms to present different processes for manufacturing fibre

optics and silica-based integrated photonics circuits – see Figure 7.1 (a). These technical elements were included in the garden proposal for the RHS. Leaflets on the research involved in these processes were prepared and distributed as handouts to attendees during the flower show. A team of researchers were present during the show to explain the garden's underlying science to the RHS visitors, as well as answer horticultural questions.

The garden is shown in Figure 7.1 (b). Over 20 types of flowers were selected – including *Hydrangea paniculata 'Early Sensation'*, and *Verbena officinalis 'Bampton'*– to reflect the spectrum of visible colour. The pavilion was brightly coloured and unusually shaped, thus attracting the audience's attention from afar to the show garden. Visitors could also see the glowing hanging Perspex slabs from a distance. These features were used to explain total internal reflection and draw analogies with slab waveguides used for integrated photonics (Chapter 2). A path through the site was designed as a metaphor for a wave-form of light travelling inside fibre optics. The designer used acrylic tubes protruding from earth mounds to reflect the fact that our telecommunications fibres are buried underground. The show garden space included a tent where researchers set up experiments to engage the public with their research and the underlying science.

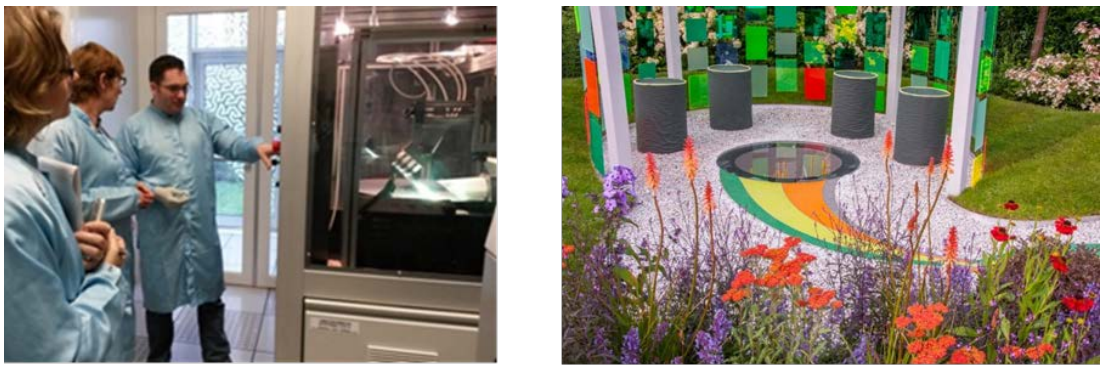

(a) (b)

Figure 7.1 – (a) Garden designer Helen Elks-Smith visited the ORC cleanrooms facilities as part of the design process; here Dr. C. Holmes demonstrates flame hydrolysis deposition (Chapter 2). (b) The garden pavilion and the fibre optic well. The vertical Perspex sheets can be seen hanging from the pavilion.

7.2.2 Evaluation

Approximately 80,000 visitors were expected to attend the 2015 RHS Flower Show Tatton Park and a much larger number to read about it via the media. This section presents metrics and tools employed to evaluate our activity's impact.

7.2.2.1 Exploiting the media and social media

The RHS Flower Show Tatton Park is an annual national event with a broad appeal to the general public. The show was featured on national and regional television (TV) and press, including national weather reports, and the national channel BBC2's show "Gardeners' World" aired at prime-time TV spots. Based on the average viewing figures for *Gardeners' World,* approximately 3 million people saw the *Reflecting Photonics* garden, and through this, had exposure to the concepts of 'photonics'. 16 features of the garden were shown and documented on national TV or in the national & regional general press, in addition to further features in the specialised (horticultural, photonics) press, blog posts, and promotion through the communication channels of the University of Southampton and the garden design partners [148]. During the show, over 75,400 Tweet impressions on social media were recorded through analytics tools.

7.2.2.2 Mixed qualitative and quantitative results

A mixed methodology using qualitative and quantitative tools was used to evaluate the impact of the PER activity. This was done in practice by handing out giveaways. The 'reach' of an activity was measured quantitatively by the number of items handed out. The 'significance' of the interaction was measured by further classifying these items into different categories. Four levels of significance ratings have been employed in this methodology:

- Level 1: General interaction with garden (garden information leaflets).
- Level 2: Scientific interaction in the garden and tent (diffraction gratings).
- Level-3: Pitched scientific and educational interaction in the science tent (photonics bookmarks and pens)
- Level-4: Demonstration of assimilation of knowledge or change of behaviour (IYL 2015 3D-printed keyrings)

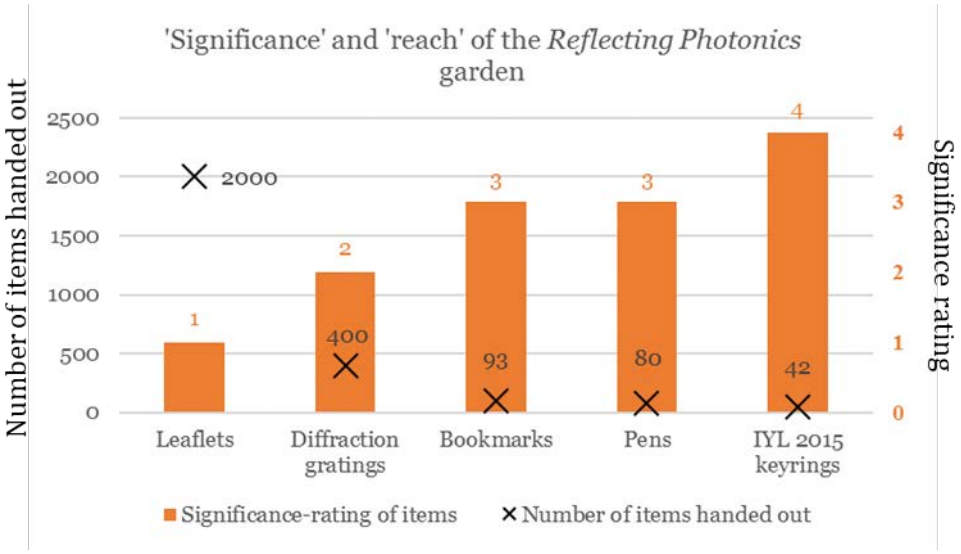

Figure 7.2 – Mixed qualitative and quantitative assessment of the *Reflecting Photonics* garden. Figure adapted from [148].

The different types of handout items map the depth and length of discussion with visitors. The team were present for the two-day period of the garden show and distributed 2,000 leaflets to visitors who walked through the exhibit (level-1 significance rating). 400 research-oriented conversations were counted (level-2 significance rating). Over the same period in the science tent, 93 bookmarks and 80 pens promoting a European-funded photonics awareness campaign (Photonics4All) were distributed (level-3 significance rating). 42 people had lengthy (10-15 minutes) conversations with researchers and completed and returned an evaluation survey and competition entry, earning them an IYL 2015 keyring (level-4 significance rating). Figure 7.2 summarizes the reach and significance of the activity during the two days of exhibiting the garden.

7.2.2.3 Survey-based evaluation

Surveys were used to measure the demographics of the audience and a quiz was used to measure assimilation of knowledge. The audience members were asked to rate the garden on a 5-point Likert scale (with '5' being most positive). The survey also asked: "How likely were you / are you to recommend studying physics and optics to a friend or family member?" and to give an answer before and after the interaction. 39 surveys were used in the analysis and this section summarises the results.

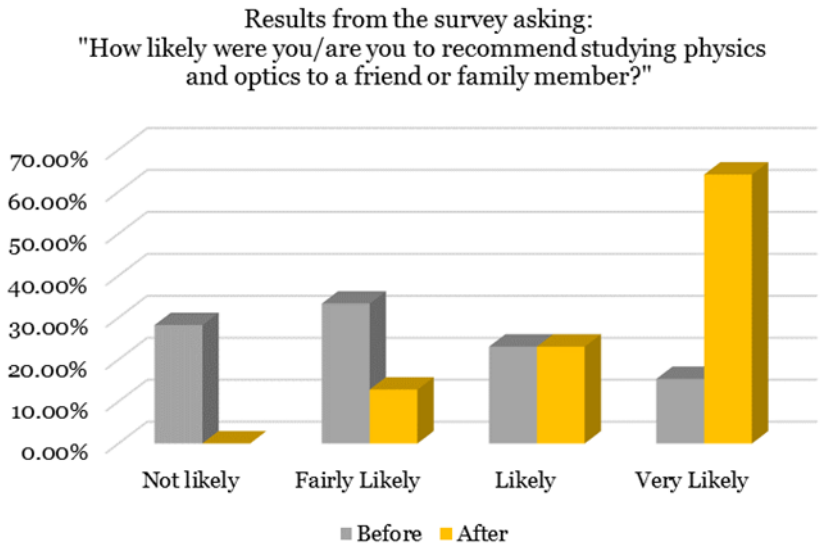

Figure 7.3 – Change of attitude recorded from the surveys before and after interaction with the public engagement team. Figure adapted from [148].

55% of attendees were female, 38% male and 7% did not detail their gender in the questionnaire. 60% of attendees were over the age of 44. The demographics were consistent with the targeted audience. The garden received an average enjoyment rating of 4.6/5 according to the surveys conducted by the University of Southampton public engagement team. 83% of the people who completed the survey in full indicated a positive change in attitude towards photonics after their visit and discussions and would recommend studying or working with photonics to a family or friend; 17% of respondents had a 4-point positive increase. No negative changes of attitudes were recorded. The survey responses are summarized in Figure 7.3.

7.2.3 Outcome of the project

The show garden won an RHS Gold Medal award and the coveted 'People's Choice Award' for the best large garden at the show. The project subsequently won the 2015 South East England Physics Network Public Engagement Innovation Project Award. The project allowed direct interaction with over 2,000 people in the garden over the two days, with an estimated 400 having a discussion on photonics science and research. The results from the surveys found that engagement was made with

the target audience, and that a positive change of behaviour was achieved on influencers of the young. This project also provided an opportunity to assess different techniques for evaluating the event's impact. Such techniques of impact assessment could be applied to all public events, including more traditional ventures such as in museums and at science fairs.

Public events that provide the opportunity to engage with influencers of the young are essential to raise the Science Capital of children. These efforts should be conducted in parallel with education endeavours targeted directly at school students. The following sections provide a description of research-driven school activities designed during this author's study.

7.3 Research-based education for schools

This section presents activities aimed at school students developed by the author to enhance the national curriculum with photonics research. The work stems from an optics and photonics education programme targeted at pre-school children that had been developed at Southampton [161], [162]. The reader is directed to references [150], [151] for supplementary details on the equipment used for the delivery of these activities, in addition to considerations for the training, equipment safety, portability, publicity and funding for student-led community education activities.

7.3.1 Research-driven school curriculum enhancement

Workshops have been developed on the themes of photonics science and research for classroom-based interaction with students aged 8-14 years of age (key stages, 2 and 3 of the UK national curriculum). The learning objectives have been designed to match elements of the UK national curriculum for science. The classes are based around active learning pedagogies [163], with emphasis on experimental work and making the student the centre of the learning activity. The classes are application driven and present links to the research and real-world applications. The workshops have been designed to provide insight into research and illustrate what the work of a researcher entails.

An example of a primary school workshop developed has been presented in [149] and an accompanying lesson plan is included in Appendix E. The workshop is structured around three main activities on the electromagnetic spectrum, the human eye and telecommunications. Quiz-based evaluations have been used to measure reach, assess demographics, record the assimilation of knowledge, assess enjoyment and measure the change of attitude through the interaction. Evaluation of results from workshops using such a format and conducted with 311 UK Year 6 students in 2016 have found high levels of enjoyment and assimilation of learning based on the quiz-based evaluation methods [149]. An example of how learning objectives can be related to national curriculum elements and applications is illustrated in Table 7.1; in this example, the "real-world" application of the optical concepts being illustrated and explained made use of a cathedral as the subject matter for the workshop which was run as part of the Winchester Cathedral Primary Science Festival. Additional formal outlines for classes on telecommunications and photonics applications photonics developed by the author and colleagues have been presented in [147] and [152], respectively.

The workshops are an essential component of the interaction between researchers and students. The author has directed 36 researchers and engaged with 1,827 students from 80 schools over the course of this study through this format of engagement. One limitation of this point-of-contact interaction is the limited follow-up. The strategies for long-term evaluation and enriching activity design through partnerships are outlined in the following section.

Table 7.1 – Activity learning objectives and links to national curriculum and cathedrals.

Activity learning objective	**Links to national curriculum elements** [164]	**Relevance to cathedrals**
Name the primary colours of light.	Experience a range of light-based phenomena including coloured filters and rainbows.	Explain how stained glass works.
Recognise the elements of the human eye.	Explain that we see things because light travels from light sources or objects and then to our eyes.	Light is essential in cathedrals to see stories.
Enjoyment of interactive demonstrations.	Emotions towards science through experimentation.	Showcase non-conflicting views.

7.3.2 School-university partnerships

An efficient strategy for working with schools is through School-University Partnerships (SUP). SUPs offer a rich and dynamic platform for delivering educational and impactful activities. Partnered institutions can obtain many mutual benefits including increasing pupil performance, understanding where research work fits into the curriculum, access to researchers of the future, sharing of best practices to improve pedagogy, training for school and university staff, and better collection of data for impact; the reader is referred to recent work by Wager describing comprehensively planning and delivery strategies for SUPs [165].

Varied activities were designed to enhance and diversify the offering of the activities between the author and a partner school. These activities were run during IYL 2015 and have been presented in [147]. The activities consisted of a combination of project-based homework (poster competition), school assembly lectures, introductory short workshops and stand-alone classes on telecommunications. 1,125 students in UK Year 8 and Year 10 aged 12-15 years from the partner school took part in these different activities carried out throughout IYL 2015.

The activities designed have also allowed the professional development of the both the school and research students engaging in the activities. Through this SUP, the author organised the logistics, funding and before and after preparation and debriefing of participants of a trip for two school pupils, four research students and accompanying support teachers and staff to participate in the opening ceremony of the IYL 2015 held at the UNESCO headquarters in Paris, France. The experience allowed the students to gain exposure to all sectors of optics and photonics as well as an opportunity for professional development by attending this prestigious event. The impact was educational, aspirational and professional for both researchers and students. Table 7.2 presents a selection of quotes reflecting the personal impact on the students who participated in this activity.

Table 7.2 – Selected quotes from students attending the IYL 2015 opening ceremony.

#	Quotes
1	"[The opening ceremony] shows different people from different areas, different countries, different cultures are all working within this same area of light."
2	"The scale of the opening ceremony made it so special. There were so many people there that you were just completely engrossed in the science."
3	"A lot of people think that science and art are two separate things and actually you need both of them and you need them to work together."
4	"It's reassuring to me that I am doing something that is going to benefit mankind."
5	"Now it is our responsibility to pass the baton; to take the responsibility and educate at the very basic level to teach them about photonics and light and how light has made a difference in our lives."

7.3.3 Findings

The development and design of educational material based on research concepts allows the enrichment of the school national curriculum. Thorough planning is required prior to undertaking work with schools to match the demand of teachers for educational enhancement. It is helpful to identify key players in SUPs, such as teachers, industrial liaison partners in schools or outreach and public engagement officers at universities, and make use of their experience in developing and delivering class-based activities. Assessment methods must be planned to efficiently assess pupils and setting achievable goals is important for school projects.

Measuring the long-term impact of school-based activities is challenging: unless one can have follow-up contact details for students and the project has funding to track the progression of the students, it is difficult to demonstrate a correlation between present activities and admissions into physics or electronics engineering undergraduate courses. SUPs can help monitor pupil progress throughout their formative school years. Surveys of students entering higher education may offer some insight into the resulting impact of these activities.

7.4 Conclusions and further work

This chapter has outlined research-based education initiatives conducted throughout this study in the context of an evolving research activity. A rich combination of socio-economic factors allows researchers to engage with the public and children to ensure a more cohesive approach to the advancement of science and technology and raising Science Capital in society.

The concept of Photonics, and the underlying science and research enabled by it, has been introduced to 2,952 students from 81 schools in the South of England and over 6,000 people in public events through initiatives driven by the author over the course of this study. In addition, the author has participated and run workshops held in China, Canada and the USA during international education and research conferences. Considerations for international activities have been discussed in [151].

Education and training roles play an important part in the development of transferable skills for researchers and students. A summary of personal development offered by these activities is provided in Table 7.3. There are mutual benefits to engagement activities. The implementation of methods for evaluating behavioural change on participants and researchers will permit further evaluation of the long-term impact of these activities [166].

Based on this experience one area that needs further development is the need to be able to accurately measure the reach of “low-significance” interactions, especially in public events. Further research into the implementation of surveys and qualitative assessment for engagement in public events is required. Online resources and training courses are available through the NCCPE to assist in the design and processing of surveys. Reports published after the completion of these activities will be useful to provide researchers with conceptual frameworks that can be applied to enhance the sophistication of the evaluation [167].

Physics education already benefits from well-established evaluation of concepts for force and motion education [168], [169]. Light and Optics Conceptual Evaluation methods have been described in the framework of Active Learning Optics and

Photonics programme (section 7.3). Methods to incorporate activities designed for school children and the public would be an effective tool for the evaluation of the impact of engagement activities.

SUPs provide a dynamic environment for addressing the STEM skills shortage. The support of these schemes may help address the shortfall in specialist teachers that has been identified as a barrier of entry to STEM. Measuring long-term impact would require significantly more administrative resources and continued cooperation with the external partners. Other high-level initiatives could be considered to tackle the skills STEM shortage. Vocational education for high school students has been recognised as an effective method [170]. Studies on the unconscious bias may also address the under-representation certain demographic groups in higher education [171].

Table 7.3 – Skills development through outreach and public engagement with research activities

Skills developed
Oral and written communication and presentation skills
Fundraising and budgeting
Event, project and team management
Production of documentation (risk assessments, information leaflets, flower description sheet)
Working with internal and external collaborators
Evaluation methodology
Observation skills
Adapting to unexpected situations

Chapter 8 Conclusions

8.1 Conclusions

This study has developed a platform to build functional building blocks that can be used to scale networks intended for quantum information processing (QIP) experiments.

Chapter 2 presented the techniques of flame hydrolysis deposition (FHD), direct UV writing (DUW) and physical micromachining that can be used to fabricate silica-on-silicon (SoS) waveguides and gratings which meet the stringent requirements imposed by QIP. Uniformity, low-loss connectivity and the ability to characterise material, waveguide and grating properties are essential for integrating building blocks into larger and more complex networks.

Chapter 3 has described the first implementation of in-line planar waveguide polarisers based on 45° tilted gratings. Proof-of-concept devices have a polarisation-dependent loss of 0.25 dB/mm and bandwidth impairments better than 0.3 dB in the C-band. An accompanying theoretical study has given new insights into the fabrication platform through the spectral analysis of the gratings.

Titled gratings permit new planar device architectures and Chapter 4 provides detailed results of the first demonstration of an integrated polarising coupler based on 45° tilted gratings. Polarisation extinction ratios in excess of 28.5 dB have been measured in fabricated devices. The architecture relies on the excellent phase tolerance offered by the DUW fabrication system and good propagation through slab planar waveguides. Small-spot DUW allows the fabrication of arrays with polarisation-dependent coupling with a packing density matching commercial fibre v-groove arrays. The study has been supported by a theoretical framework for the design and optimisation of this architecture.

The FHD fabrication process has been adapted to fabricate high-birefringence waveguides through the control of the material composition of slab waveguides. The adapted material composition is compatible with DUW for the generation of waveguides and gratings. Chips made by the author are being tested for the generation of spontaneous four-wave mixing heralded single-photon sources operating in the visible and NIR in experimental investigations being carried out by collaborators at the University of Oxford's Ultrafast Quantum Optics and Optical Metrology research group. Chapter 5 also described the development of a process for the integration of endcaps on planar chips for high-power management applications to add new functionality to the SoS FHD platform.

The losses associated with fibre positioning in v-groove arrays have been studied and this aspect is presented in Chapter 6 together with a system for their characterisation that has been implemented by the author. The test system allows the separate measurement of the horizontal and vertical positioning for calculating axis-dependent insertion loss. Losses due to horizontal misalignment have been measured as less than 0.01dB per port and 0.09 dB per port for devices operating near 1550 nm and 800 nm respectively. The results have shown modest improvements to losses due to misalignment are possible. Optimisation of waveguide mode field diameters is currently a more critical area of investigation (section 8.2.1).

Chapter 7 has outlined research-based education initiatives conducted throughout this study. A rich combination of socio-economic factors is allowing researchers to engage with the general public and in particular young people to raise Science Capital. Examples of research-inspired projects for the public and schools carried out in the UK have been presented alongside methods for assessing the reach and significance of the activity. The concept of Photonics, and the underlying science and research associated with it, has been introduced to 2,952 students from 81 schools in the South of England and over 6,000 people in public events ranging from public lectures to science fairs and garden shows through initiatives driven and lead by the author over the course of this study.

8.2 Future perspectives

The following section discusses further work that could be conducted to extend and validate the findings of this thesis.

8.2.1 Coupling loss optimisation

Insertion loss is critical to the scaling of QIP experiments. The characterisation of waveguide mode field diameter offers a promising route for the validation of DUW. The current experimental setup (Section 5.2.4) is limited to operation in the visible regime, and waveguide mode properties at other wavelengths have only been inferred from modelling. The development of an imaging system operating over a wider range of wavelengths, and specifically to include the near-infrared spectral region, will permit more accurate profiling and the characterisation of insertion loss.

The scaling of networks will require connecting arrays of waveguides and fibres. Horizontal misalignment compensation adapter chips could be fabricated through DUW to cancel these coupling losses, in particular for devices that have been specified to have poorer fabrication tolerances and for shorter wavelengths of operation. The development of DUW for writing gratings into fibres of v-groove arrays has been identified as a strategy to provide very accurate measurements of insertion loss. Utilising grating-based measurement techniques could be used for measuring fibre-to-waveguide coupling loss at individual ports.

8.2.2 Layer fabrication uniformity

The control of the variation in the FHD layer thickness and composition are necessary to produce highly uniform planar devices. This is an essential requirement for the scaling of QIP experiments and utilising arrays of uniform waveguides. Improvements in uniformity will also reduce scattering and absorption-based losses for radiated modes propagating through the slab waveguide layer. This has the potential for improving the bandwidth response of integrated polarising beam splitters and phase-controlled polarisation-sensitive waveguide arrays based on tilted gratings operating through planar mode coupling.

Tilted gratings offer routes to various novel architectures. These may make use of the ability to detune grating resonance wavelength both via the rotation of the

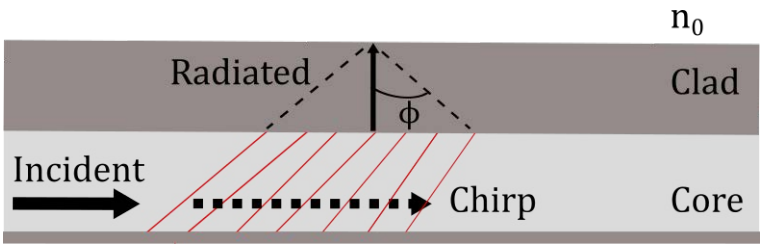

Figure 8.1 – Grating planar mode coupling output coupler based on tilted gratings.

writing stage and control of the exposure period. Focusing devices, following the architecture presented in Figure 8.1, based on gratings with numerical aperture matching fibres, may be fabricated through the detuning of the tilted grating wavelength by 225 nm [172]. The detuning can already be achieved with the current control system of the DUW (Section 2.5.4).

8.2.3 Refractive index contrast enhancement

Improved stage tolerance position for the DUW process will permit the refractive index contrast enhancement for waveguide and grating formation. The fabrication process will improve the efficiency of in-line waveguide polarisers based on 45^0 tilted gratings for the fabrication of polarisers with higher polarisation extinction ratios.

Strategies for the optimisation of the grating strength in DUW waveguides would considerably enhance the range of applications. Higher waveguide confinement is required for the integration of bends without compromising propagation loss through bend loss. This will be useful for efficient pigtail-to-waveguide adapter chips and optimised cross-couplers at a range of wavelengths [59]. Ring resonator structures may be further investigated in DUW processes. The structures are extremely sensitive to loss and may offer new insights into the photosensitivity mechanisms of the DUW fabrication process, as well as applications in telecommunications and sensing.

Investigations into other mechanisms for waveguide generation through small-spot UV writing may allow higher refractive index contrast modulation for waveguides and gratings. Methods currently being investigated using 213 nm lasers offer the potential for very high-grating modulation contrast in waveguides. Combining the

process with small-spot UV writing will offer the phase stability offered by the current system. This may allow out-of-plane grating couplers [173], and if combined with improved system stability may permit out-of-plane focusing devices, that have found applications in QIP experiments for trapping ion qubits [174].

8.2.4 Integrated spontaneous four-wave mixing four-photon-pair source

The improvements of the capability of the SoS DUW platform discussed previously will enable further applications for QIP experiments requiring a low-loss platform. This is illustrated through the architecture required for an on-chip integrated spontaneous four-wave mixing four-photon-pair source. Optimisation of coupling loss, layer uniformity and refractive index matching contrast will all contribute towards the scaling of integrated waveguide-based heralded single-photon sources. Figure 8.2 describes the setup for experiments for the realisation of such a network to permit further QIP experiments in areas of high impact. The architecture is comprised of the following elements:

- Endcaps for power management of input beam and v-groove fibre arrays for the collection of signals.
- Integration of 1x4 splitter 50:50 beam-splitters, based on DUW cross-coupler architecture and optimised crossing angles for pump wavelengths.
- Grating-based diagnostic structures for non-destructive and classical characterisation waveguide properties (loss, birefringence).
- Alignment channels with gratings for optimisation of chip-to-chip alignment.
- In-line waveguide polarisers with polarisation-dependent loss in excess of 20 dB to provide on-chip inhibitors for cascaded Raman scattering.
- The filtering channels may be further isolated with the use of physical micromachining processes to produce low-surface roughness isolation trenches.

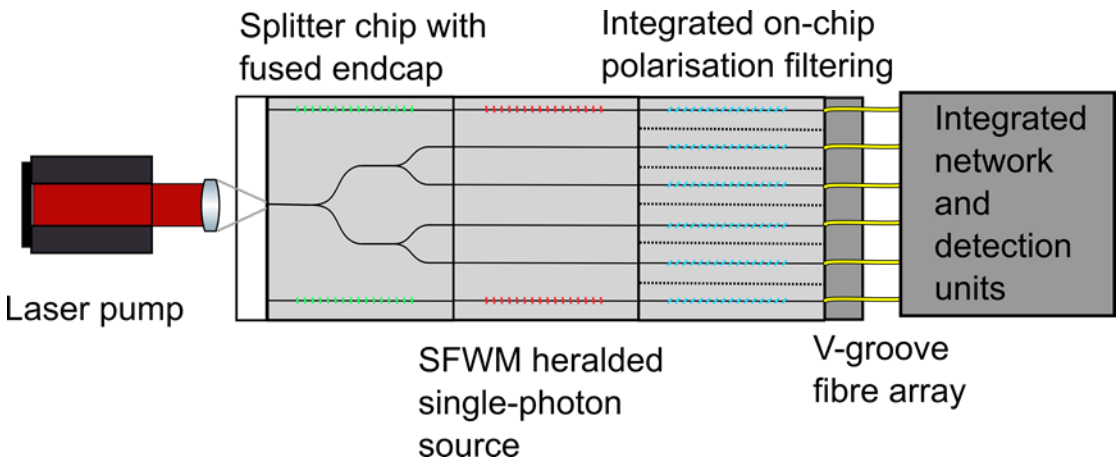

Figure 8.2 – On-chip spontaneous four-wave mixing for the generation of four heralded photon-pairs.

8.2.5 Combined research and engagement endeavours

Combining research with public engagement and education activities is critical to raise the profile of the field and ensure its long-term prosperity. Further work is needed to implement tools that will assess the impact of engagement endeavours on researchers in photonics-based research [166]. The support of national and institutional initiatives for working with wider areas of the community is essential to develop the Science Capital. Further work is also required for measuring accurately the reach of "low-significance" interactions, especially in public events.

Enhancing school-university partnerships for combined research and education projects is essential to raise the profile of the field and inform on careers in STEM. Measuring the long-term impact for working with students in primary and secondary schools would require significantly more administrative resources and enhanced partnerships. One approach would be developing photonics-based extended project qualifications with organisations seeking to enhance education through research projects, such as the UK's Institute for Research in Schools. Other high-level initiatives could be considered to tackle the skills STEM shortage, such as vocational education and the study of unconscious bias.

Appendix A Awards, grants and publication List

Awards

Optical Engineering & Quantum Photonics Group, "Public Engagement Research Group Award," Highly commended for public engagement with research activities, South East England Physics Network, 2017.

M. T. Posner, "Excellence in Volunteering Award for best contribution to a student society," for group projects undertaken with the Optics and Photonics Society and Road Cycling Club, University of Southampton Student Union, 2017.

M. T. Posner, N. H. L. Wong, "Director's Award in Engagement & Outreach," for exceptional contribution to university activities University of Southampton Doctoral College, 2016.

M. T. Posner, P. V John, D. Standen, N. V. Wheeler, L. D. van Putten, N. Soper, T. Parsonage, and G. Brambilla, "Public Engagement Innovation Award," for Reflecting Photonics Garden at 2015 Royal Horticultural Society Flower Show Tatton Park, South East England Physics Network, 2015.

M. T. Posner, "Director's Award," for Outstanding Contribution in leadership in department's outreach activities, Optoelectronics Research Centre, 2014.

Grants

- **Lead author**

"IOP Research Student Conference Fund," Institute of Physics Science Communicators Group, £300 GBP, 2017.

"IAA Research, Engagement and Impact Fund," Engineering and Physical Sciences Research Council (EPSRC) University of Southampton Impact Acceleration, £800 GBP, 2017.

"Teaching Students to Teach Students", The Optical Society (OSA), $500 USD, 2016.

"Lightwave, Light Express and teacher CPD," EPSRC Future Photonics Manufacturing Hub, Pathways to Impact funding, £15,000 GBP, 2016.

"Widening Participation outreach program," University of Southampton Outreach Office, £3,000 GBP, 2015-2016.

"SPIE International Year of Light Activity grant," International Society for Optics and Photonics (SPIE), for development of classes for students and workshops for the general public on photonics sciences, telecommunications and integrated photonics research, $2,432 USD, 2014.

University of Southampton Optoelectronics Research Centre and Faculty of Physical Sciences and the Environment, "From school classes to UNESCO," International Year of Light 2015 sponsorship and collaborative school trip with Thomas Hardye School to IYL 2015 opening ceremony, €5000 EUR, 2014.

- **Co-author**

"SPIE Education Outreach Grant", International Society for Optics and Photonics (SPIE), $3,779 USD, 2017.

"OSA Centennial Special Events Grant", Optical Society (OSA), $1,550 USD, 2015

"SPIE Education Outreach Grant", International Society for Optics and Photonics (SPIE), $3,024 USD, 2015

"IYL 2015 activity grant", IEEE Photonics Society, $900 USD, 2015

Invited papers and talks

M. T. Posner, P. V John, N. H. L. Wong, V. Mittal, and M. M. Nunez-Velazquez, "From school classes to UNESCO: IYL-enabled environments for tackling the STEM skills shortage through student-led outreach, (*Invited Paper*)" in *Proc. SPIE 9946*, pp.9946-6, 2016, (Oral presentation).

M. T. Posner, "*Reflecting photonics: RHS Tatton Park Flower Show*," Excellence with Engagement, Royal Society Outreach and Public Engagement Symposium, Chicheley Hall, Newport Pagnell, UK, 2016.

M. T. Posner, "*From heliographs to the internet: celebrating Light*," Salisbury Café Scientifique, Salisbury, UK, 2015.

M. T. Posner, "*Communicating with Light*," British Science Festival, in *Light: shaping the future*, Bradford, UK, 2015.

Conference proceedings

M. T. Posner, R. H. S Bannerman, D. H. Smith, P. L. Mennea, J. C. Gates, P. G. R. Smith, "High-birefringence direct-UV-written silica waveguides for heralded single-photon sources at telecom wavelengths," in *Conference on Lasers and Electro-Optics Europe (CLEO Europe)*, 2017 (Poster presentation).

B. Liu, C. Sima, B. Cai, Y. Gao, D. Liu, **M. T. Posner**, J. C. Gates, and P. G. R. Smith, "Design of continuously-tuneable photonic fractional Hilbert transformer based on a high birefringent planar Bragg grating," in *Conference on Lasers and Electro-Optics Pacific Rim (CLEO PR)*, 2017.

N. Podoliak, **M. T. Posner**, J. C Gates, P. G. R. Smith, and P. Horak "Optical beam splitting and switching based on arrays of tilted Bragg gratings in planar waveguides" in *Conference on Lasers and Electro-Optics Pacific Rim (CLEO PR)*, 2017.

M. T. Posner, A. Jantzen, L. D. Van Putten, A. Ravagli, A. L. Donko, N. Soper, N. H. L. Wong, and P. V. John, "Cathedral outreach: student-led workshops for school curriculum enhancement in non-traditional environments," in *Proc. SPIE 10452*, pp. 10452-07, 2017 (Oral presentation).

N. H. L. Wong, A. S. K. Tong, **M. T. Posner**, and A. Ravagli "Modular and extensible lesson on fiber optics for youths," in *Proc. SPIE 10452*, pp. 10452-14, 2017.

A. Jantzen, C. Holmes, S. G. Lynch, **M. T. Posner**, R. H. S. Bannerman, P. G. R. Smith, "Tilted Bragg gratings in integrated optical fiber," in *Photonics and Fiber Technology 2016 (ACOFT, BGPP, NP),* OSA Technical Digest (online) paper BT2B.2, 2016.

N. H. L. Wong, **M. T. Posner**, V. Mittal, D. R. Gray, and P. V John, "Taking local optics outreach abroad for IYL 2015: administrative and logistical challenges and strategies," in *SPIE 9946*, pp. 9946–14, 2016.

M. T. Posner, P. V John, D. Standen, N. V. Wheeler, L. D. van Putten, N. Soper, T. Parsonage, N. H. L. Wong, and G. Brambilla, "Reflecting photonics: Reaching new audiences through new partnerships: IYL 2015 and the Royal Horticultural Society flower show," in *Proc. SPIE 9946*, pp. 9946–2, 2016 (Oral presentation)

M. T. Posner, P. L. Mennea, N. Podoliak, P. Horak, J. C. Gates, and P. G. Smith, "Integrated polarizing coupler based on tilted gratings," in *Advanced Photonics 2016 (IPR, NOMA, Sensors, Networks, SPPCom, SOF)*, OSA technical Digest (online) (Optical Society of America, 2016), paper IW3B.3, 2016 (Oral presentation)

C. B. E Gawith, J. C. Gates, P. L. Mennea, L. G. Carpenter, S. Berry, C. Holmes, S. G. Lynch, **M. T. Posner**, R. H. S. Bannerman, M. Turvey, P. Cooper, and P. G. R. Smith, "Fabrication of integrated optical waveguides for use in new quantum technologies," in *International Conference on Photonics, 2016*

M. T. Posner, P. L. Mennea, N. Podoliak, P. Horak, J. C. Gates, and P. G. R. Smith, "45° tilted gratings for silica-based integrated polarizers," in *2015 European Conference on Lasers and Electro-Optics –European Quantum Electronics Conference*, (Optical Society of America, 2015), paper CE_10_5, 2015 (Oral presentation).

P. L. Mennea, B. J. Metcalf, J. B. Spring, A. E. Lita, B. Calkins, P. C. Humphries, T. J. Bartley, T. Gerrits, **M. T. Posner**, J. C. Gates, W. S. Kolthammer, S. W. Nam, I. A. Walmsley, and P. G. R. Smith, "UV-written Silica Waveguide devices for Integrated Quantum Optics," in *2015 European Conference on Lasers and Electro-Optics – European Quantum Electronics Conference*, (Optical Society of America, 2015), paper JSV_P_7, 2015.

N. H. L. Wong, **M. T. Posner**, and P. V. John, "The Lightwave Programme and Roadshow : An Overview and Update," in *Proc. SPIE 9793*, vol. 97932V, pp. 1–16, 2015.

M. T. Posner, P. L. Mennea, J. C. Gates, and P. G. R. Smith, "Tilted gratings for silica-based integrated polarising beam splitter –preliminary results," in *Zepler Institute Photonics Day*, Southampton, 2014. (Poster presentation)

P. G. R. Smith, J. C. Gates, C. Holmes, L. G. Carpenter, D. O. Kundys, P. L. Mennea, and **M. T. Posner**, "Integrated optical circuits for quantum information processing," in *International Conference on Optics & Optoelectronics (ICOL)*, 2014.

P. G. R. Smith, J. C. Gates, C. Holmes, L. G. Carpenter, D. O. Kundys, P. L. Mennea, and **M. T. Posner**, "At the Cross-Roads of Effective Quantum Information Processing with Integrated Optical Gates," in *Photonics North*, 2014.

P. L. Mennea, **M. T. Posner**, J. C. Gates, P. G. R. Smith, J. B. Spring, B. J. Metcalf, P. C. Humphries, M. Moore, W. S. Kolthammer, and I. A. Walmsley, "Engineering waveguide arrays for high-purity, matched, four-wave-mixing photon sources," in *17th European Conference. of Integrated Optics*, 2014.

Manuscripts in preparation

The following are titles of papers that are being drafted for publication, which stem from the work directly undertaken as part of this PhD thesis:

M. T. Posner, N. Podoliak, P. L. Mennea, P. Horak, P. G. R. Smith, J. C. Gates, "Integrated polarizer based on 45^0 tilted gratings."

M. T. Posner, T. Hiemstra, P. L. Mennea, A. Eckstein, W. S. Kolthammer, I. A. Walmsley, D. H. S. Smith, J. C. Gates, and P. G. R. Smith, "High-birefringence direct UV-written waveguides for heralded single-photon sources at telecoms wavelengths."

Appendix B Contribution list

Work has been undertaken throughout this project with other researchers from within this author's research group, the Optoelectronics Research Centre and researchers from other universities. The tables shown here highlight the contributions made by the author in collaborative activities. For Chapter 2, the table provided is to highlight the author's contribution to current fabrication systems.

Chapter 2	
Situation prior to this project	Author contribution
Physical micromachining using precision dicing and traditional lapping and chemical-mechanical polishing process.	Development of process for lapping and chemical-mechanical polishing using Allied High Tech Products Inc Multiprep equipment (Section 2.7), to speed up sample processing.

Chapter 3	
Brief outline of work	Author contribution
Modelling of polarising beam splitter (section 3.3.2).	Assisted with model design for waveguides and gratings. Modelling and analytical derivations carried out by Nina Podoliak.
Fabrication and characterisation of devices (sections 3.4 and 3.5).	Direct UV writing and grating characterisation. Wafer fabrication at ORC prior to the author's PhD study.

Chapter 4	
Brief outline of work	Author contribution
Modelling of polarising beam splitter (section 4.3.1).	Assisted with model design for waveguides and gratings. Modelling and analytical derivations carried out by Nina Podoliak.
Fabrication and characterisation of devices (sections 4.4 and 4.5).	Direct UV writing and grating characterisation. Wafer fabrication at ORC prior to the author's PhD study.

Chapter 5	
Brief outline of work	Author contribution
Fabrication and characterisation of high-birefringence wafers v1, v2 and v3.	Wafers v2 and v3 fabricated and characterised by this author. Wafers v1 previously fabricated the ORC.
DUW fabrication and characterisation of waveguides on wafers v1, v2 and v3.	Fabrication and characterisation conducted by the author
Waveguide and fibre optical mode profiling.	Waveguide mode profile of waveguide chips measured by this author. Fibre profile measurements results obtained by Rex H. S. Bannerman.
Numerical modelling and coupling efficiency simulations.	Photon Design FIMMWAVE model developed by the author. Matlab source code provided by James C. Gates and Paolo L. Mennea, and adapted by the author.

Chapter 6	
Brief outline of work	Author contribution
Measurement of horizontal and vertical misalignment offsets of commercial fibre v-groove arrays.	Design, implementation and testing of characterisation setup. Characterisation and analysis of all fibre v-groove arrays presented in Appendix D.

Chapter 7	
Brief outline of work	Author contribution
Reflecting Photonics Garden project design and delivery.	Production of documentation (flower cheat sheets). Design of experiments for science tent. Garden fabrication from project partners. Engaged with public over 2-day period with university research students (Tina Parsonage, Lieke van Putten, Nathan Soper) and Pearl John.
Reflecting Photonics evaluation.	Survey design by Pearl John. Data collection by author and research public engagement team. Survey data processing by Thomas Jefferson-Brain. Social media analysis by Deanna Standen.
Research-based school class activities.	Class and evaluation designed by author. Management of delivery (coordination with schools/project partners, team organisation, kit training, production of documentation, delivery, evaluation)

Appendix C Wafer Parameters

The wafers used to fabricate waveguides and grating-based devices described in this thesis have different chemical and physical properties having been produced by different recipes. This appendix presents the fabrication properties of each slab waveguide wafer prior to UV writing to compare layer composition with the optical behaviour observed.

All wafers in this thesis were fabricated at the University of Southampton's Optoelectronics Research Centre (ORC) using the same flame hydrolysis deposition system between 2011 and 2016. The gas flows presented here are pressure compensated with respect to the air pressure and humidity of the lab environment. The gas flows, shown here in standard cubic centimetres per minute (sscm), cannot be directly compared for the different precursors, as the pressure at operating temperature for each is different (see Chapter 2). However, as a means of comparison between different wafers, the presence of more or less gas flow can be interpreted as a greater or lesser amount of precursor reaching the torch.

The following pages give detailed fabrication parameters and slab waveguide properties of each wafer.

Wafer NB12/NB18 Fabricated at ORC			
Underclad	Shinetsu TY471/2, 16.5 µm thermal oxide		
Core	Date Deposition program Run number Wafer position **Average refractive index** **Average thickness**	14/06/11 075%CORE NB12 2 **1.4545** **5.1 µm**	
	Torch gas flows	H_2 O_2 Ar	3 1.9 8
	Process gas flow	$SiCl_4$ $GeCl_4$ PCl_3 BCl_3	143 177 - 25
	Furnace gas flow	He O_2	1.9 0.9
Overclad	Date Deposition program Run number Wafer position Average refractive index Average thickness	14/07/11 ORCLAD2A NB18 5 1.4447 18.1 µm	
	Torch gas flows	H_2 O_2 Ar	6.5 1.9 8
	Process gas flow	$SiCl_4$ $GeCl_4$ PCl_3 BCl_3	137 - 31 71
	Furnace gas flow	He O_2	1.9 -

Wafer NB231/NB232 Fabricated at ORC			
Underclad	Shinetsu 615-49-5002, 16.5 µm thermal oxide		
Core	Date Deposition program Run number Wafer position **Average refractive index** **Average thickness**	08/10/15 High-bi **V2** NB231 2 **1.4478** **3.6 µm**	
	Torch gas flows	H_2 O_2 Ar	5 5 8
	Process gas flow	$SiCl_4$ $GeCl_4$ PCl_3 BCl_3	141 31 - 27
	Furnace gas flow	He O_2	1.9 0.9
Overclad	Date Deposition program Run number Wafer position Average refractive index Average thickness	09/10/15 ORCLAD2A NB232 2 1.4447 18.1 µm	
	Torch gas flows	H_2 O_2 Ar	6.5 1.9 8
	Process gas flow	$SiCl_4$ $GeCl_4$ PCl_3 BCl_3	139 - 31 70
	Furnace gas flow	He O_2	1.9 -

Wafer NB236/NB237 Fabricated at ORC			
Underclad	Shinetsu 615-49-5002, 16.5 µm thermal oxide		
Core	Date Deposition program Run number Wafer position **Average refractive index** **Average thickness**	21/10/15 High-bi **V1** NB236 2 **1.4473** **5.0 µm**	
	Torch gas flows	H_2 O_2 Ar	5 5 8
	Process gas flow	$SiCl_4$ $GeCl_4$ PCl_3 BCl_3	140 35 - 40
	Furnace gas flow	He O_2	1.9 0.9
Overclad	Date Deposition program Run number Wafer position Average refractive index Average thickness	22/10/15 ORCLAD2A NB237 2 1.4447 18.1 µm	
	Torch gas flows	H_2 O_2 Ar	6.5 1.9 8
	Process gas flow	$SiCl_4$ $GeCl_4$ PCl_3 BCl_3	139 - 31 70
	Furnace gas flow	He O_2	1.9 -

Wafer NB241/NB242 Fabricated at ORC			
Underclad	Shinetsu 615-49-5002, 16.5 µm thermal oxide		
Core	Date Deposition program Run number Wafer position **Average refractive index** **Average thickness**	30/11/15 High-bi **V3** NB241 2 **1.4478** **5.1 µm**	
	Torch gas flows	H_2 O_2 Ar	5 5 8
	Process gas flow	$SiCl_4$ $GeCl_4$ PCl_3 BCl_3	140 29 - 20
	Furnace gas flow	He O_2	1.9 0.9
Overclad	Date Deposition program Run number Wafer position Average refractive index Average thickness	01/12/15 ORCLAD2A NB242 2 1.4447 18.1 µm	
	Torch gas flows	H_2 O_2 Ar	6.5 1.9 8
	Process gas flow	$SiCl_4$ $GeCl_4$ PCl_3 BCl_3	139 - 31 70
	Furnace gas flow	He O_2	1.9 -

Wafer NB284/NB287 Fabricated at ORC			
Underclad	Shinetsu 615-49-5002, 16.5 µm thermal oxide		
Core	Date Deposition program Run number Wafer position **Average refractive index** **Average thickness**	08/10/15 High-bi **V2** NB284 2 **1.4478** **4.2 µm**	
	Torch gas flows	H_2 O_2 Ar	5 5 8
	Process gas flow	$SiCl_4$ $GeCl_4$ PCl_3 BCl_3	141 31 - 27
	Furnace gas flow	He O_2	1.9 0.9
Overclad	Date Deposition program Run number Wafer position Average refractive index Average thickness	09/10/15 ORCLAD2A NB287 2 1.4447 18.1 µm	
	Torch gas flows	H_2 O_2 Ar	6.5 1.9 8
	Process gas flow	$SiCl_4$ $GeCl_4$ PCl_3 BCl_3	139 - 31 70
	Furnace gas flow	He O_2	1.9 -

Wafer NB285/NB287 Fabricated at ORC			
Underclad	Shinetsu 615-49-5002, 16.5 µm thermal oxide		
Core	Date Deposition program Run number Wafer position **Average refractive index** **Average thickness**	08/10/15 High-bi **V2** NB285 2 **1.4478** **5.2 µm**	
	Torch gas flows	H_2 O_2 Ar	5 5 8
	Process gas flow	$SiCl_4$ $GeCl_4$ PCl_3 BCl_3	141 31 - 27
	Furnace gas flow	He O_2	1.9 0.9
Overclad	Date Deposition program Run number Wafer position Average refractive index Average thickness	09/10/15 ORCLAD2A NB287 2 1.4447 18.1 µm	
	Torch gas flows	H_2 O_2 Ar	6.5 1.9 8
	Process gas flow	$SiCl_4$ $GeCl_4$ PCl_3 BCl_3	139 - 31 70
	Furnace gas flow	He O_2	1.9 -

Wafer NB286/NB287 Fabricated at ORC			
Underclad	Shinetsu 615-49-5002, 16.5 µm thermal oxide		
Core	Date Deposition program Run number Wafer position **Average refractive index** **Average thickness**	08/10/15 High-bi **V2** NB286 2 **1.4478** **6.0 µm**	
	Torch gas flows	H_2 O_2 Ar	5 5 8
	Process gas flow	$SiCl_4$ $GeCl_4$ PCl_3 BCl_3	141 31 - 27
	Furnace gas flow	He O_2	1.9 0.9
Overclad	Date Deposition program Run number Wafer position Average refractive index Average thickness	09/10/15 ORCLAD2A NB287 2 1.4447 18.1 µm	
	Torch gas flows	H_2 O_2 Ar	6.5 1.9 8
	Process gas flow	$SiCl_4$ $GeCl_4$ PCl_3 BCl_3	139 - 31 70
	Furnace gas flow	He O_2	1.9 -

Wafer NB88/NB90 Fabricated at ORC			
Underclad	TY470-2, 16.5 µm thermal oxide		
Core	Date Deposition program Run number Wafer position **Average refractive index** **Average thickness**	11/12/12 LOW LOSS V3 NB88 2 **1.445** **4.8 µm**	
	Torch gas flows	H_2 O_2 Ar	5 5 8
	Process gas flow	$SiCl_4$ $GeCl_4$ PCl_3 BCl_3	142 43 - 61
	Furnace gas flow	He O_2	1.9 0.9
Overclad	Date Deposition program Run number Wafer position Average refractive index Average thickness	19/12/12 LOWLOSS NB102 2 1.4447 18.1 µm	
	Torch gas flows	H_2 O_2 Ar	6.5 1.5 8
	Process gas flow	$SiCl_4$ $GeCl_4$ PCl_3 BCl_3	136 - 31 69
	Furnace gas flow	He O_2	1.9 -

Wafer NB100/NB102 Fabricated at ORC			
Underclad	TY470-2, 16.5 µm thermal oxide		
Core	Date Deposition program Run number Wafer position **Average refractive index - 633nm** **Average thickness**	31/05/2013 HIBI**V1** NB100 2 **1.446** **4.9 µm**	
	Torch gas flows	H_2 O_2 Ar	5 5 8
	Process gas flow	$SiCl_4$ $GeCl_4$ PCl_3 BCl_3	140 40 - 35
	Furnace gas flow	He O_2	1.9 0.9
Overclad	Date Deposition program Run number Wafer position Average refractive index Average thickness	06/06/2013 ORCCLAD2A NB102 3 1.4447 18.1 µm	
	Torch gas flows	H_2 O_2 Ar	6.5 1.9 8
	Process gas flow	$SiCl_4$ $GeCl_4$ PCl_3 BCl_3	137 - 31 70
	Furnace gas flow	He O_2	1.9 -

Appendix D V-groove measurement details

This appendix provides detail of the horizontal, vertical and radial offsets and losses caused by misalignment that were presented in Chapter 6. The offset positions have been stated relative to the "ideal" position of ports on the device. The loss, α, has been calculated using equation (6.1), where u and ω refer to the fibres' offset position and mode field diameter, respectively. The drift for each device scanned has been measured from calculating the deviation in measured fibre position of the same fibre at the start and end of the scan. The reader is referred to sections 6.4 and 6.5 for detailed discussion on the calibration of the measurement system and calculation method of the offset value.

$$\alpha\ (dB) = 4.34 \left(\frac{u}{\omega}\right)^2 \qquad \textbf{(6.1)}$$

Fibre v-groove arrays have been sourced from two suppliers: OzOptics and SQS Fibre. The nomenclature for each supplier is, respectively, Oz-N-X-λ and SQS-N-X-λ, where '*N*' refers to the number of ports, '*X*' is an arbitrary numbering to the device under test, and λ the operating wavelength. V-groove fibre arrays at operating wavelengths near 1550 nm were already available at the University of Southampton's Optoelectronics Research Centre. The v-grooves fibre arrays for operating wavelengths near 800 nm have been provided by collaborators from the University of Oxford. The devices' specified radial offset has been indicated when available.

A.1 V-groove fibre arrays measurements for wavelengths near 1550 nm

		Measurements									***Spec sheet***	
Device	*Port*	Horizontal (x-axis)			Vertical (y-axis)			Radial offset			Radial offset	
		Offset (µm)	Loss (dB)	Drift (µm)	Offset (µm)	Loss (dB)	Drift (µm)	Offset (µm)	Loss (dB)	Drift (µm)	Offset (µm)	Loss (dB)
Oz-4-1 -1550	1	Ref	\	0.030	0.055	0.0001	0.028	0.055	0.0001	0.041	0.500	0.0100
	2	0.200	0.0016		-0.050	0.0001		0.206	0.0017			
	3	0.256	0.0026		-0.061	0.0001		0.263	0.0028			
	4	0.445	0.0080		0.056	0.0001		0.449	0.0081			
Oz-4-2 -1550	1	Ref	0.0000	0.021	0.040	0.0001	0.016	0.040	0.0001	0.026	0.500	0.0100
	2	0.288	0.0033		-0.067	0.0002		0.296	0.0035			
	3	0.193	0.0015		0.016	0.0000		0.194	0.0015			
	4	0.426	0.0073		0.011	0.0000		0.426	0.0073			
Oz-4-3 -1550	1	Ref	\	0.027	0.000	0.0000	0.030	0.000	0.0000	0.040	0.500	0.0100
	2	0.063	0.0002		0.031	0.0000		0.070	0.0002			
	3	0.001	0.0000		0.063	0.0002		0.063	0.0002			
	4	0.393	0.0062		-0.033	0.0000		0.394	0.0062			
Oz-4-4 -1550	1	Ref	\	0.034	-0.238	0.0023	0.027	0.238	0.0023	0.044	0.500	0.0100
	2	-0.453	0.0082		0.578	0.0134		0.734	0.0216			
	3	-0.244	0.0024		0.129	0.0007		0.276	0.0031			
	4	0.243	0.0024		-0.470	0.0089		0.529	0.0112			
SQS-4-1 -1550	1	Ref	\	0.021	-0.160	0.0010	0.013	0.160	0.0010	0.025	0.480	0.0092
	2	0.389	0.0061		0.060	0.0001		0.394	0.0062		0.450	0.0081
	3	0.328	0.0043		0.381	0.0058		0.502	0.0101		0.640	0.0164
	4	0.270	0.0029		-0.280	0.0032		0.389	0.0061		0.640	0.0164

A.2 V-groove fibre arrays measurements for wavelengths near 800 nm

4-port fibre v-groove arrays

The average radial offset $\overline{r_1}$ and $\overline{r_2}$, for devices SQS-4-1 and SQS-4-2 as $\overline{r_1} = 780 \pm 410\ nm$ and $\overline{r_2} = 697 \pm 333\ nm$. The stated error is the standard deviation of the measurements, which has been found to be significantly higher than the drift. The corresponding misalignment tolerances, $\overline{r_{S1}}$ and $\overline{r_{S2}}$, specified by the manufacturer for these two devices have been calculated as $\overline{r_{S1}} = 738 \pm 359\ nm$ and $\overline{r_{S2}} = 645 \pm 165\ nm$. Full details of horizontal, vertical, radial obtained by measurements, as well as the specified offsets, and the associated losses have been presented in the following table.

		Measurements									***Spec sheet***	
Device	*Port*	Horizontal (x-axis)			Vertical (y-axis)			Radial offset			Radial offset	
		Offset (µm)	Loss (dB)	Drift (µm)	Offset (µm)	Loss (dB)	Drift (µm)	Offset (µm)	Loss (dB)	Drift (µm)	Offset (µm)	Loss (dB)
SQS-4-1 -800 1200730179	1	Ref	\	0.025	-0.474	0.032	0.054	0.474	0.032	0.060	0.950	0.129
	2	-0.638	0.058		1.230	0.217		1.386	0.275		0.980	0.138
	3	-0.584	0.049		-0.196	0.006		0.616	0.054		0.210	0.006
	4	0.321	0.015		-0.421	0.025		0.529	0.040		0.810	0.094
SQS-4-2 -800 1200730180	1	Ref	\	0.025	-0.350	0.018	0.058	0.350	0.018	0.063	0.470	0.032
	2	-0.232	0.008		0.421	0.025		0.481	0.033		0.540	0.042
	3	0.414	0.025		0.831	0.099		0.929	0.124		0.770	0.085
	4	-0.497	0.035		-0.903	0.117		1.031	0.152		0.800	0.092

10-port fibre v-groove array

		Experimental								
Device	*Port*	Horizontal (x-axis)			Vertical (y-axis)			Radial offset		
		Offset (μm)	Loss (dB)	Drift (μm)	Offset (μm)	Loss (dB)	Drift (μm)	Offset (μm)	Loss (dB)	Drift (μm)
SQS-10-1-800	1	Ref	\	0.066	-0.070	0.0007	0.068	0.070	0.0007	0.095
	2	-0.413	0.0244		0.168	0.0041		0.446	0.0285	
	3	0.146	0.0030		-0.151	0.0033		0.210	0.0063	
	4	0.111	0.0018		0.130	0.0024		0.171	0.0042	
	5	-0.200	0.0057		-0.001	0.0000		0.200	0.0057	
	6	-0.150	0.0032		-0.151	0.0033		0.212	0.0065	
	7	-0.225	0.0073		0.020	0.0001		0.226	0.0073	
	8	-0.160	0.0037		0.030	0.0001		0.163	0.0038	
	9	0.079	0.0009		0.024	0.0001		0.082	0.0010	
	10	0.034	0.0002		-0.207	0.0061		0.209	0.0063	

Appendix E Teaching plans

This appendix presents example lesson plans for classes developed throughout this thesis.

Workshops have been developed on the themes of photonics science and research for classroom-based interaction with students aged 8-14 years of age (key stages 2 and 3 of the UK national curriculum). These classes complement the relevant areas of the science national curriculum. The reader is referred to section 7.3 for the associated discussion.

The Secrets of light, Key Stage 2 (Years 5-6)

Title	**The secrets of light**

Outcomes/objectives

At the end of the session the pupils will be able to do the following

a) Explain that white light is made of different colours and be able to name the three primary colours of light.
b) Recognise different type or mirrors and be able to name planar, convex and concave mirrors; also use the idea that light travels in a straight line to explain why shapes can be deformed with different types of mirrors.
c) Send a simple message using light and Morse code.
d) Identify that 2015 is the International Year of Light.

Overview:

The class will be divided into 3 workshops containing hands-on practical experiments on mirrors and lenses, the electromagnetic spectrum and telecommunications.

The students will be split into groups (3) to maximise experimental work and contact time with demonstrations.

Activities included: *(35 minutes)*

Introduction

- University: "a big school for adults to study at"; science, sports, English, languages, teaching.
- Introduction to the class and divide class into smaller groups (5 minutes)
    - Light from the sun is dangerous

Workshops: 7-8 minutes each, x3 (21-24 minutes)

a) Electromagnetic spectrum

Talk about different types of light that exist (UV, visible, infrared). Use a white light source to demonstrate that white light can be split into different colours. Use filters to block out light from a white light source and prisms to split light. Use colour spinners to show that white light is made by mixing all the different colours. Quiz students about the primary colours of light.

b) Mirrors, lenses and reflection

Talk about mirrors and reflection: angle of incidence=angle of reflection for planar mirrors. Demonstrate this using periscope. Ask the pupils to complete the pictures using the mirrors.
Demonstrate planer, convex and concave mirrors. See if they can use the bendy mirrors to make themselves as ugly as possible!

c) Telecommunications

Experiments: Morse code machine. Use flash torches and worksheet handouts to send messages to friends through pipes. Show how a message can be guided in plastic using Perspex rods.
Plenary demonstration (2 minutes):
Tyndall-Colladon experiment: use a red laser light to send a message (SOS) through a water fountain using total internal reflection.
Conclusion and quiz (5 mins)

Plenary: Participation throughout the session will be encouraged to address all learning points; questions will be asked during the experimental demonstrations. A short quiz will be given to students at the end of the class with a marking sheet for the teachers.	
Kit a) Electromagnetic spectrum Light Box and Filters Colour spinners UV Lamps b) Mirrors and Reflections Periscope Bendable Mirrors Box Mirror Maze Lenses c) Telecommunications Torches and pipes. Morse code circuit. d) Tyndall-Colladon experiment Laser pointer, batteries Tyndall aquarium, tap bits, collection bucket. Table clothes: x4-5	
Evaluation:	Students to complete event evaluation quiz and survey

Communicating with Light[2], Key Stage 3 (Years 7-8)

Title	**Communicating with Light**

Outcomes and teaching objectives:
At the end of the workshop the participants will be able to do the following: -

1. Identify that 2015 is the International Year of Light.
2. Send messages using Morse Code, explain pros and cons of this technique and describe ways to overcome limitations of free space communications
3. Recognise total internal reflection.
4. Name what optical fibres are most commonly made of.
5. Recognise one research applications carried out at the University of Southampton.

Overview:

The workshop aims to introduce students to the field of photonics and demonstrate how light can be used as a communication method.

We will start the class by relating communication to their everyday lives and challenge them to think about what they know that may enable them the freedom of communication they enjoy today (fibre optics, internet, etc.)

We will introduce the concept of lasers and fibre optics and discuss how these are used to transmit data.

The workshop will then feature a practical "light coding" session where the students will be asked to use Morse code to transmit and receive messages using flash torches to their peers. A discussion will follow to highlight the pros and cons of the scheme.

We will run a couple of experimental demonstrations to address teaching objectives 1 and 3, followed by a short clip on making optical fibres.

At the end of the session, the postgraduate researchers will be given an opportunity to present their research to the students.

Key words

- Photonics
- Lasers.
- Optical fibres.
- Total internal reflection

[2] Developed independently from the highly acclaimed version for adults presented by Prof. P. Bayvel at the Royal Society in 2014 [175]

Activities included:

Total time 60-70 mins

- Introduction –*10 minutes*

Introduce demonstrators
Outline session plan
Ask who has heard of the IYL 2015.
Show IYL video
Start presentation.

Teaching objective 1

- Activity 1 – Light Morse code – *12-15 minutes*

Divide class into groups of 4 or 5 pupils and use work sheets to get them to send messages using Morse code.
Get class back together and discuss pros and cons of this method, writing responses down on the white board.

Teaching objective 2

- Split class into 2 groups and alternate between two experiments, 20 minutes max total
  - Experiment 1 – Communicating video with laser light –*5-10 minutes*

Teaching objective 2

  - Experiment 2 – Tyndall experiment and total internal reflection– *5-10 minutes*

Teaching objective 3

- Return to class and describe total internal reflection using ray diagrams –*3 minutes*

Teaching objective 3

- Optical fibres –

Introduce optical fibres and pass around the real fibres for the students to see.

- Making fibres – 5 minutes

Screen discovery Channel video – show how a fibre is drawn (*1-minute max*) – https://www.youtube.com/watch?v=N0x4KcnuLn4#t=145

Teaching objective 4

- Research at the Optoelectronics Research Centre 10-*12 minutes*

Each demonstrator gets 3-4 minutes to talk about their research and answer questions from students.

Teaching objective 5

- Conclusions and quiz (10 mins)

Plenary:

The session will end with the session leader linking the topics covered to some of the work carried out at the University of Southampton.

Participation throughout the session will be encouraged to address all learning points; questions will be asked during the experimental demonstrations.

A short questionnaire will be given to students at the end of the class with a marking sheet for the teachers.

Evaluation:	Students to complete event evaluation quiz and survey

References

[1] Commission of the European Communities, "Preparing for our future: Developing a common strategy for key enabling technologies in the EU," 2009. [Online]. Available: http://eur-lex.europa.eu/legal-content/EN/TXT/PDF/?uri=CELEX:52009DC0512&from=EN. [Accessed: 18-Sep-2017].

[2] T. H. Maiman, "Stimulated Optical Radiation in Ruby," *Nature*, vol. 187, no. 4736, pp. 493–494, Aug. 1960.

[3] The Optical Society, *OSA Century of Optics*. 2015.

[4] S. E. Miller, "Integrated Optics: An Introduction," *Bell Syst. Tech. J.*, vol. 48, no. 7, pp. 2059–2069, Sep. 1969.

[5] S. P. Watts, "Flame hydrolysis deposition of photosensitive silicate layers for the de finition of waveguiding structures through direct ultraviolet writing," *Thesis*, 2002.

[6] G. D. Emmerson, "Novel direct UV written devices," *Thesis*, 2003.

[7] C. Sima, "Integrated planar Bragg grating devices for advanced optical communications systems," *Thesis*, 2013.

[8] H. L. Rogers, "UV-written Bragg gratings for waveguide characterisation and advanced applications," *Thesis*, 2013.

[9] P. G. R. Smith, R. Williams, V. Albanis, C. Gawith, S. Watts, and G. Emmerson, "Fabrication of waveguides and bragg gratings with UV-irradiation," *Patent US20060127024 A1*, 2006.

[10] G. D. Emmerson, C. B. E. Gawith, and P. G. R. Smith, "Optical sensors for sensing the refractive index of fluid samples," *Patent US7541573 B2*, 2009.

[11] J. P. Dowling and G. J. Milburn, "Quantum technology : the second quantum revolution," *Phil. Trans. R. Soc. Lond. A*, vol. 361, pp. 1655–1674, 2003.

[12] N. Gisin and R. Thew, "Quantum communication," *Nat. Photonics*, no. 1, pp. 165–171, 2007.

[13] C. L. Degen, F. Reinhard, and P. Cappellaro, "Quantum sensing," *Rev. Mod. Phys.*, vol. 89, no. 3, pp. 35002-1-35002–39, Jul. 2017.

[14] T. D. Ladd, F. Jelezko, R. Laflamme, Y. Nakamura, C. Monroe, and J. L. O'Brien, "Quantum computers.," *Nature*, vol. 464, no. 7285, pp. 45–53, Mar. 2010.

[15] J. L. O'Brien, A. Furusawa, and J. Vučković, "Photonic quantum technologies," *Nat. Photonics*, vol. 3, no. 12, pp. 687–695, 2010.

[16] E. Knill, R. Laflamme, and G. J. Milburn, "A scheme for effcient quantum computation with linear optics," *Nature*, vol. 409, pp. 46–52, 2001.

[17] A. Aaronson and A. Arkhipov, "The computational complexity of linear optics," in *Proc. 43rd Annual ACM Symposium on the Theory of Computing*, 2011, pp. 333–342.

[18] J. L. O. Brien, "Optical Quantum Computing," *Science*, vol. 318, no. 5856, pp. 1567–1571, 2007.

[19] J. B. Spring, "Single photon generation and quantum computing with integrated photonics," *Thesis*, 2014.

[20] S. Tanzilli, A. Martin, F. Kaiser, M. P. De Micheli, O. Alibart, and D. B. Ostrowsky, "On the genesis and evolution of Integrated Quantum Optics," *Laser Photon. Rev.*, vol. 6, no. 1, pp. 115–143, Jan. 2012.

[21] R. Nagarajan, M. Kato, J. Pleumeekers, P. Evans, S. Corzine, S. Hurtt, A. Dentai, S. Murthy, M. Missey, R. Muthiah, R. A. Salvatore, C. Joyner, R. Schneider, M. Ziari, F. Kish, and D. Welch, "InP Photonic Integrated Circuits," *IEEE J. Sel. Top. Quantum Electron.*, vol. 16, no. 5, pp. 1113–1125, Sep. 2010.

[22] G. Reed, W. Headley, and C. Png, "Silicon photonics: the early years," in *Proc. SPIE 5730*, 2005, p. 596921.

[23] R. Soref, "The Past, Present, and Future of Silicon Photonics," *IEEE J. Sel. Top. Quantum Electron.*, vol. 12, no. 6, pp. 1678–1687, Nov. 2006.

[24] M. G. Thompson, A. Politi, J. C. F. Matthews, and J. L. O'Brien, "Integrated waveguide circuits for optical quantum computing," *IET Circuits, Devices Syst.*, vol. 5, no. 2, pp. 94–102, Mar. 2011.

[25] A. Politi, M. J. Cryan, J. G. Rarity, S. Yu, and J. L. O'Brien, "Silica-on-Silicon Waveguide Quantum Circuits," *Science*, vol. 320, no. 5876, pp. 646–649, 2008.

[26] A. Crespi, R. Ramponi, R. Osellame, L. Sansoni, I. Bongioanni, F. Sciarrino, G. Vallone, and P. Mataloni, "Integrated photonic quantum gates for polarization qubits," *Nat. Commun.*, vol. 2, pp. 566–572, 2011.

[27] B. J. Smith, D. Kundys, N. Thomas-Peter, P. G. R. Smith, and I. A. Walmsley, "Phase-controlled integrated photonic quantum circuits," *Opt. Express*, vol. 17, no. 16, pp. 264–267, 2009.

[28] J. B. Spring, B. J. Metcalf, P. C. Humphreys, S. W. Kolthammer, X. M. Jin, M. Barbieri, A. Datta, N. Thomas-Peter, N. K. Langford, D. Kundys, J. C. Gates, B. J. Smith, P. G. R. Smith, and I. A. Walmsley, "Boson Sampling on a Photonic Chip," *Science*, vol. 339, no. 6121, pp. 798–801, 2013.

[29] B. J. Metcalf, J. B. Spring, P. C. Humphreys, N. Thomas-Peter, M. Barbieri, W. S. Kolthammer, X. Jin, N. K. Langford, D. Kundys, J. C. Gates, B. J. Smith, P. G. R. Smith, and I. A. Walmsley, "Quantum teleportation on a photonic chip," *Nat. Photonics*, vol. 8, pp. 770–774, 2014.

[30] J. B. Spring, P. L. Mennea, B. J. Metcalf, P. C. Humphreys, J. C. Gates, H. L. Rogers, C. Söller, B. J. Smith, W. S. Kolthammer, P. G. R. Smith, and I. A. Walmsley, "Chip-based array of near-identical, pure, heralded single-photon sources," *Optica*, vol. 4, no. 1, pp. 90–96, 2017.

[31] B. Calkins, P. L. Mennea, A. E. Lita, J. Benjamin, W. S. Kolthammer, A. Lamas-linares, B. Justin, P. C. Humphreys, R. P. Mirin, J. C. Gates, P. G. R. Smith, I. A. Walmsley, T. Gerrits, and S. W. Nam, "High quantum-efficiency photon-number-resolving detector for photonic on-chip information processing," *Opt. Express*, vol. 21, no. 19, pp. 22657–22670, 2013.

[32] J. Wilson and J. Hawkes, “Chapter 8 - Optical fiber waveguides,” in *Optoelectronics: an introduction*, 1998, pp. 359–427.

[33] J. M. Senior, “Chapter 5 - Optical fiber connections: joints, couplers and isolators,” in *Optical fiber communications: principles and practice*, 2009, pp. 217–293.

[34] A. K. Ghatak and K. Thyagarajan, “Chapter 8 - Propagation characteristics of a step index fiber,” in *Introduction to Fiber Optics*, 1st ed., Cambridge University Press, Ed. Cambridge, 1998, pp. 97–124.

[35] A. Ghatak and K. Thyagarajan, “Introduction to Fiber Optics,” 1st ed., Cambridge University Press, Ed. Cambridge, 1998.

[36] K. Okamoto, *Fundamentals of Optical Waveguides*, 2nd ed. 2006.

[37] K. Okamoto, “Chapter 2 - Planar Optical Waveguides,” in *Fundamentals of Optical Waveguides*, 2nd ed., 2006, pp. 13–56.

[38] K. Okamoto, “Chapter 6 - Finite Element Method,” in *Fundamentals of Optical Waveguides*, 2nd ed., 2006, pp. 261–328.

[39] W. Souder and P. Hidnert, “Measurements on the thermal expansion of fused silica,” *Sci. Pap. Bur. Stand.*, vol. 21, p. 1, Sep. 1925.

[40] Y. Okada and Y. Tokumaru, “Precise determination of lattice parameter and thermal expansion coefficient of silicon between 300 and 1500 K,” *J. Appl. Phys.*, vol. 56, no. 2, pp. 314–320, 1984.

[41] M. Huang, “Thermal stresses in optical waveguides,” *Opt. Lett.*, vol. 28, no. 23, pp. 2327–2329, Dec. 2003.

[42] G. E. McGuire, “Semiconductor materials and process tehnology handbook: for Very Large Scale Integration (VLSI) and Ultra Large Scale Integration (ULSI),” 1998, pp. 48–57.

[43] S. Sudo, M. Kawachi, T. Edahiro, T. Izawa, T. Shioda, and H. Gotoh, “Low-OH-content optical fibre fabricated by vapour-phase axial-deposition method,” *Electron. Lett.*, vol. 14, no. 17, pp. 534–535, Aug. 1978.

[44] M. Blankenship and C. Deneka, “The outside vapor deposition method of fabricating optical waveguide fibers,” *IEEE J. Quantum Electron.*, vol. 18, no. 10, pp. 1418–1423, Oct. 1982.

[45] J. R. Bautista and R. M. Atkins, “The formation and deposition of SiO2 aerosols in optical fiber manufacturing torches,” *J. Aerosol Sci.*, vol. 22, no. 5, pp. 667–675, Jan. 1991.

[46] S. Sakaguchi, “Consolidation of silica glass soot body prepared by flame hydrolysis reaction,” *J. Non. Cryst. Solids*, vol. 171, no. 3, pp. 249–258, Aug. 1994.

[47] B. G. Bagley, C. R. Kurkjian, J. W. Mitchell, G. E. Peterson, and A. R. Tynes, “Chapter 7 – Materials, Properties, and Choices,” in *Optical Fiber Telecommunications*, 1979, pp. 167–231.

[48] D. L. Williams, B. J. Ainslie, J. Armitage, R. Kashyap, and R. Campbell, “Enhanced UV photosensitivity in boron codoped germanosilicate fibres,”

Electron. Lett., vol. 29, no. 1, pp. 45–47, 1993.

[49] P. K. Tien, "Light Waves in Thin Films and Integrated Optics," *Appl. Opt.*, vol. 10, no. 11, pp. 2395–2413, Nov. 1971.

[50] M. Svalgaard, "Ultraviolet light induced refractive index structures in germanosilica," *Thesis*, 1995.

[51] M. Svalgaard, C. V. Poulsen, O. Poulsen, and A. Bjarklev, "Direct UV writing of buried singlemode channel waveguides in Ge-doped silica films," *Electron. Lett.*, vol. 30, no. 17, pp. 1401–1403, Aug. 1994.

[52] M. Douay, W. X. Xie, T. Taunay, P. Bernage, P. Niay, P. Cordier, B. Poumellec, L. Dong, J. F. Bayon, H. Poignant, and E. Delevaque, "Densification involved in the UV-based photosensitivity of silica glasses and optical fibers," *J. Light. Technol.*, vol. 15, no. 8, pp. 1329–1342, Aug. 1997.

[53] K. O. Hill, Y. Fujii, D. C. Johnson, and B. S. Kawasaki, "Photosensitivity in optical fiber waveguides: Application to reflection filter fabrication," *Appl. Phys. Lett.*, vol. 32, no. 10, pp. 647–649, 1978.

[54] D. K. W. Lam and B. K. Garside, "Characterization of single-mode optical fiber filters," *Appl. Opt.*, vol. 20, no. 3, pp. 440–445, Feb. 1981.

[55] D. P. Hand and P. S. J. Russell, "Photoinduced refractive-index changes in germanosilicate fibers," *Opt. Lett.*, vol. 15, no. 2, pp. 102–104, 1990.

[56] D. L. Williams, S. T. Davey, R. Kashyap, J. R. Armitage, and B. J. Ainslie, "Direct observation of UV induced bleaching of 240 nm absorption band in photosensitive germanosilicate glass fibres," *Electron. Lett.*, vol. 28, no. 4, pp. 369–371, Feb. 1992.

[57] P. J. Lemaire, R. M. Atkins, V. Mizrahi, and W. A. Reed, "High pressure H2 loading as a technique for acheiving ultrahigh UV photosensitivity and thermal sensivity in GeO2 doped optical fibres," *Electron. Lett.*, vol. 29, no. 13, pp. 1191–1193, 1993.

[58] J. Stone, "Interactions of hydrogen and deuterium with silica optical fibers: A review," *J. Light. Technol.*, vol. 5, no. 5, pp. 712–733, May 1987.

[59] D. O. Kundys, J. C. Gates, S. Dasgupta, C. B. E. Gawith, and P. G. R. Smith, "Use of Cross-Couplers to Decrease Size of UV Written Photonic Circuits," *IEEE Photonics Technol. Lett.*, vol. 21, no. 13, pp. 947–949, Jul. 2009.

[60] W. W. Morey, G. Meltz, and W. H. Glenn, "Holographically generated gratings in optical fibers," *Opt. Photon. News*, vol. 1, no. 7, pp. 14–16, 1990.

[61] M. J. Cole, W. H. Loh, R. I. Laming, M. N. Zervas, and S. Barcelos, "Moving fibre/phase mask-scanning beam technique for enhanced flexibility in producing fibre gratings with uniform phase mask," *Electron. Lett.*, vol. 31, no. 17, pp. 1488–1490, Aug. 1995.

[62] A. Asseh, H. Storoy, B. E. Sahlgren, S. Sandgren, and R. A. H. Stubbe, "A writing technique for long fiber Bragg gratings with complex reflectivity profiles," in *Journal of Lightwave Technology*, vol. 15, no. 8, 1997, pp. 1419–1423.

[63] I. Petermann, B. Sahlgren, S. Helmfrid, A. T. Friberg, and P.-Y. Fonjallaz, "Fabrication of advanced fiber Bragg gratings by use of sequential writing

with a continuous-wave ultraviolet laser source," *Appl. Opt.*, vol. 41, no. 6, pp. 1051–1056, Feb. 2002.

[64] G. D. Emmerson, S. P. Watts, C. B. E. Gawith, V. Albanis, M. Ibsen, R. B. Williams, and P. G. R. Smith, "Fabrication of directly UV-written channel waveguides with simultaneously defined integral Bragg gratings," *Electron. Lett.*, vol. 38, no. 24, pp. 1531–1532, 2002.

[65] K. Sugden and V. Mezentsev, "Fiber Bragg gratings: advances in fabrication process and tools," in *Fiber Bragg grating sensors: recent advancements, industrial applications and market exploitation*, 2011, pp. 9–34.

[66] F. G. Smith, T. A. King, and D. Wilkins, "Chapter 11 - The diffraction grating and its applications," in *Optics and Photonics: an introduction*, 2nd ed., 2007, pp. 259–280.

[67] T. Erdogan, "Fiber grating spectra," *J. Light. Technol.*, vol. 15, no. 8, pp. 1277–1294, 1997.

[68] A. K. Ghatak and K. Thyagarajan, "Chapter 21 - Periodic interactions in waveguides," in *Introduction to Fiber Optics*, 1st ed., C. U. Press, Ed. Cambridge, 1998, pp. 452–479.

[69] T. Erdogan and J. E. Sipe, "Tilted fiber phase gratings," *J. Opt. Soc. Am. A*, vol. 13, no. 2, pp. 296–313, Feb. 1996.

[70] G. Meltz, W. W. Morey, and W. H. Glenn, "In-fiber Bragg grating tap," in *Optical Fiber Communication Conference*, 1990, vol. 1169, no. 1989, p. 6108.

[71] J. Wagener and T. Strasser, "Fiber grating optical spectrum analyzer tap," *ECOC 97*, no. 448, pp. 65–68, 1997.

[72] C. K. Madsen, J. Wagener, T. A. Strasser, D. Muehlner, M. A. Milbrodt, E. J. Laskowski, and J. Demarco, "Planar Waveguide Optical Spectrum Analyzer Using a UV-Induced Grating," *IEEE J. Sel. Top. quantum Electron.*, vol. 4, no. 6, pp. 925–929, 1998.

[73] J. Albert, L.-Y. Shao, and C. Caucheteur, "Tilted fiber Bragg grating sensors," *Laser Photon. Rev.*, vol. 7, no. 1, pp. 83–108, Jan. 2013.

[74] T. Guo, F. Liu, B.-O. Guan, and J. Albert, "[INVITED] Tilted fiber grating mechanical and biochemical sensors," *Opt. Laser Technol.*, vol. 78, pp. 19–33, Apr. 2016.

[75] C. Holmes, L. G. Carpenter, H. L. Rogers, I. J. G. Sparrow, J. C. Gates, and P. G. R. Smith, "Planar waveguide tilted Bragg grating refractometer fabricated through physical micromachining and direct UV writing.," *Opt. Express*, vol. 19, no. 13, pp. 12462–12468, Jun. 2011.

[76] C. Holmes, K. R. Daly, I. J. G. Sparrow, J. C. Gates, G. D'Alessandro, and P. G. R. Smith, "Excitation of Surface Plasmons Using Tilted Planar-Waveguide Bragg Gratings," *IEEE Photonics J.*, vol. 3, no. 5, pp. 777–788, Oct. 2011.

[77] C. Holmes, H. L. Rogers, K. R. Daly, L. G. Carpenter, C. Sima, P. L. Mennea, J. C. Gates, G. D'Alessandro, and P. G. R. Smith, "Tilted planar Bragg grating refractometers," in *2013 Conference on Lasers Electro-Optics Europe International Quantum Electronics Conference CLEO EUROPE/IQEC*, 2013, p. 1.

[78] C. Holmes, J. C. Gates, L. G. Carpenter, H. L. Rogers, R. M. Parker, P. a Cooper, S. Chaotan, F. R. Mahamd Adikan, C. B. E. Gawith, and P. G. R. Smith, "Direct UV-written planar Bragg grating sensors," *Meas. Sci. Technol.*, vol. 26, no. 11, p. 112001, Nov. 2015.

[79] G. Nemova, J. Chauve, and R. Kashyap, "Design of sidetap fiber Bragg grating filters," *Opt. Commun.*, vol. 259, pp. 649–654, 2006.

[80] K. Zhou, L. Zhang, X. Chen, and I. Bennion, "Low thermal sensitivity grating devices based on ex-45 degree tilting structure capable of forward-propagating cladding modes coupling," *J. Light. Technol.*, vol. 24, no. 12, pp. 5087–5094, 2006.

[81] G. Lepert, M. Trupke, E. A. Hinds, H. Rogers, J. C. Gates, and P. G. R. Smith, "Demonstration of UV-written waveguides, Bragg gratings and cavities at 780 nm, and an original experimental measurement of group delay," *Opt. Express*, vol. 19, no. 25, pp. 24933–24943, Dec. 2011.

[82] H. L. Rogers, C. Holmes, K. R. Daly, L. G. Carpenter, J. C. Gates, G. D'Alessandro, and P. G. R. Smith, "Tilted Bragg grating based optical components within an integrated planar platform," in *Proc. SPIE 8627*, 2013, pp. 8627-8627–6.

[83] J. Wilson and J. Hawkes, "Chapter 3 - Modulation of Light," in *Optoelectronics: an introduction*, 3rd ed., 1998, pp. 90–128.

[84] C. Sima, J. C. Gates, H. L. Rogers, P. L. Mennea, C. Holmes, M. N. Zervas, and P. G. R. Smith, "Ultra-wide detuning planar Bragg grating fabrication technique based on direct UV grating writing with electro-optic phase modulation," *Opt. Express*, vol. 21, no. 13, pp. 15747–15754, 2013.

[85] C. Sima, J. C. Gates, H. L. Rogers, P. L. Mennea, C. Holmes, M. N. Zervas, and P. G. R. Smith, "Phase controlled integrated interferometric single-sideband filter based on planar Bragg gratings implementing photonic Hilbert transform," *Opt. Lett.*, vol. 38, no. 5, pp. 727–729, Mar. 2013.

[86] H. L. Rogers, S. Ambran, C. Holmes, J. C. Gates, and P. G. R. Smith, "In situ loss measurement of direct UV-written waveguides using integrated Bragg gratings.," *Opt. Lett.*, vol. 35, no. 17, pp. 2849–2851, Sep. 2010.

[87] R. Kashyap, "Chapter 4 - Theory of fiber Bragg gratings," in *Fiber Bragg Gratings*, 1999, pp. 119–194.

[88] H. L. Rogers, C. Holmes, J. C. Gates, and P. G. R. Smith, "Analysis of Dispersion Characteristics of Planar Waveguides via Multi-Order Interrogation of Integrated Bragg Gratings," *IEEE Photonics J.*, vol. 4, no. 2, pp. 310–316, Apr. 2012.

[89] L. G. Carpenter, "Precision dicing and micromilling of silica for photonics," *Thesis*, 2013.

[90] J. C. Stover, "Chapter 2 - Quantifying surface roughness," in *Optical Scattering: Measurement and Analysis, Third Edition*, 2012, pp. 23–45.

[91] International Organisation for Standardisation, "ISO 25178-2:2012 Geometrical product specifications (GPS) -- Surface texture: Areal -- Part 2: Terms, definitions and surface texture parameters." 2012.

[92] L. G. Carpenter, H. L. Rogers, P. A. Cooper, C. Holmes, J. C. Gates, and P. G. R. Smith, "Low optical-loss facet preparation for silica-on-silicon photonics using the ductile dicing regime," *J. Phys. D. Appl. Phys.*, vol. 46, no. 47, p. 475103, 2013.

[93] C. Gui, M. Elwenspoek, J. G. E. Gardeniers, and P. V. Lambeck, "Present and Future Role of Chemical Mechanical Polishing in Wafer Bonding," *J. Electrochem. Soc.*, vol. 145, no. 6, pp. 2198–2204, 1998.

[94] H. L. Rogers, C. Holmes, P. L. Mennea, J. C. Gates, and P. G. R. Smith, "Experimental observation of coupling between physically separated planar waveguides utilising tilted Bragg grating structures," in *European Conference on Integrated Optics*, 2012, p. ThP032.

[95] D. Dai, J. Bauters, and J. E. Bowers, "Passive technologies for future large-scale photonic integrated circuits on silicon: polarization handling, light non-reciprocity and loss reduction," *Light Sci. Appl.*, vol. 1, no. 3, p. e1, 2012.

[96] B. Shen, P. Wang, R. Polson, and R. Menon, "An integrated-nanophotonics polarization beamsplitter with 2.4 × 2.4 μm2 footprint," *Nat Phot.*, vol. 9, no. 6, pp. 378–382, Jun. 2015.

[97] J. D. Sarmiento-Merenguel, R. Halir, X. Le Roux, C. Alonso-Ramos, L. Vivien, P. Cheben, E. Durán-Valdeiglesias, I. Molina-Fernández, D. Marris-Morini, D.-X. Xu, J. H. Schmid, S. Janz, and A. Ortega-Moñux, "Demonstration of integrated polarization control with a 40 dB range in extinction ratio," *Optica*, vol. 2, no. 12. pp. 1019–1023, 2015.

[98] P. S. Westbrook, T. A. Strasser, and T. Erdogan, "In-line polarimeter using blazed fiber gratings," *IEEE Photonics Technol. Lett.*, vol. 12, no. 10, pp. 1352–1354, Oct. 2000.

[99] S. J. Mihailov, R. B. Walker, T. J. Stocki, and D. C. Johnson, "Fabrication of tilted fibre-grating polarisation-dependent loss equaliser," *Electron. Lett.*, vol. 37, no. 5, pp. 284–286, 2001.

[100] K. Zhou, G. Simpson, X. Chen, L. Zhang, and I. Bennion, "High extinction ratio in-fiber polarizers based on 45 degree tilted fiber Bragg gratings," *Opt. Lett.*, vol. 30, no. 11, pp. 1285–1287, Jun. 2005.

[101] Z. Yan, C. Mou, K. Zhou, X. Chen, and L. Zhang, "UV-Inscription, Polarization-Dependant Loss Characteristics and Applications of 45° Tilted Fiber Gratings," *J. Light. Technol.*, vol. 29, no. 18, pp. 2715–2724, 2011.

[102] A. K. Ghatak and K. Thyagarajan, "Chapter 2 - Basic Optics," in *Introduction to Fiber Optics*, 1st ed., C. U. Press, Ed. Cambridge, 1998, pp. 9–28.

[103] Y. Li, M. Froggatt, and T. Erdogan, "Volume Current Method for Analysis of Tilted Fiber," *J. Light. Technol.*, vol. 19, no. 10, pp. 1580–1591, 2001.

[104] T. Yoshino, "Theoretical analysis of a tilted fiber grating polarizer by the beam tracing approach," *J. Opt. Soc. Am. B*, vol. 29, no. 9, pp. 2478–2483, Aug. 2012.

[105] M. T. Posner, P. L. Mennea, N. Podoliak, P. Horak, J. C. Gates, and P. G. R. Smith, "45° tilted gratings for silica-based integrated polarizers," in *European Conference on Lasers and Electro-Optics - European Quantum Electronics Conference*, 2015, p. CE_10_5.

[106] A. Adebayo, Z. Yan, L. Zhang, and D. Robinson, "45°-TFG based in-fiber polarizer at 800 nm by UV inscription," in *Asia Communications and Photonics Conference*, 2012, p. ATh2A.4.

[107] M. D. Baiad and R. Kashyap, "Concatenation of surface plasmon resonance sensors in a single optical fiber using tilted fiber Bragg gratings," *Opt. Lett.*, vol. 40, no. 1, pp. 115–118, Jan. 2015.

[108] P. C. Gow, R. H. S. Bannerman, C. Holmes, J. C. Gates, and P. G. R. Smith, "Direct UV Written Integrated Planar Waveguides Fabricated with 213 nm Light," in *Conference on Lasers and Electro-Optics*, 2017, p. CE-p-25.

[109] H. Ma, J. Zhang, Z. Chen, and Z. Jin, "Tilted Waveguide Gratings and Implications for Optical Waveguide-Ring Resonator," *J. Light. Technol.*, vol. 33, no. 19, pp. 4176–4183, 2015.

[110] H. Ma, S. Wang, and Z. Jin, "Measurements of excess loss of the crossed waveguide using optical waveguide ring resonators," *Opt. Commun.*, vol. 281, no. 24, pp. 6016–6018, Dec. 2008.

[111] L. K. Shalm, E. Meyer-Scott, B. G. Christensen, P. Bierhorst, M. A. Wayne, M. J. Stevens, T. Gerrits, S. Glancy, D. R. Hamel, M. S. Allman, K. J. Coakley, S. D. Dyer, C. Hodge, A. E. Lita, V. B. Verma, C. Lambrocco, E. Tortorici, A. L. Migdall, Y. Zhang, D. R. Kumor, W. H. Farr, F. Marsili, M. D. Shaw, J. A. Stern, C. Abellán, W. Amaya, V. Pruneri, T. Jennewein, M. W. Mitchell, P. G. Kwiat, J. C. Bienfang, R. P. Mirin, E. Knill, and S. W. Nam, "Strong Loophole-Free Test of Local Realism," *Phys. Rev. Lett.*, vol. 115, no. 25, p. 250402, Dec. 2015.

[112] C. R. Lima, L. L. Soares, L. Cescato, and A. L. Gobbi, "Reflecting polarizing beam splitter," *Opt. Lett.*, vol. 22, no. 4, pp. 203–205, 1997.

[113] L. Zhou and W. Liu, "Broadband polarizing beam splitter with an embedded metal-wire nanograting," *Opt. Lett.*, vol. 30, no. 12, pp. 1434–1436, 2005.

[114] D. Taillaert, H. Chong, P. I. Borel, L. H. Frandsen, R. M. De La Rue, and R. Baets, "A compact two-dimensional grating coupler used as a polarization splitter," *IEEE Photonics Technol. Lett.*, vol. 15, no. 9, pp. 1249–1251, 2003.

[115] B. Wang, L. Chen, L. Lei, and J. Zhou, "Reflection polarizing beam splitter of a fused-silica metal-based sandwiched grating at an incident angle of 45°," *Opt. Laser Technol.*, vol. 47, pp. 179–182, 2013.

[116] X. Guan, H. Wu, Y. Shi, and D. Dai, "Extremely small polarization beam splitter based on a multimode interference coupler with a silicon hybrid plasmonic waveguide," *Opt. Lett.*, vol. 39, no. 2, pp. 259–62, 2014.

[117] K. Thyagarajan, S. Diggavi, and A. K. Ghatak, "Integrated-optic polarization-splitting directional coupler," *Opt. Lett.*, vol. 14, no. 23, pp. 1333–1335, 1989.

[118] M. Okuno, A. Sugita, K. Jinguji, and M. Kawachi, "Birefringence control of silica waveguides on Si and its application to a polarization-beam splitter/switch," *J. Light. Technol.*, vol. 12, no. 4, pp. 625–633, 1994.

[119] Y. Hashizume, T. Goh, Y. Inoue, K. Hamamoto, and M. Itoh, "Polarization beam splitter with different core widths and its application to dual-polarization optical hybrid," *J. Light. Technol.*, vol. 33, no. 2, pp. 408–414, 2015.

[120] J. Xiao and X. Sun, “Proposal for a compact silicon microring resonator-based polarization demultiplexer,” *J. Nanophoton.*, vol. 9, no. 1, p. 93055, 2015.

[121] B. Shen, R. Polson, and R. Menon, “Broadband asymmetric light transmission via all-dielectric digital metasurfaces,” *Opt Express*, vol. 23, no. 16, pp. 20961–20970, 2015.

[122] K. W. Chang and C. C. Huang, “Ultrashort broadband polarization beam splitter based on a combined hybrid plasmonic waveguide,” *Sci. Rep.*, vol. 6, no. January, p. 19609, 2016.

[123] R. B. Walker, S. J. Mihailov, P. Lu, and D. Grobnic, “Shaping the radiation field of tilted fiber Bragg gratings,” *J. Opt. Soc. Am. B*, vol. 22, no. 5, pp. 962–974, 2005.

[124] Y. Li and T. G. Brown, “Radiation modes and tilted fiber gratings,” *J. Opt. Soc. Am. B*, vol. 23, no. 8, pp. 1544–1555, 2006.

[125] S. Lu, O. Xu, S. Feng, and S.-S. Jian, “Analysis of radiation-mode coupling in reflective and transmissive tilted fiber Bragg gratings,” *J. Opt. Soc. Am. A*, vol. 26, no. 1, pp. 91–98, 2008.

[126] M. T. Posner, P. L. Mennea, N. Podoliak, P. Horak, J. C. Gates, and P. G. R. Smith, “Integrated polarizing coupler based on tilted gratings,” in *Advanced Photonics 2016 (IPR, NOMA, Sensors, Networks, SPPCom, SOF)*, 2016, p. IW3B.3.

[127] M. D. Eisaman, J. Fan, A. Migdall, and S. V Polyakov, “Invited Review Article: Single-photon sources and detectors,” *Rev. Sci. Instrum.*, vol. 82, no. 7, p. 71101, 2011.

[128] G. Agrawal, “Chapter 10 - Four-Wave Mixing,” in *Nonlinear Fiber Optics (Fifth Edition)*, Fifth Edit., G. Agrawal, Ed. Boston: Academic Press, 2013, pp. 397–456.

[129] J. B. Spring, P. S. Salter, B. J. Metcalf, P. C. Humphreys, M. Moore, N. Thomas-Peter, M. Barbieri, X.-M. Jin, N. K. Langford, W. S. Kolthammer, M. J. Booth, and I. A. Walmsley, “On-chip low loss heralded source of pure single photons,” *Opt. Express*, vol. 21, no. 11, pp. 13522–13532, 2013.

[130] J. B. Spring, “Single Photon Generation and Quantum Computing with Integrated Photonics,” *Thesis*, 2014.

[131] B. J. Smith, P. Mahou, O. Cohen, J. S. Lundeen, and I. A. Walmsley, “Photon pair generation in birefringent optical fibers,” *Opt. Express*, vol. 17, no. 26, pp. 23589–23602, 2009.

[132] R. H. Stolen, “Nonlinearity in fiber transmission,” *Proc. IEEE*, vol. 68, no. 10, pp. 1232–1236, Oct. 1980.

[133] M. Kawachi, “Silica waveguides on silicon and their application to integrated-optic components,” *Opt. Quantum Electron.*, vol. 22, pp. 391–416, 1990.

[134] International Organisation for Standardisation, “ISO 11146-1:2005 Lasers and laser-related equipment -- Test methods for laser beam widths, divergence angles and beam propagation ratios -- Part 1: Stigmatic and simple astigmatic beams.” 2005.

[135] D. P. Laurie, “Calculation of Gauss-Kronkod quadrature rules,” *Math. Comput.*,

vol. 66, no. 219, pp. 1133–1145, 1997.

[136] M. T. Posner, R. H. S. Bannerman, D. H. Smith, P. L. Mennea, J. C. Gates, and P. G. R. Smith, "High-birefringence direct-UV-written silica waveguides for heralded single-photon sources at telecom wavelengths," in *European Conference on Lasers and Electro-Optics - European Quantum Electronics Conference*, 2017, p. CN-P.6.

[137] M. Avenhaus, A. Eckstein, P. J. Mosley, and C. Silberhorn, "Fiber-assisted single-photon spectrograph," *Opt. Express*, vol. 34, no. 18, pp. 2873–2875, 2009.

[138] T. Gerrits, F. Marsili, V. B. Verma, L. K. Shalm, M. Shaw, R. P. Mirin, and S. W. Nam, "Spectral correlation measurements at the Hong-Ou-Mandel interference dip," *Phys. Rev. A*, vol. 91, no. 1, p. 13830, Jan. 2015.

[139] J. Limpert, F. Roser, T. Schreiber, and A. Tunnermann, "High-Power Ultrafast Fiber Laser Systems," *IEEE J. Sel. Top. Quantum Electron.*, vol. 12, no. 2, pp. 233–244, 2006.

[140] S. Sinha, K. E. Urbanek, A. Krzywicki, and R. L. Byer, "Investigation of the suitability of silicate bonding for facet termination in active fiber devices," *Opt. Express*, vol. 15, no. 20, pp. 13003–13022, 2007.

[141] R. Puers and A. Cozma, "Bonding wafers with sodium silicate solution," *J. Micromechanics Microengineering*, vol. 7, no. 3, p. 114, 1997.

[142] P. C. Gow, A. Jantzen, J. C. Gates, P. G. R. Smith, and C. Holmes, "Direct 9.3 μm CO_2 Laser Consolidation of FHD Silica for Planar Devices," in *European Conference on Lasers and Electro-Optics - European Quantum Electronics Conference*, 2017, p. CM-P.1.

[143] N. H. Nickerson, J. F. Fitzsimons, and S. C. Benjamin, "Freely Scalable Quantum Technologies Using Cells of 5-to-50 Qubits with Very Lossy and Noisy Photonic Links," *Phys. Rev. X*, vol. 4, no. 4, p. 41041, Dec. 2014.

[144] A. Courvoisier, M. J. Booth, and P. S. Salter, "Inscription of 3D waveguides in diamond using an ultrafast laser," *Appl. Phys. Lett.*, vol. 109, no. 3, p. 31109, 2016.

[145] R. Nigmatullin, C. J. Ballance, N. de Beaudrap, and S. C. Benjamin, "Minimally complex ion traps as modules for quantum communication and computing," *New J. Phys.*, vol. 18, no. 10, p. 103028, Oct. 2016.

[146] R. J. Beichner, "An introduction to physics education research," *Get. started PER*, vol. 2, no. 1, 2009.

[147] M. T. Posner, P. V. John, N. H. L. Wong, V. Mittal, and M. M. Nunez-Velazquez, "From school classes to UNESCO: IYL-enabled environments for tackling the STEM skills shortage through student-led outreach (Invited Paper)," in *Proc. SPIE 9946*, 2016, pp. 9946–6.

[148] M. T. Posner, P. V John, D. Standen, N. V. Wheeler, L. D. van Putten, N. Soper, T. Parsonage, N. H. L. Wong, and G. Brambilla, "Reflecting photonics: Reaching new audiences through new partnerships: IYL 2015 and the Royal Horticultural Society flower show," in *Proc. SPIE 9946*, 2016, pp. 9946–2.

[149] M. T. Posner, A. Jantzen, L. D. van Putten, A. Ravagli, A. L. Donko, N. Soper, N. H. L. Wong, and P. V. John, "Cathedral outreach: student-led workshops for school curriculum enhancement in non-traditional environments," in *Proc. SPIE 104520*, 2017, pp. 10452–7.

[150] N. H. L. Wong, M. T. Posner, and P. V. John, "The Lightwave Programme and Roadshow : An Overview and Update," in *Proc. SPIE 9793*, 2015, vol. 97932V, pp. 1–16.

[151] N. H. L. Wong, M. T. Posner, V. Mittal, D. R. Gray, and P. V John, "Taking local optics outreach abroad for IYL 2015: administrative and logistical challenges and strategies," in *Proc. SPIE 9946*, 2016, pp. 9946–14.

[152] N. H. L. Wong, A. S. K. Tong, M. T. Posner, and A. Ravagli, "Modular and extensible lesson on fiber optics for youths," in *Proc. SPIE 104520*, 2017, pp. 10452–9.

[153] R. Morgan, C. Kirby, and A. Stamenkovic, "The UK STEM Education Landscape," 2016. [Online]. Available: http://www.raeng.org.uk/publications/reports/uk-stem-education-landscape. [Accessed: 03-May-2017].

[154] Institute of Physics, "Raising Aspirations in Physics: A Review of Research into Barriers to STEM Participation for Students from Disadvantaged Backgrounds," 2014. [Online]. Available: http://www.iop.org/publications/iop/2014/file_64466.pdf. [Accessed: 15-Sep-2017].

[155] Hanover Research, "Trends in Higher Education Marketing, Recruitment and Technology," 2014. [Online]. Available: http://www.hanoverresearch.com/media/Trends-in-Higher-Education-Marketing-Recruitment-and-Technology-2.pdf. [Accessed: 15-Sep-2017].

[156] "What is Public Engagement?," *NCCPE*, 2016. [Online]. Available: https://www.publicengagement.ac.uk/explore-it/what-public-engagement. [Accessed: 06-Aug-2016].

[157] "Concordat for Engaging the Public with Research: RCUK." [Online]. Available: http://www.rcuk.ac.uk/documents/scisoc/concordatforengagingthepublicwithresearch-pdf/. [Accessed: 19-Apr-2017].

[158] "RCUK Impact Requirements Frequently Asked Questions." [Online]. Available: http://www.rcuk.ac.uk/RCUK-prod/assets/documents/impacts/RCUKImpactFAQ.pdf. [Accessed: 06-May-2015].

[159] L. Archer, J. DeWitt, and B. Willis, "Adolescent boys' science aspirations: Masculinity, capital, and power," *J. Res. Sci. Teach.*, vol. 51, no. 1, pp. 1–30, Jan. 2014.

[160] J. DeWitt and L. Archer, "Who Aspires to a Science Career? A comparison of survey responses from primary and secondary school students," *Int. J. Sci. Educ.*, vol. 37, no. 13, pp. 2170–2192, Sep. 2015.

[161] E. Bricchi, J. C. Baggett, D. A. Guilhot, and I. O. Musgrave, "The lightwave road show," in *Education and Training in Optics and Photonics, OSA Technical Digest*

Series, 2003.

[162] H. D. Foreman, F. R. Parmigiani, M. A. Roelens, and R. E. Simpson, "The Lightwave Roadshow," in *ETOP 2005: Conference on Education and Training in Optics and Photonics*, 2005, pp. 24–27.

[163] D. R. Sokolff, Z. B. Lakhdar, I. B. Culaba, V. Lakshminarayanan, J. T. Maquiling, and A. Mazzolini, "Active learning in optics and photonics," 2006.

[164] Department of Education UK Government, "Science programmes of study : key stages 1 and 2," 2013. [Online]. Available: https://www.gov.uk/government/uploads/system/uploads/attachment_data/file/425618/PRIMARY_national_curriculum_-_Science.pdf. [Accessed: 21-Sep-2017].

[165] L. Wager, *Building School-University Parternships Guide Book*, 1st ed. Southampton: University of Southampton, 2016.

[166] C. Thorley, "Physicists and Outreach: Implications of schools physics outreach programmes from the perspective of the participating physicists," *Thesis*, 2016.

[167] N. Mahony and H. C. Stephansen, "Engaging with the public in public engagement with research," *Res. All*, vol. 1, no. 1, pp. 35–51, 2017.

[168] D. Hestenes, M. Wells, and G. Swackhamer, "Force concept inventory," *Phys. Teach.*, vol. 30, no. 3, pp. 141–158, 1992.

[169] R. K. Thornton and D. R. Sokoloff, "Assessing student learning of Newton's laws: The Force and Motion Conceptual Evaluation and the Evaluation of Active Learning Laboratory and Lecture Curricula," *Am. J. Phys.*, vol. 66, no. 4, pp. 338–352, 1998.

[170] N. Miller and P. V. John, "Public education and the electro-optical industry: a strategic partnership in creating photonics classes for high school students (Invited Paper)," in *Proc. SPIE 3831*, 2000, pp. 80–83.

[171] A. MacDonald, "'Not for people like me?' Under-represented groups in science, technology and engineering," 2014. [Online]. Available: https://www.wisecampaign.org.uk/uploads/wise/files/not_for_people_like_me.pdf.

[172] J. L. Miller, "Extraction angle for blazed Bragg gratings," in *Optical Communications Rules of Thumb*, 2003, p. 356.

[173] D. Taillaert, W. Bogaerts, P. Bienstman, T. F. Krauss, P. Van Daele, I. Moerman, S. Verstuyft, K. De Mesel, and R. Baets, "An out-of-plane grating coupler for efficient butt-coupling between compact planar waveguides and single-mode fibers," *IEEE J. Quantum Electron.*, vol. 38, no. 7, pp. 949–955, Jul. 2002.

[174] K. K. Mehta, C. D. Bruzewicz, R. McConnell, R. J. Ram, J. M. Sage, and J. Chiaverini, "Integrated optical addressing of an ion qubit," *Nat Nano*, vol. 11, no. 12, pp. 1066–1070, Dec. 2016.

[175] P. Bayvel, "Communicating with Light," 2014. [Online]. Available: https://royalsociety.org/events/2014/10/clifford-paterson/. [Accessed: 05-May-2015].